Effects of Chiari Malformation on Cerebrospinal Fluid within the Spinal Canal

BY

WOJCIECH KALATA
B.S., University of Illinois at Chicago, 1999
M.S., University of Illinois at Chicago, 2002

THESIS

Submitted as partial fulfillment of the requirements
for the degree of PhD of Science in Mechanical Engineering
in the Graduate Collage of the
University of Illinois at Chicago, 2012

Chicago, Illinois

Defense Committee:

Thomas J. Royston, Chair and Advisor
Francis Loth, University of Akron
Wally J. Minkowycz
Farzad Mashayek
Paul F. Fischer, Argonne National Laboratory

This work is dedicated to my family:

to my precious daughters Zosia and Martynka,

and my loving wife Madzia.

May any hardships be overpowered by love and family bonds.

I would like to give my deepest gratitude

to my parents for their patience and support.

They always encouraged me towards education

ACKNOWLEDGMENTS

I would like to express great appreciation and gratitude to Dr. Francis Loth for his guidance, support, friendship and compassion. His role as a mentor taught me academic and ethical professionalism along with friendly approach to engineering research in the laboratory. His support throughout my hard times will never be forgotten.

I would like to thank my committee members, Dr. Paul F. Fischer, Dr. Francis Loth, Dr. Farzad Mashayek, Dr. Wally J. Minkowycz and Dr. Thomas J. Royston, for their support in realization of this work. Their valuable engineering expertise and multi-discipline character made this work complete.

I would like to give my great appreciation to the organizations that supported this project. The Ed and Gayle Labuda Charitable Fund of the Vanguard Charitable Endowment Program, the Labuda Family Foundation, and the American Syringomyelia Alliance Project (ASAP) Research Grant supported this work. My only hope is that this work will have an impact towards their importan cause.

Also I would like to thank American Council for Polish Culture for a Pulaski Scholarship for Advanced Studies.

TABLE OF CONTENTS

LIST OF TABLES

LIST OF FIGURES

LIST OF ABBREVIATIONS

1-D	One Dimensional
2-D	Two Dimensional
3-D	Three Dimensional
3DS	Three Dimensional Simulation
ABS	Acrylonitrile Butadiene Styrene
CFD	Computational Fluid Dynamics
CM	Chiari Malformation
CPBC	Constant Pressure Boundary Condition
CSF	Cerebrospinal Fluid
CT	Computerized Tomography
DP2PdQ	Diastolic Peak to Peak Flow Difference
ECG	Electrocardiogram
FFT	Fast-Fourier Transform
FSI	Fluid-Structure Interaction
IHNWN	Inverse of Healthy-Normalized Womersley Number
FM	Foramen Magnum
MR	Magnetic Resonance
MRI	Magnetic Resonance Imaging
IBC	Inlet Boundary Condition
pcMR	Phase-Contrast Magnetic Resonance
pcMRI	Phase-Contrast Magnetic Resonance Imaging
PWV	Pulse Wave Velocity
SAS	Subarachnoid Space
SSL	Stratasys Layer
SM	Syringomyelia
SP2PdQ	Systolic Peak to Peak Flow Difference
STL	Stereolithography
UAF	Unsteady Annulus Flow
VWS	Velocity Wave Speed
WF	Womersley Flow

SUMMARY

Cerebrospinal fluid (CSF) moves in a pulsatile manner within the spinal canal and cranial cavity within both the subarachnoid and ventricular spaces. CSF hydrodynamics in the subcranial subarachnoid space is disrupted by Chiari malformation (CM) which can resist CSF motion into and out of the cranium. Magnetic resonance imaging (MRI) enables *in vivo* measurements of both the spinal canal anatomy and CSF velocity. Since alterations in CSF motion have been reported in patients with CM and/or syringomyelia, a hydrodynamic analysis of CSF motion is warranted.

Using geometry and velocity from MRI, this work investigated various flow parameters in both healthy subjects and patients with CM. Computational fluid dynamics was performed to obtain an unsteady resistance parameter, longitudinal impedance that indicated that patients have higher resistance than healthy subjects. Two CM patients had pre-surgery resistance values that were higher (31% and 21%) than post-surgery. Also, a complex spinal canal geometry of a patient with CM was investigated both numerically and experimentally. A Sylgard flow model of CM was tested in an MRI scanner and compared with numerical results. Good agreement was obtained between numerical and experimental results; however, significant noise in the MR experimental made comparison difficult. A statistical flow waveform analysis was performed on many cases of healthy subjects and patients. These hydrodynamic parameters show differences between CM patients and healthy subjects. In particular, the duration of systole was shown to be longer for CM patients. This parameter may have clinical utility to help quantify the hydrodynamics alteration in CM patients. Finally, a novel technique was developed to measure a velocity wave speed of CSF (~4m/s) from specialized MRI which may provide an overall quantitative assessment of the rigidity of a CM patient's spinal canal system.

1. GENERAL INTRODUCTION

Cerebrospinal fluid (CSF) has been linked with various neurological disorders and diseases. Currently modern medicine struggles to successfully overcome these CSF related issues that, in the majority of patients, require invasive corrective procedures to prevent further development or resolve health issues. The work presented here focuses on one CSF related disorders, Chiari malformation (CM). This work is a continuation of a master's thesis work by the same author [1].

1.1 Cerebrospinal Fluid and Subarachnoid Space

1.1.1 Basics

Cerebrospinal fluid (CSF) is a clear liquid that surrounds the brain and the spinal cord. It moves in a pulsatile manner inside the subarachnoid space (SAS) and ventricular system inside the brain. The SAS lies between the pia matter internally and the arachnoid membrane externally. The SAS separates the brain and the spinal cord from their surrounding bone structures, the skull and vertebra (Figures 1.1, 1.2 and 1.3). The CSF pulsation is thought to originate primarily from changes in intracranial blood volume during the cardiac cycle (Figure 1.4). CSF supports and provides a cushion for the brain and the spinal cord, protecting them from sudden movements and trauma. It delivers protein and nutrients to the nervous system, and provides a mechanism for removing waste products from the nervous system.

The amount of CSF volume in the body of a human adult is about 140 ml ranging from 110 to 160 ml. About 25% of its total volume resides in the ventricular system, 20% in cranial SAS, and 55% in the spinal canal [2]. This plasma-like liquid is mainly produced by the choroid

plexuses in the ventricles (Figure 1.2). The production rate is about 0.35 ml/min (or 400-500 ml/day) which roughly represents the replacement of three total volumes per day [2, 3]. The absorption rate of CSF is about the same as the production rate. The CSF is absorbed into the venous system through cranial and spinal arachnoid villi that are located in the SAS.

1.1.2 Mechanical Considerations

The physical properties of CSF and water are similar. The CSF has a specific gravity of 1.007 [3, 4]. Bloomfield et al., measured its dynamic viscosity (μ) within a range from 0.65 to 1.09 mPa·s at 37°C [5]. According to Kestin et al., the viscosity of water is 0.69 mPa·s at 37°C and atmospheric pressure [6]. Thus, CSF is assumed to act as a Newtonian fluid with physical properties of water at human body temperature.

Various sources indicate that the normal lumbar spinal pressure in humans is about 150 mm of saline (H_2O) and it may range from 65 to 195 mm H_2O (~5-15 mmHg, ~670-2000 Pa, ~0.10-0.29 psi) [2-4]. These measurements were obtained by lumbar puncture with human subjects lying down on one side. It has been shown that body position has an effect on this pressure. Subjects measured with the same method but in a sitting position were shown to have a pressure of ~400 mm H_2O [2, 7].

As indicated previously, the flow of CSF is pulsatile, therefore pressure fluctuates also. Since the brain is enclosed in the skull, which is considered to be a rigid cavity, the difference between arterial and venous pulsations inside the skull are the sources of CSF pulsations. CSF pulsations vary with the respiratory and cardiac cycles. With the respiratory cycle, the pressure oscillates about 2-5 mm H_2O, and with cardiac cycle about 1-2 mm H_2O [3].

1.2 Chiari Malformation

1.2.1 Basics

CM is associated with abnormal CSF flow. CM is a disorder formed by a downward displacement (herniation) of the base of the hind brain (cerebellar tonsils) into the foramen magnum (FM) that is an opening into the sub-cranial portion of the spinal canal (Figure 1.1C and 1.1D). This disorder disrupts the normal hydrodynamics of CSF flow by reducing the spinal canal's cross-sectional area and corresponding increases in the CSF velocity.

1.2.2 Association with Syringomyelia

Syringomyelia (SM) is associated with syrinx formation where a fluid filled pocket, called a syrinx, is formed inside the spinal cord (Figure 1.1C and 1.1D). The classification of SM is difficult and has been debated by neurosurgeons [8]. Milhorat et al. reported that 65% of 364 CM patients had SM [9]. Also, Ellenbogen et al. reported that out of 65 patients with CM I, 78% had SM [10].

1.2.3 Categorization

The classical categorization of CM is presented here. Type I CM (CMI), or sometimes called adult-CM, is associated with cerebellar (tonsillar) herniation into the cisterna magna. SM may also be also present. Type II CM (CMII), also known as Arnold-CM, involves a downward displacement of the cerebellar tonsils, the fourth ventricle and brain stem (see Figure 1.2). More advanced SM may be present. CMII may include hydrocephalus (condition with increased size of lateral ventricles) and is almost always associated with meningomyelocele (the most severe form of spina bifida, the failure of bone and tissue surrounding the spinal cord to close properly).

Type III CM consists of displacement of the cerebellum and portions of the brain stem into a meningocele (the defect of outside layers of the base of the brain and upper cervical region). Type IV CM, the rarest of all four types, refers to cases with underdevelopment of the cerebellum (cerebellar hypoplasia). CM types III and IV are less common than types I and II [8, 11, 12].

1.2.4 Statistics

Bejjani et al. has shown, based on magnetic resonance imaging (MRI) and brain dissection studies, about 0.60% incidence of CM to be present in his patient population [11]. Speer has estimated that the approximate range of patients with CM (CMI and CMII) and SM treated in the US was between 125,700 to 184,900 (or 0.045% to 0.066% based on US population from 1997)[13]. When reasoning that about 70% (averaged value from section 1.2.2) of CMI had SM, it can be estimated that in 1997 the range of US patients with CM was from 168,100 to 247,700. Or the estimated range of people with CM in the US was between 0.060% and 0.088% of Americans have CM.

1.2.5 Current Diagnosis and Treatment

The most common symptoms that lead to a suspicion or initial diagnosis of CM are headache, neck pain, sensory disturbances, reflex change, ataxia (gross lack of coordination in muscle movements), dizziness, and respiratory dysfunction [10, 14-16].

Noninvasive medical imaging techniques such as MRI, Computerized Tomography (CT), and ultrasound have become standard tools for diagnosing a wide spectrum of health problems. CM and SM, with their characteristic geometrical features, are recognizable with use of imaging

techniques mentioned above. These imaging techniques have become important tools in the diagnosis and research for better care and management of these painful conditions.

Currently, CM is treated temporarily with pain management and in the long run with decompression surgery. Although there are various surgical techniques, generally the neurosurgeon removes a small portion of the base of the skull and some portions of the top vertebrae to widen the foramen magnum to allow CSF motion with less resistance ([10, 14, 15]). The success rate for decompression surgery, which does not have clear definition among reported literature, varies. Ellenbogen et al. categorized long-term outcome in 65 patients into three groups (good, improved and poor), separating pediatric and adult cases. Both age-based cases averaged 66% "good", 31% "improved", and 3% "poor outcome" [10]. Alzate et al. reported on 66 patients with a follow-up period after surgery of 24 months (mean value). An "excellent" outcome for 82% of patients was reported. The other 18% were reported as "good," "unchanged" or "worsened" [14].

Another invasive technique that is employed to relieve symptoms in some CM patients that have SM, is shunting [17, 18]. In this procedure, a shunt is placed inside the syrinx to drain accumulated fluid. This reduces the syrinx size and the SM/CM symptoms can be resolved. However, this procedure is not successful in all CM cases.

1.2.6 Historical Background

Historical aspects of CM were presented by Bejjani, Lotbiniere and Schijman in three different articles all agreeing on aspects of how to progress towards better understanding of the pathology [11, 12, 19]. All three articles describe discovery and early categorization by Hans Chiari after whom the malformation was named after. All three articles also indicate that

besides Chiari, there were others who were able to identify the cerebellar displacement and indicate its importance, such as Theodor Langhans, John Cleland and Julius Arnold.

Based on articles by Bejjani, Lotbiniere and Schijman, CM breakthroughs (or milestones) can be divided into distinct time periods as shown in Figure 1.5. An obvious starting point for CM research breakthroughs is a series of work toward a discovery. Discovery is followed by early categorization, indication and early attempts for treatment of CM, more detailed categorization of CM, and radiological imaging with X-ray. All three authors agreed on the significant impact of MR technology on diagnosis, improvement, and monitoring of CM.

In addition to the previously mentions milestones, CFD was added as a recent area of breakthrough. Similar to MRI, the potential of CFD is still yet to be fully realized as further research is needed to develop clinical uses. What will be the impact of CFD simulations that can describe CSF hydrodynamics within the SAS of CM patients? Hopefully, CFD, coupled with MRI and other computational modalities, will help doctors to study, diagnose, and treat CM.

1.3 CM/SM and MRI

The recent literature on CM has mainly focused on using MRI for diagnosis and further research. Also, cine MRI, known as phase-contrast MRI (pcMRI), has gained popularity since velocity measurements in the pathogenic regions became possible ([20-23]). Further comparative studies have shown velocity measurements in CM and/or SM patients before and after the decompression surgery [16, 24-31]. Some of these studies included healthy volunteers. These studies indicated that before the surgery, the average velocities were higher than after the surgery. From a fluid dynamics perspective, these velocity changes are a result of geometrical changes that are accomplished by decompression surgery. Note that while velocity magnitudes

may vary significantly pre- and post-surgically, the flow waveform magnitudes may still be similar [28, 29]. In addition to flow measurements, Heiss et al. performed geometrical and pressure analysis for healthy volunteers and patients before and after surgery [26]. Although he focused on SM, his data supports the fact that decompression surgery favorably alters the CSF hydrodynamics from a pathological state towards a healthier state.

1.4 Mechanical Engineering Link to Medicine

In addition to advances of MRI technology, CFD and experimental modeling techniques became accessible tools for an investigation of biological flows, especially in the hemodynamics field such as blood flow within arteries, veins, aneurysms, and various grafting devices [32-35]. The numerical simulation of biological flows has advanced dramatically as computational power, programming techniques, and software developments have improved along with today's technology. The significance of using MRI technology with CFD simulations lies in the fact that diagnostic information can be obtained by entirely noninvasive procedures. Loth et al. has performed hydrodynamics analysis using 1-D and 2-D CFD on annuli resembling various levels of the spinal canal with a realistic flow CSF waveform [36]. Velocity profiles and pressure drop were investigated for various annular shapes. The velocity fields were shown to be blunt due to the inertial dominated flow as expected by the large Womersley numbers. The pressure drop waveform was found to be dependent on the flow waveform and cross-sectional area.

MRI, computational techniques, and experimental simulation provide a set of tools that enable biofluids research to investigate better treatments or resolution of biofluids-related health problems. Studies which combine numerical work validated with bench-top experimental work have proven to be highly respected by engineers and researchers in the biofluids area. Such

studies by Ford et al., Steinman et. al, and Lei et. al, among many others, focus on validated numerical studies of biological flow within the well defined geometries obtained from MRI [35, 37, 38]. These studies indicate good agreement between numerical and experimental results of fluid velocity.

1.5 Motivation and Specific Aims

As previously noted, CM causes abnormal CSF hydrodynamics through a restriction of the SAS space in the foramen magnum and upper cervical regions. The main treatment option for CM is decompression surgery. Providing more information about the factors that lead to CM may help to obtain a cure or prevent the progression as well as possibly improve the success rate of surgery. The general hypothesis is that hydrodynamic changes to the CSF system reflect the underlying pathophysiology associated with CM disease, and serve as a better prognostic indicator than standard static methods that are currently being used clinically. Alterations to the hydrodynamics of CSF into and out of the cranium can be due, in part, to structural anomalies leading to increased flow resistance, or changes in spinal canal compliance, or both. This work will serve as a pilot study for larger clinical studies to determine if an improved diagnosis of CM can be obtained from the assessment of CSF resistance and compliance, and whether this method may be useful in follow-up treatments. Future clinical studies would be required to determine the underlying causal relationship between these hydrodynamic parameters and neurological symptoms, radiological severity, and surgical success. The **significance** of the current study will be to describe the variety and range of CSF hydrodynamics in CM patients. As such new and more accurate methods to assist in standard clinical diagnosis and treatment of CM may be possible which is important for the more than 20,000 patients who are evaluated each year for

decompression surgery. According to National Institute of Neurological Disorders and Stroke, CM is more common than 1 in 1000 births which puts its impact in the same range as multiple sclerosis and hydrocephalus [1, 2].

This work uses imaging along with computational and experimental tools to better understand CSF hydrodynamics. Both geometry and velocity-encoded MRI are used for analytical, CFD, experimental and image analysis studies. It is important to emphasize that analysis of unsteady CSF dynamics is an attempt to assess the hydrodynamic environment more accurately. This work goes beyond the static MRI approach, which is the current "gold standard" and is not always a good indicator of CM symptoms.

This thesis consists of four different topics. The first topic (Chapter 2) describes 3-D transient CFD simulations that compare a healthy case versus two patients with CM before and after the decompression surgery. This is a review and continuation of a Master's Thesis work [1]. The comparison and progress level is assessed with transient resistance calculations for CSF through a CM geometry. This part of the thesis sets a base line for CFD techniques that use SAS geometry and CSF flow. Each case has been characterized with the flow resistance parameter. This parameter is a potential CM severity marker that a physician may find valuable.

The second topic (Chapter 3) is a hydrodynamic investigation employing a physiologically realistic experimental flow model of CM. The bench-top experiment is compared with patient MRI and a CFD model for validation of the numerical results. In this chapter, complicated structures of CM blockage features were investigated. The CSF hydrodynamics from the experiment and the CFD determined the regions of high velocity and corresponding abnormal pressure drop.

In the next topic (Chapter 4), a statistical comparison of flow waveform and geometric features of healthy volunteers versus CM patients is described. The statistical analysis of CSF flow waveforms pointed out various differences in systole and diastole. Based on high number of test subjects, this type of study may indicate CSF flow waveform features that may become guidelines for CM assessment.

The last topic (Chapter 5) focuses on measurement of velocity wave speed (VWS) inside the cervical SAS obtained from novel high-speed pcMRI. Using this method, VWS was obtained for CSF flow within the SAS. This novel marker may provide a measure of stiffness of cervical SAS.

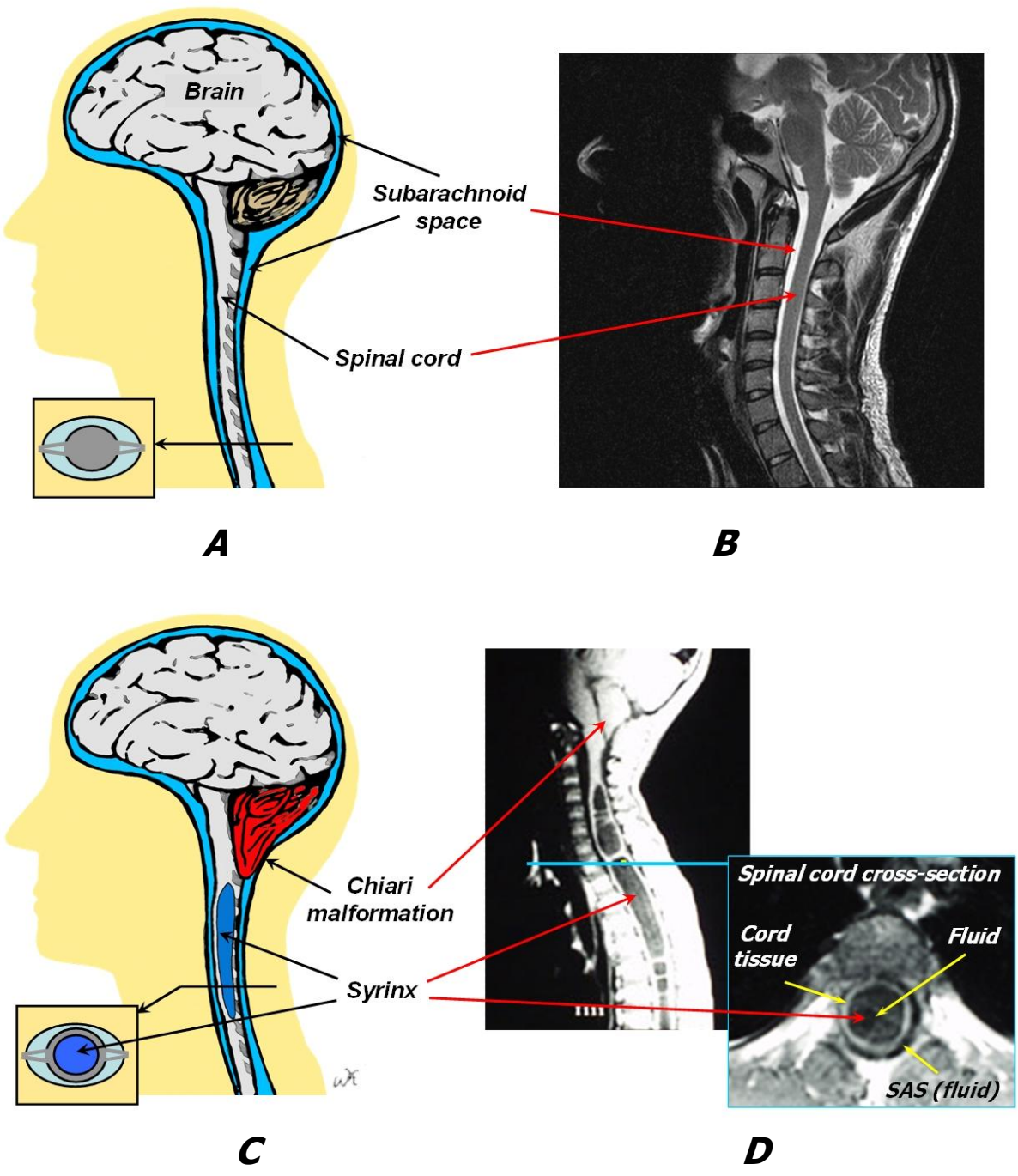

Figure 1.1. Brain and spinal canal in healthy subject, **A.** Simplified sketch and **B.** MR image of SAS in the head and upper section of the spinal canal. Brain with CM and a spinal canal with SM **C.** Simplified sketch and **D**. MR image of CM and SM**.**

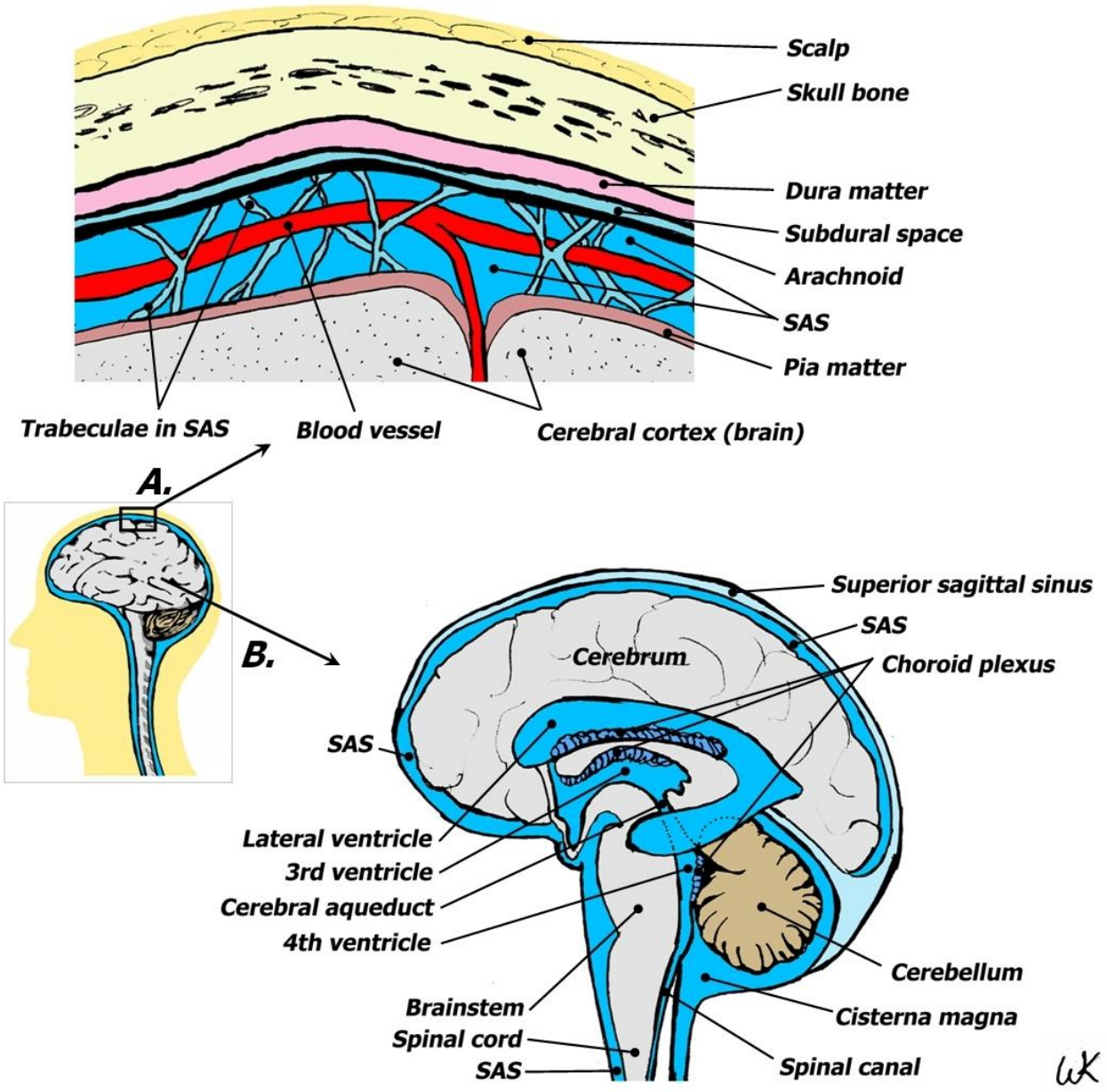

Figure 1.2. Representation of ventricles and SAS in the head. CSF is represented by blue color. **A.** Cross-section on top of the head. **B.** Sagittal cross-section across the middle of the head.

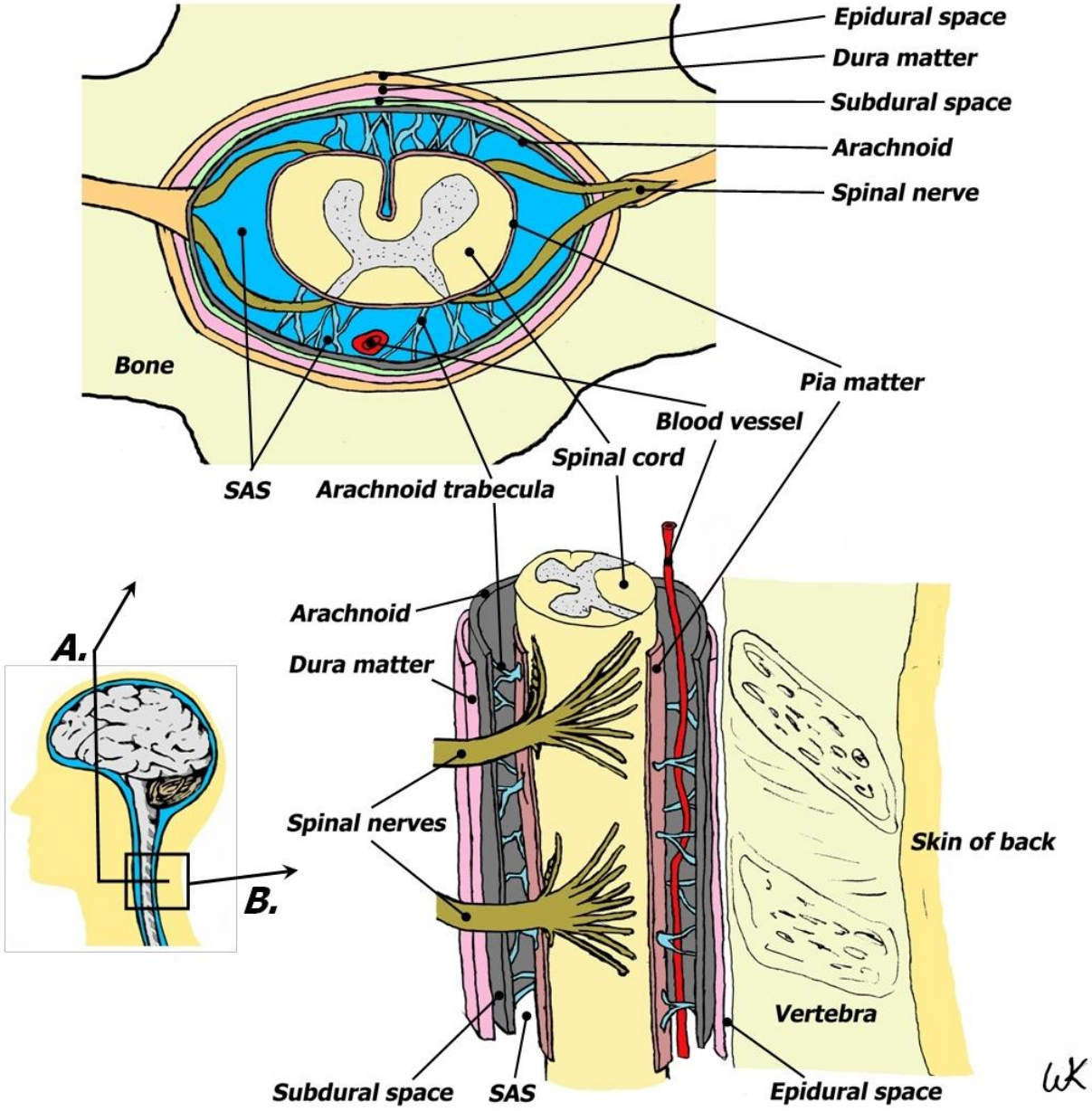

Figure 1.3. Representation of SAS in the spinal canal. CSF is represented by blue color. **A.** Axial cross-section of the spinal canal. **B.** Sagittal cross-section indicating tissue and space layers between the bone and the spinal cord.

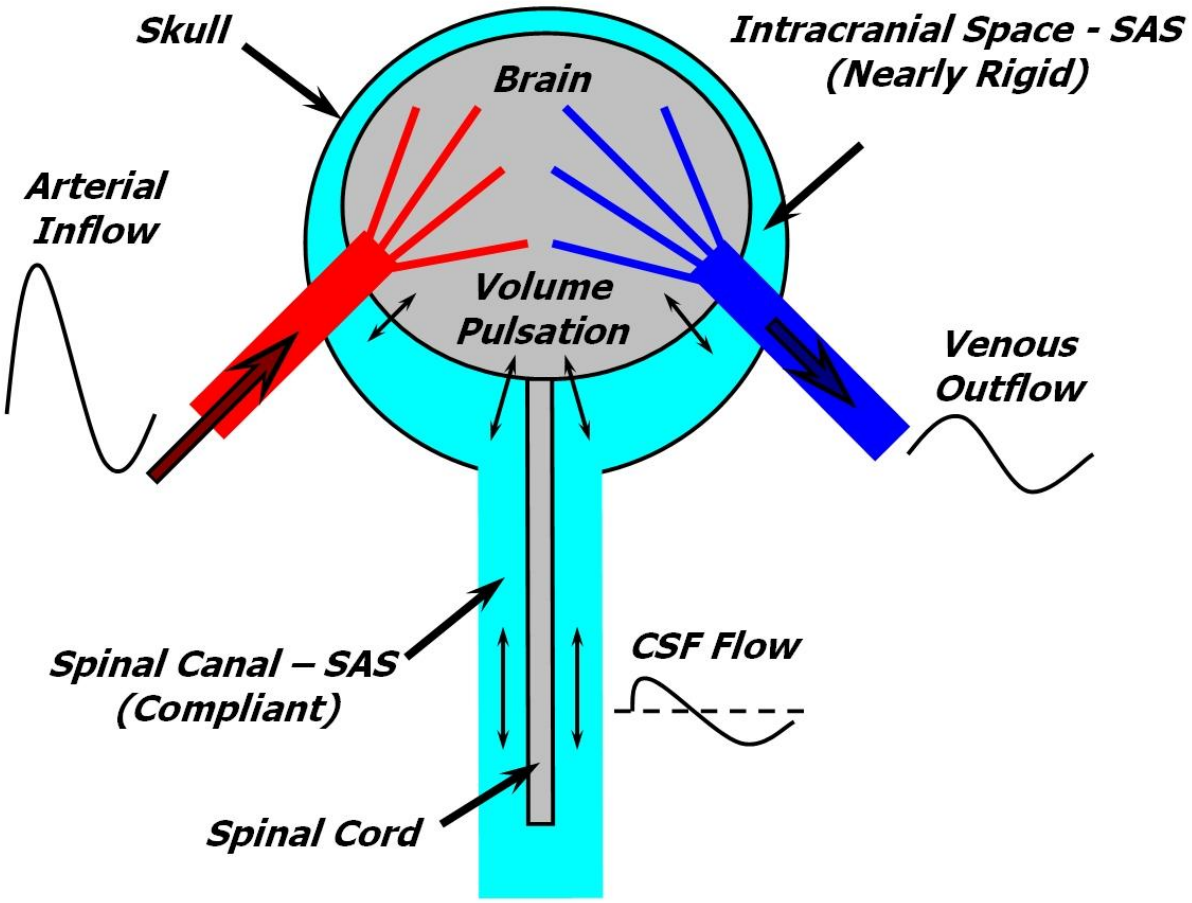

Figure 1.4. Simplified diagram of CSF pulsation.

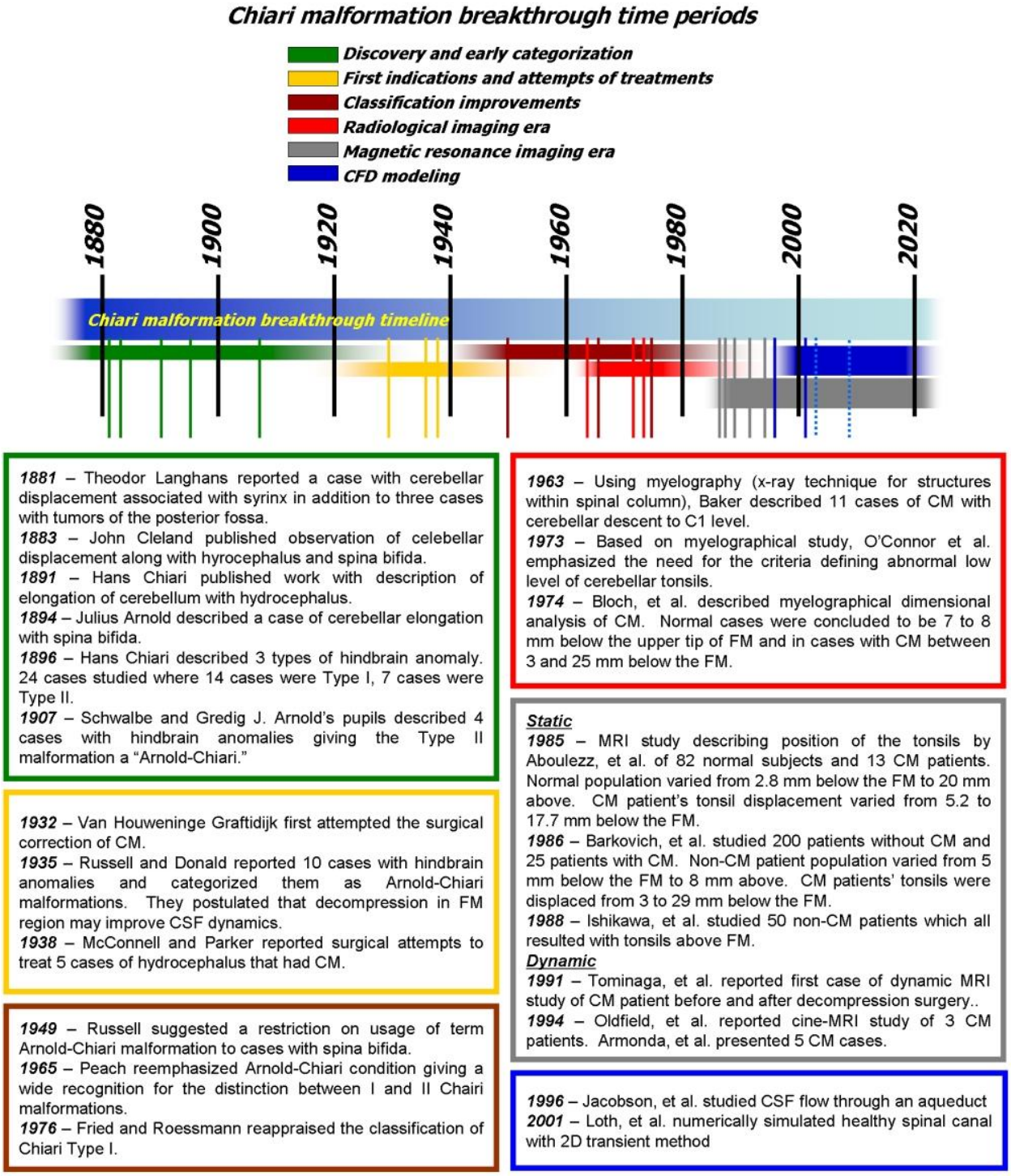

Figure 1.5. Historical aspects of CM.

2. CSF FLOW RESISTANCE – CFD STUDY

2.1 Introduction

In general, the geometry and flow (or pressure) boundary conditions are required in order to solve Navier-Stokes equations. With MRI technology, it is possible to obtain geometry of biological conduits like arteries, veins, and the SAS with their corresponding fluid velocity. Unfortunately, parameters such as wall shear stress or pressure in the SAS are extremely difficult to obtain. With the help of MRI, CSF flow fields, which are transient and cyclic in nature, can be simulated by solution of the Navier-Stokes equations.

This chapter presents methods to obtain the geometry and flow boundary conditions that are utilized in the following chapters. The geometry plays an important role since CM causes a stenosis-like obstruction to CSF. This chapter briefly summarizes a basis for this work presented in detail in Kalata's Master's Thesis [1] and continues a comparative analysis of CFD results from a healthy subject versus two patients before and after decompression surgery. This chapter provides a baseline for the three following chapters with respect to how MRI information is used to analyze CSF flow within the cervical SAS.

In current medical practice, when the MRI images of a CM/SM patient are analyzed by a radiologist, abnormal geometry of the brain and spinal cord as well as complex CSF flow features of can be detected. A diagnosis can be reached when these geometric abnormalities are combined with symptoms and various tests that are performed on the CM/SM patient. With engineering tools, the quantification of geometrical features in SAS and CSF flow characteristics can be made consistent and could possibly become a useful tool for the evaluation of the patient's condition.

Fluid flow resistance can be computed based on the flow rate inside a conduit and pressure drop across it. An electrical analogy for the resistance can be applied to the CSF flow problem and is used in other areas such as heat transfer. The hydrodynamic resistance can be useful to assess the pressure drop due to geometric blockage that is thought to play a role in the pathogenesis of CM and SM.

In this section, the resistance computed using a 3D CFD simulation was compared with less sophisticated 1-D methods. Similar to the 3D CFD, each was based on the *in-vivo* geometry of SAS and CSF flow waveforms obtained via MRI. The 1-D results showed similar trends to 3-D CFD results.

2.2 Methods

2.2.1 Initial Considerations

SAS geometry is complex, therefore, a numerical grid is difficult to obtain. There are limitations due to meshing technologies and computational hardware. Various simplifications were necessary in order to simulate cervical SAS with CM constrictions. In the present research, five different cases were investigated computationally focusing on the upper region of the cervical SAS and lower region of the foramen magnum (FM). The first case was a healthy subject; cases two and three were from one patient before and after surgery. Cases four and five were from a second patient before and after surgery, respectively. This chapter focuses on these five cases and compares them by analyzing the pulsatile flow resistance. For consistency and clarity, the CM patient cases are abbreviated in the text. "CP1-pre" and "CP1-post" refer to the first CM patient before and after surgery, respectively. Similarly, cases of the second patient before and after surgery are referred to as "CP2-pre" and "CP2-post" respectively.

2.2.2 MRI Measurements

The MRI scans for all cases were performed on a 1.5 Tesla scanner (Signa, General Electric Medical Systems, Milwaukee, WI). The anatomy scans were obtained with a vascular time-of-flight technique and consisted of 2-D images along the spinal canal oriented axially. Each CSF velocity measurement consisted of 32 cardiac gated sequential pcMR images.

The healthy volunteer was a 21-year-old male and had several MRI scans. The anatomy scan of the healthy volunteer extended from the bottom of the sacral region of the spine up to the brain to the bottom of the cerebellum. The velocity measurements were obtained at numerous axial locations including the second cervical vertebrae (C2) level.

Both patients with CM were 35-year-old males. Before and after their surgeries, they were scanned for geometry and velocity. Their MRI geometries were obtained in the sub-cranial region ranging from the upper cervical region, through the FM to the lower part of the cerebellum. The velocity MRI measurement for each case was at the C2 level.

2.2.2 Geometry and Meshing

The three-dimensional (3-D) reconstruction process for sub-cranial SAS was performed using MIMICS (Materialise's Interactive Medical Image Control System, versions 6.1-7.0, Ann Arbor, MI). The model reconstruction methodology is based on thresholding for specific gray-scale range, masking the specific regions, and if necessary manual editing. The sub-cranial SAS regions had annular shapes that consisted of two boundaries (inside-the spinal cord and outside-the vertebrae) as the meshing algorithm. These 3-D reconstructions were converted to sliced format (SSL–StrataSys Layer), which is used in rapid prototyping.

Every 3-D reconstruction provided a realistic SAS geometry. See an example of SAS reconstruction in Figure 2.1. Some aspects of the SAS geometry had to be omitted such as the nerve roots, denticulate ligaments and blood vessels. They were omitted because axial MRI did not pick up these features completely and more importantly the annular geometry had to be maintained. To maintain the annularity of the SAS, minor alternations were performed in the blockage regions. If all features of the SAS anatomy were included, the computational grid with these geometrical features would require a very dense mesh and hence, highly advanced meshing techniques and computational power. Both were not available to the author.

A smoothing process was applied to all SAS geometries. Smoothing was necessary for removing the roughness, bumps, and sharp edges, which are not expected to be present in an in vivo geometry such as the CSF space. The algorithm for smoothing was developed in FORTRAN. More details on the methodology were published by Yedavalli et al. [39].

The computational grid was created using MATLAB (Releases 11 and 12). This program reconstructed the points, called vertices, which formed the outer and inner boundaries of the annular SAS. For each slice, this reconstruction created an equal number of vertices. These vertices were used to create the mesh cells forming the hexahedral mesh of the model. This code created a file with mesh commands for the CFD package, STAR-CD (Versions 3.10A and 3.10B, adapco, London, England). This code was written by Seung-Eun Lee and described elsewhere [40, 41]. All meshed geometries are shown in Figure 2.2. A significant narrowing of the SAS due to the CM in CP1-pre, CP1-post and CP2-pre in the top portion of geometries was observed. In contrast, more space for the CSF flow is noticed in healthy and CP2-post cases.

2.2.3 CSF Flow Measurements

Each flow waveform was obtained from the set of 32 PCMR images representing the flow during one cardiac cycle. These images contained electronically encoded velocity data in the form of pixel grayscale intensity. For each pcMRI in the series, the field of view was the same, a 256x256 pixel array. The pixel size was determined by dividing the field of view by 256. The flow waveforms were obtained by integration of the CSF flow domain for each image in the set, which was chosen for each of the series. The methods for obtaining flow waveforms from pcMRI were reported by Alperin et al. [42, 43].

Flow waveforms of all cases were obtained with a same method using MRView described in Section 2.3.4 (Figure 2.3). All were acquired at the C2 level. The magnitudes of peak systolic flow for the healthy volunteer, CP1-pre, CP1-post CP1-pre- and CP2-post cases were 177, 180, 218, 220, and 236 ml/min, respectively. The magnitudes for diastolic peak flow were 110, 117, 162, 131, and 115 ml/min for healthy, CP1-pre, CP1-post, CP2-pre and CP2-post cases, respectively.

2.2.4 MRView

MRView is a software package developed with MATLAB to obtain flow waveforms from pcMRI measurements. It is based on the integration of flow by selecting the flow domain (Figure 2.4A). Besides calculating flow waveforms, additional features of the MATLAB graphical user interface were included: visualization of MR data for each time step within the cardiac cycle, zoom in/out, image translation within zoomed area, contrast variation within a set of minimum and maximum values, different visualization techniques of velocity distribution for

each time step, and animation of the velocity during the cardiac cycle using the MR images or 3-D plots.

The key feature in this program is the ability to mask, or choose, the specific geometry of the flow domain. By masking the specific pixel on the MR image, the location of this pixel was stored and its color changed. The option of masking and unmasking the flow region with pixel arrays of 3x3, 5x5, and 7x7 was available for faster processing. If there was a pixel with high flow domain uncertainty, a supporting tool for picking the flow region of interest was available. To resolve this uncertainty, full velocity data of the cardiac cycle was loaded; that is, the velocity as a function of time for each pixel in the cardiac cycle was displayed. Since the flow waveform was expected to be of a certain form, examination of the velocity waveform for a specific pixel within the flow region proved to be a helpful tool (Figure 2.4).

Another useful feature for masking the geometry within the region of interest was initialization of masked pixels. The MR image that clearly represented the flow region, such as peak flow within the cycle, was used as a reference for picking the flow region. Instead of initialization by selecting pixels one by one from scratch, the certain low- and high-threshold velocity values for the mask were set. All pixels were masked, as initialized with velocity higher than the low-threshold value and lower than the high-threshold value. After the initialization, a "filtering" process was necessary in order to eliminate unnecessary pixels. Once the region of flow was selected (Figure 2.4A), an option for saving that region was available. In case one, it was necessary to return to this flow region to redefine it.

Based on this chosen region, the velocity was visualized (Figure 2.4A) and animated. But, most important, the flow waveform was obtained. The process involved integration of the velocity over the picked region for an entire cardiac cycle (Equation 2.1 and Figure 2.4A).

$$Q(t) = A_{pixel} \sum_{i=1}^{n} V_i(t), \quad \text{n = number of masked pixels} \tag{2.1}$$

An additional option was created for obtaining the Fast Fourier Transform (FFT) coefficients (Equations 2.2-2.5) that were used for the input boundary condition for the CFD analysis. N represents the number of input points of the sequence.

$$a(0) = \frac{real(FFT(Q(t))_1)}{N} = mean(Q(t)) \tag{2.2}$$

$$b(0) = \frac{imag(FFT(Q(t))_1)}{N} = 0 \tag{2.3}$$

$$a(i-1) = \frac{2}{N} real(FFT(Q(t))_i), i = 2,3,..., \frac{N}{2} \tag{2.4}$$

$$b(i-1) = -\frac{2}{N} imag(FFT(Q(t))_i), i = 2,3,..., \frac{N}{2} \tag{2.5}$$

In order to obtain the FFT coefficients, equations 2.6 to 2.8 were used initially in the Fortran program (initial CFD studies) or MATLAB (more recent MRI and CFD studies).

$$FFT(Q(t)) = \sum_{n=1}^{N} Q(n) \cdot e^{-j2\pi(k-1)(\frac{n-1}{N})}, 1 \le k \le N \tag{2.6}$$

$$Q(n) = \frac{1}{N} \sum_{k=1}^{N} FFT(Q(t)) \cdot e^{j2\pi(k-1)(\frac{n-1}{N})}, 1 \le n \le N \tag{2.7}$$

$$Q(n) = \frac{1}{N} \sum_{k=1}^{N} a(k) \cos\left(\frac{2\pi(k-1)(n-1)}{N}\right) + b(k) \sin\left(\frac{2\pi(k-1)(n-1)}{N}\right), 1 \le n \le N \tag{2.8}$$

2.2.4 Fluid Dynamic Parameters

Using the SAS geometry and CSF flow data for all cases, fluid dynamics parameters were calculated along the spinal canal (zero reference point starts at the base of the brain) as shown in Figure 2.5. The Reynolds number (Equation 2.9) was calculated by using diastolic and systolic flow peaks, which represented the two extremes in the flow waveform. Womersley number (Equation 2.11) was also calculated. This is a dimensionless parameter that defines the nature of pulsatile flow. A low Womersley number (<3) indicates viscous effects will dominate, and a high Womersley number (>10) indicates flow inertia will dominate.

$$\mathrm{Re} = \frac{V_{mean,peak} D_h}{\nu} = \frac{Q_{peak} D_h}{\nu A_{CS}}, \text{ Reynolds number} \tag{2.9}$$

$$\nu = \frac{\rho}{\mu}, \text{ kinematic viscosity} \tag{2.10}$$

$$\alpha = \frac{D_h}{2}\sqrt{\frac{\omega}{\nu}}, \text{ Womersley number} \tag{2.11}$$

$$\omega = \frac{2\pi}{T}, \text{ angular frequency} \tag{2.12}$$

In order to calculate these parameters, the cross-sectional area (A_{CS}), wetted perimeter (P_{wet}), and hydraulic diameter (D_h) were computed. Both A_{CS} and P_{wet} were used to obtain D_h as shown in Equation 2.13 and described by Kalata [1]. The method described by Kalata's work [1] would only apply to continuously annual structures that were used for this chapter (Figure 2.2) and would become inaccurate in complicated geometries.

$$D_h = \frac{4A_{cs}}{P_{wet}} \tag{2.13}$$

2.2.5 3-D Flow Simulations

Flow simulations were performed using commercially available CFD software (STAR-CD version 3.1). This software uses a finite volume flow approximation and was applied to all cases. The setup of the problem consisted of mesh creation, indication for transient simulation, specification of boundary conditions, specification of time-step intervals and their quantity, and indication of computational methods and output preferences. All geometries were treated as a rigid domain, having an inlet boundary condition (IBC) at one end (the cervical spine), and a constant pressure boundary condition (CPBC) at the other end (sub-cranial region). The IBC was specified as an unsteady blunt profile velocity based on the FFT coefficients from the flow waveform measured at C2 level. For all cases, extensions were added at the IBC side. For the Healthy, CP2-pre and CP2-post cases, additional extensions were added at the CPBC. The purpose of these extensions was to reduce end effects in the flow domain. The inner and the outer walls had a no-slip condition. The density and viscosity were 1000 kg/m^3 and 0.001 $N \cdot s/m^2$, respectively. Each case was calculated for at least four flow waveform cycles (four periods) to ensure the repeatability of the results. For each case, the computational time interval (times step) was 0.005 s. Samples of velocity data are given in Figure 2.6. The pressure drop was computed between C2 level and 2.5 cm above C2 level (Figure 2.7).

2.2.6 Longitudinal Impedance

Longitudinal impedance (Z_L) in Equation 2.14 is a representation of pulsatile flow resistance. For each case, FFT was performed on the flow waveform (Q) and on the pressure drop (ΔP) that resulted from CFD calculations or bench-top experiments.

$$Z_{L_n} = \frac{FFT(\Delta P)}{FFT(Q)} = \frac{\Delta P_n}{Q_n} \tag{2.14}$$

The FFT coefficients of pressure difference were divided by the flow waveform FFT coefficients for each harmonic. Both were in complex form. The result was a complex number representing the longitudinal impedance for each harmonic (Equation 2.15). The longitudinal impedance modulus (M_L) and the phase angle for each harmonic were calculated from Equations 2.16 and 2.17 (Figure 2.8).

$$C_n = A_n + iB_n \tag{2.15}$$

$$M_{L_n} = \sqrt{A_n^2 + B_n^2} \tag{2.16}$$

$$\phi_{L_n} = \tan^{-1}\left(-\frac{B_n}{A_n}\right) \tag{2.17}$$

To obtain one characteristic value of CSF resistance, the resulting M_L curve was integrated via calculation of the area under the curve over the range of frequencies (converted from harmonics using heart rate) as shown in Equation 2.18. The range of frequency was 1 - 8 Hz, where *k* is the number of data points on the curve within the 1-8 Hz range (Figure 2.9).

$$M_{L,1-8} = \int_1^8 M_{L,f}(f)df = \sum_{n=1}^{k-1}(f_{n+1} - f_n)\left(\frac{M_{L,n}+M_{L,n+1}}{2}\right) \tag{2.18}$$

2.2.7 Womersley and 1-D Unsteady Annulus Flows

Pressure drop and its resulting M_L was computed for all five cases with Womersley Flow (WF) and unsteady (pulsatile) annulus flow (UAF) and both methods are summarized in Figure 2.10. Figure 2.10 shows flow-pressure drop relations derived from the Navier-Stokes equations. Both methods are unsteady 1-D calculations that result with modified Bessel functions (see Figure 2.10 and appendix A1). Similarly to 3-D simulations (3DS), an input C2 flow was

decomposed into FFT coefficients and used as a harmonic input to compute the pressure drop for the cross-sectional area (A_{CS}) of SAS.

This method employed A_{CS} values obtained from multiple axial SAS locations between the C2 level and 2.5 cm above the C2 level (same distance as in 3DS). The representative diameters (D) were computed based on A_{CS} values at multiple axial locations. For both WF and UAF methods, α was based on a fictional representative D, which was computed using the definition of area for a circle ($A_{CS}=0.25\pi D^2$). For the UAF method, additional parameters of inner and outer diameters (D_i and D_o) were necessary to accommodate the geometrical changes within A_{CS}.

The unsteady pressure drop was calculated for every cross-sectional slice along spinal canal (axial direction) in which A_{CS} varies with location. Each slice has a finite thickness (Δz). The final pressure drop calculation was a summation of pressure drops for each slice location. Since both 1-D methods included Bessel functions that are represented in a mathematical series, MATLAB was employed to compute pressure drop and resulting M_L.

2.3 Results

2.3.1 CFD Results Summary

The healthy geometry had the largest space in the FM region (Figure 2.1). It had no sign of cerebellar blockage. The CP1-pre and CP1-post cases had clearly defined blockages. The postoperative geometry for this case had partial relief in the space below the cerebellar tonsils. CP2-pre case had a significant blockage as well. The CP2-post had space enlargement in the FM region that is shown in Figure 2.2. CSF flow waveforms (Figure 2.3) at the C2 level for all five cases indicated similar traits. The systole peaks varied for 3 to 4 ml/s, and the diastole peak

varied from -2.8 to -1.8 ml/s. The periods for the healthy, CP1-pre, CP1-post, CP2-pre and CP2-post were 0.834, 1.071, 0.984, 0.855, and 0.780 s, respectively.

The cross-sectional area was the main factor that caused differences in hydraulic diameter, Womersley number and systolic Reynolds number (Figure 2.5). The major differences were observed in the FM region as previously referred to in Figure 2.2. In the healthy case, the FM region was unaffected by the cerebellum and therefore its cross-sectional area was the largest. This led to the largest hydraulic diameter, the lowest Reynolds number, and the highest Womersley number. For both patient cases, the cross-sectional areas in the FM region were the smallest with the exception of the CP2-post case which had a brief section of the FM region with a large area. In all five cases, the cross-sectional areas were similar in the cervical region of SAS. The significant differences can be noticed in the systolic Reynolds number curves, where in addition to cross-sectional areas, the systolic flow peaks were different for each case.

The CFD simulations (see Figure 2.6) have shown similar characteristics to Womersley Flow, where in tight spaces, the velocity profiles were parabolic and in larger spaces, the profiles were flat with horn-like shapes near the walls when in cyclic transition. As expected, in tighter spaces the CFD velocities were higher. The pressure drop obtained via CFD (between C2 level and level 2.5 cm above C2 (Figure 2.7) was used to calculate longitudinal impedance modulus (Figures 2.8) as described in the previous section. When integrated from 1-8 Hertz, the healthy, CP1-pre, CP1-post, CP2-pre and CP2-post were 143, 440, 303, 335 and 264 dynes/cm^5 (Figure 2.9). For both patients, the surgery improved the CSF flow resistance. Yet this improvement did not reach the healthy volunteer's resistance value.

2.3.2 1D vs. CFD Comparisons

The 1-D pressure drop computations via Womersley flow and pulsatile annulus flow show similar traits when compared to full 3-D simulations in all five cases. For each case, they generally followed the shape of the 3-D simulations' pressure drop and M_L curves. The healthy volunteer case has nearly identical pressure drop and M_L for all three methods (Figure 2.11 and Table I).

TABLE I.

SYSTOLE AND DIASTOLE TRANSITION PRESSURE DROP PEAKS FOR ALL 5 CASES.

Case	Diastole-Systole Transitions dP peak **3DS, WF, UAF** (100·mmHg)	Systole-Diastole Transition dP peak **3DS, WF, UAF** (100·mmHg)
Healthy	**3.5, 3.3, 3.3**	**-1.5, -1.4, -1.4**
CP1-pre	**8.8, 6.8, 7.6**	**-3.9, -3.1, -2.9**
CP1-post	**9.7, 7.9, 8.2**	**-4.9, -4.1, -4.0**
CP2-pre	**13.6, 12.6, 9.8**	**-4.1, -3.7, -3.0**
CP2-post	**10.3, 9.3, 6.5**	**-3.8, -3.2, -2.7**

3DS: 3-D Simulation, WF: Womersley Flow, UAF: Unsteady Annulus Flow

In all patient cases, the pressure drop curves from 1-D methods did not match the 3DS data as closely as in the healthy case. The main differences were observed in flow transition from diastole to systole where 1-D pressure drop peaks were lower (Figures 2.12 - 2.15 and Table I). In flow transition from systole to diastole, the 1-D pressure drop peaks, and in some cases shapes, did not match the 3DS data. As expected, the M_L curves were consistently different for each method. Only the healthy case had M_L curves from 1-D methods close to the 3DS method (Figure 2.11B). For all five cases, the WF method produced M_L values as straight lines as a

function of harmonics (Figures 2.11B - 2.15B). Similar to the pressure drop results, M_L calculated from 1-D methods were consistently lower than M_L from 3DS.

In all five cases, the integrated values for three different methods were compared case-wise (Figure 2.16A) and method-wise (Figure 2.16B and Table II).

TABLE II.

METHOD-WISE DECREASE OF INTEGRATED M_L VALUES WITH RESPECT TO 3-D SIMULATION.

Case	WF (decrease %)	UAF (decrease %)
Healthy	4%	3%
CP1-pre	33%	26%
CP1-post	20%	23%
CP2-pre	4%	20%
CP2-post	10%	47%

WF: Womersley Flow, UAF: Unsteady Annulus Flow

Table II demonstrates the resistance percentage reduction between the 3-D simulation and 1-D methods. As expected, the healthy case shows the smallest difference in resistance for the two methods. CP1 (both before and after surgery) shows consistent reduction in range of 20-33%. For the CP2 case, the WF method showed resistance value reduction with 4 and 10% before and after surgery, respectively. The UAF method indicated larger value reduction with 10 and 47% before and after surgery, respectively.

Although, the magnitude of the integrated values from 1-D methods did not match the 3DS data, the respective difference trends were similar as shown in Table III. 1-D methods showed higher reduction in resistance in CP2, where 3DS indicated better improvement in CP1.

TABLE III.

POSTOPERATIVE REDUCTION IN LONGITUDINAL IMPEDANCE FROM BOTH PATIENTS - METHOD COMPARISON.

Method	**Patient 1 (M_L Reduction %)**	**Patient 2 (M_L Reduction %)**
3DS	31%	21%
WF	24%	26%
UAF	29%	35%
$(Wo_{ave}/Wo_{ave,healthy})^{-1}$	30%	14%

3DS: 3-D Simulation, WF: Womersley Flow, UAF: Unsteady Annulus Flow.

2.3.3 Normalization

From the Womersley number previously calculated based on cross-sectional area along the length of each case (Figure 2.5), an average value of the Womersley number ($\overline{\alpha_c}$) was calculated for the same region as the pressure drop (C2 level to 2.5 cm above C2 level). These five averages were normalized by an averaged Womersley number from the healthy case ($\overline{\alpha_h}$) and then inverted (Equation 2.19). For simplicity, the inverse of healthy-normalized Womersley number ratio is abbreviated to IHNWN (an acronym).

$$\text{IHNWN} = \frac{\overline{\alpha_h}}{\overline{\alpha_c}} = \left(\frac{Wo_{ave}}{Wo_{ave,heatlthy}}\right)^{-1} \tag{2.19}$$

Similarly, the resistance based on longitudinal impedance modulus, was normalized via the healthy case (no inversion). Both were plotted side-by-side, revealing striking similarities as shown in Figure 2.17.

Similarly to 1-D methods, IHNWN had similar reduction trends (Table III). The post-operative reduction of IHNWN for CP1 was 30%, and CP2 was 14%. The IHNWN values for patients were lower than normalized resistance values. For CP1-pre, CP1-post, CP2-pre and

CP2-post, the reduction percentage values with respect to normalized longitudinal impedance values were 30, 16, 27 and 14%, respectively.

2.4 Discussion and Conclusions

The unsteady flow resistance results from 1-D Navier-Stokes equations demonstrated that 1-D methods can be useful to assess a healthy CSF flow system below the cerebellum to some degree. In cases where the cross-sectional area along the flow path does not change dramatically as in the healthy case, the 1-D method proved to be a good approximation. It is necessary to analyze more healthy volunteers to determine if Womersley Flow or Unsteady Annulus Flow methods are reliable to analyze the CSF flow resistance in the SAS.

In flows of CM patients where SAS is malformed due to cerebellar descent, 1-D methods did not match the CFD results well. However, from a comparative point of view, 1-D methods rendered similar resistance reduction trends when compared before and after surgery. Based on the comparative assessment, the reduction difference in resistance magnitude between full 3-D simulation and 1-D methods varied from 4% up to 47%. The average resistance value reduction was 23%. Considering large changes in the cross-sectional area of malformed SAS geometries and the exclusion of secondary flow effects (1-D assumption), the under-estimated values of flow resistance have the potential to be used as a quick preliminary assessment of the hydrodynamic environment in CM patients.

An interesting correlation was observed with healthy-case normalized values of Womersley number versus CFD resistance (Figure 2.17). The post-surgical reduction trend was similar (Table III) for both patients. This close correlation confirms that longitudinal impedance, similarly to Womersley number, is strongly dependent on geometrical configuration.

Considering the simplicity of the 1-D methods to obtain the M_L value, the 1-D methods or even Womersley parameter analysis seem to have potential to be incorporated into MRI processing software where both flow and geometry can be obtained with relative ease and analyzed with rapid 1-D methods. As MRI hardware, scanning protocols, and software improves, the process for obtaining representative resistance can be achieved within the same day as the MRI scan. This may prove beneficial to doctors, neurosurgeons, and most importantly patients, where treatment decision can be supported not only by symptoms and MRI geometrical assessment, but supplemented with a thorough hydrodynamic analysis of a patient.

Although full 3-D simulation requires time commitment and resources for computation and post-processing, it could play a supporting role in the neurosurgeon's decision and planning for surgery. Further, CFD can serve as a predictive tool for surgery planning by assessing flow resistance in virtually altered SAS.

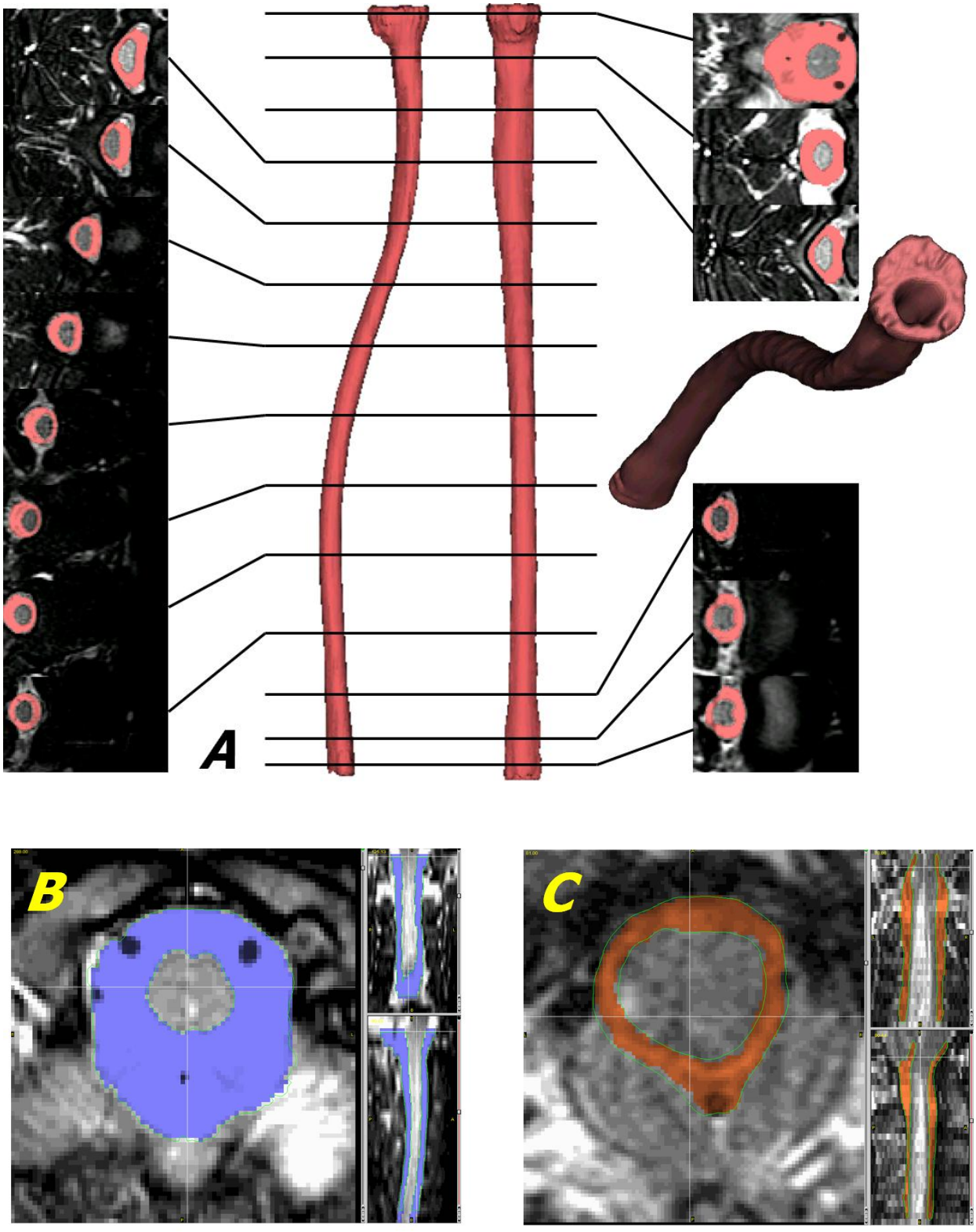

Figure 2.1. 3-D reconstructions from MR images: **A.** reconstruction of SAS in a healthy volunteer's full upper back. **B.** SAS in FM region in healthy volunteer. **C.** SAS in FM region in CP1-pre.

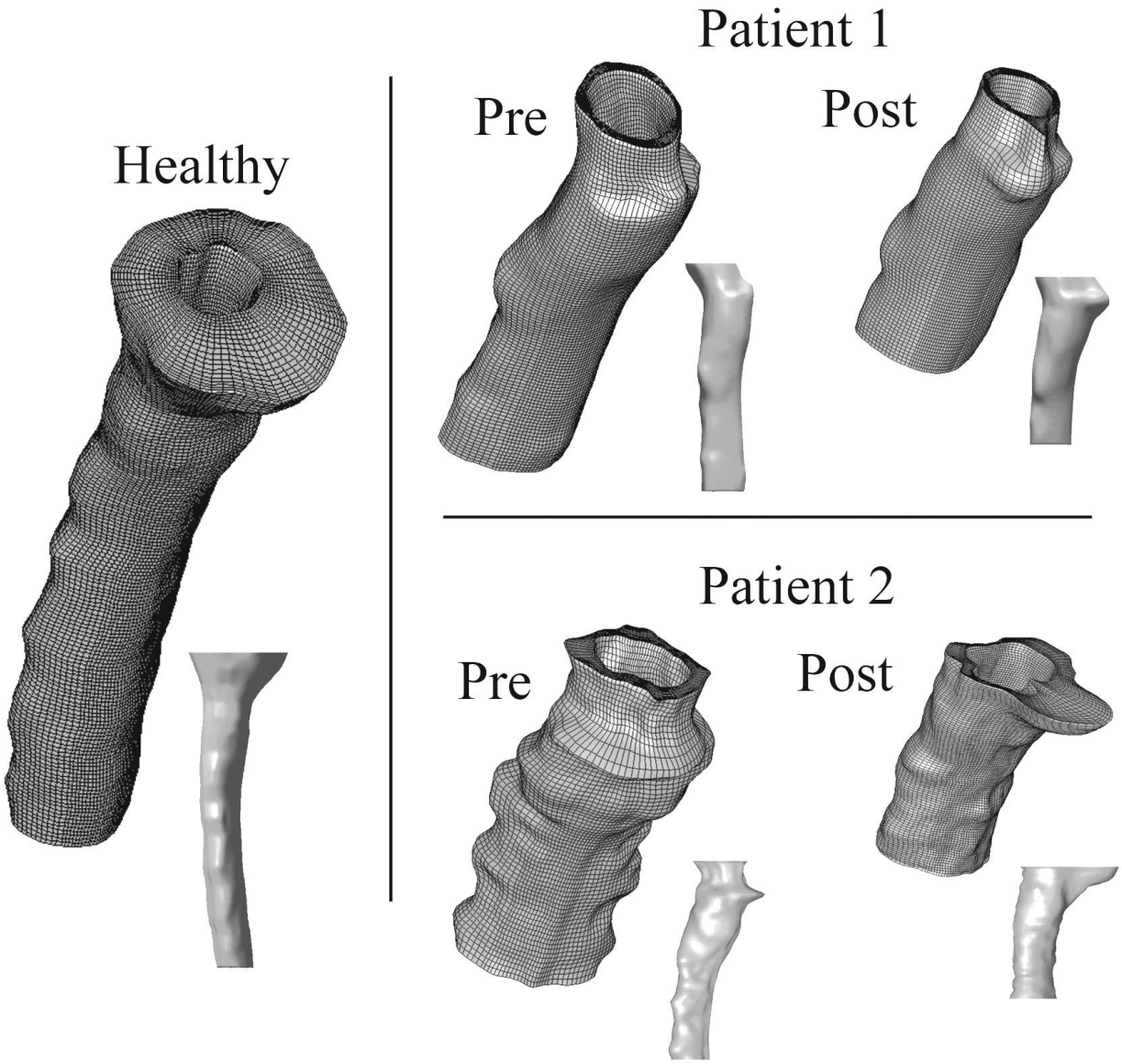

Figure 2.2. Reconstructed and meshed geometries of sub-cranial SAS for a healthy volunteer and two patients before and after surgery (CP1-pre, CP1-post, CP2-pre and CP2-post).

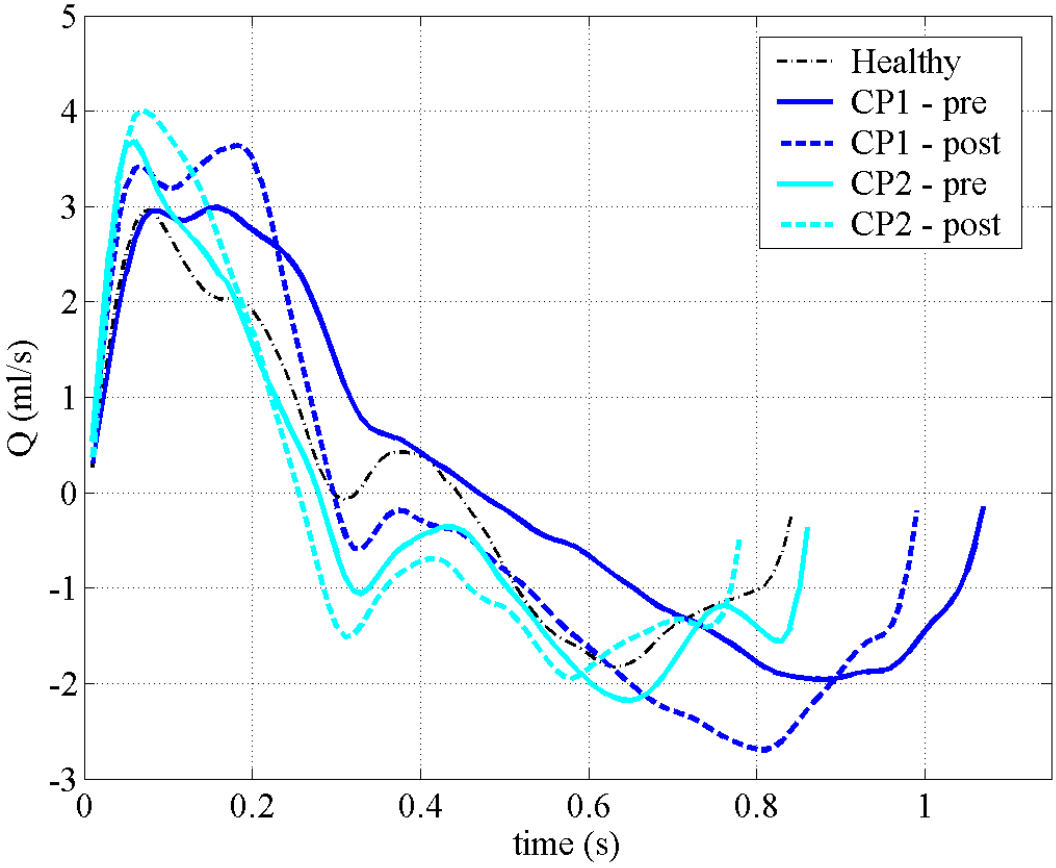

Figure 2.3. CSF flow waveforms at C2 for all cases.

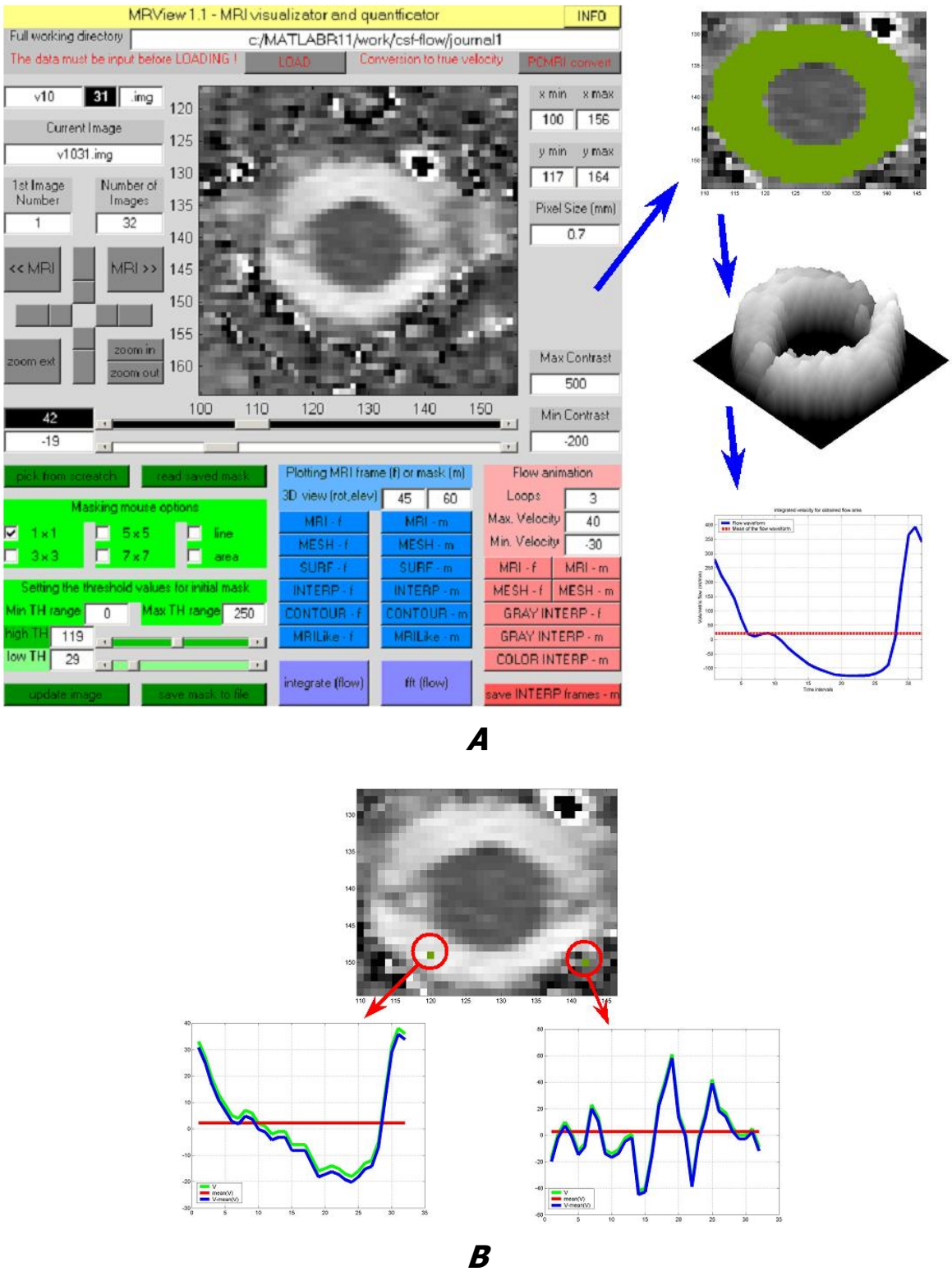

A

B

Figure 2.4. MRView: **A.** GUI and the process for obtaining the flow waveform by masking the flow domain, visualizing the flow, and calculating the flow waveform. **B.** examples for the single pixel velocity during whole cycle for pixel with fluid flow and the pixel with noise.

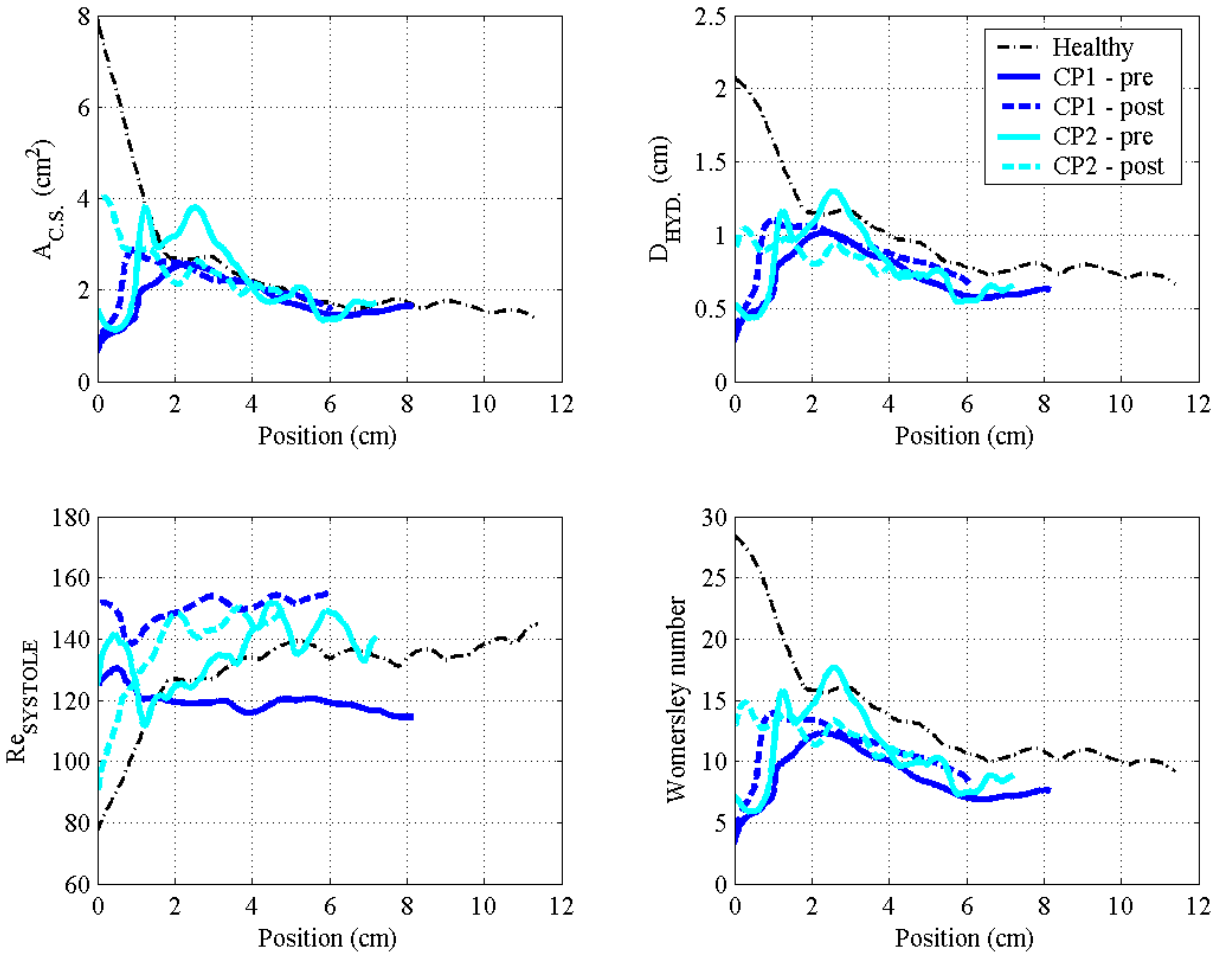

Figure 2.5. Hydrodynamic parameters for all 5 cases.

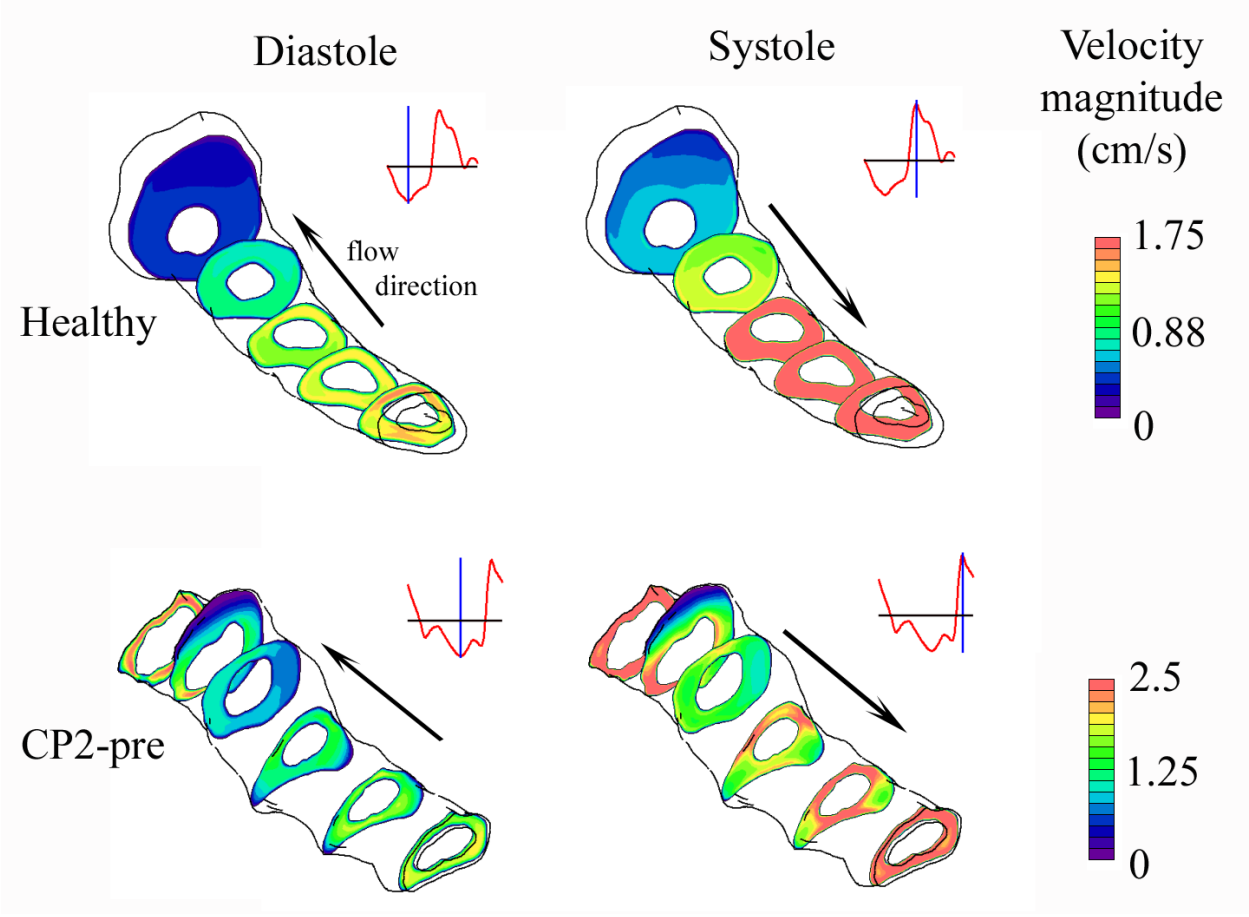

Figure 2.6. Velocity magnitudes at various locations for Healthy and CP2-pre cases at diastolic and systolic peaks.

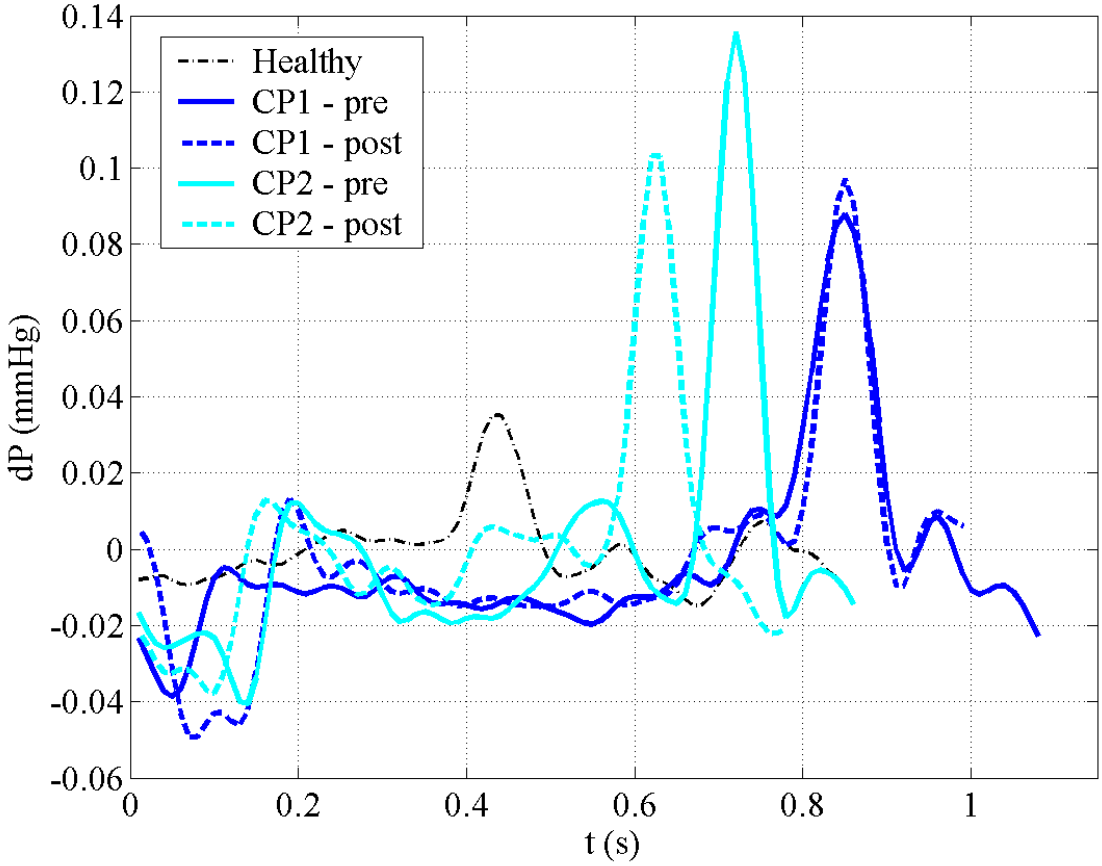

Figure 2.7. Pressure drop for all 5 cases.

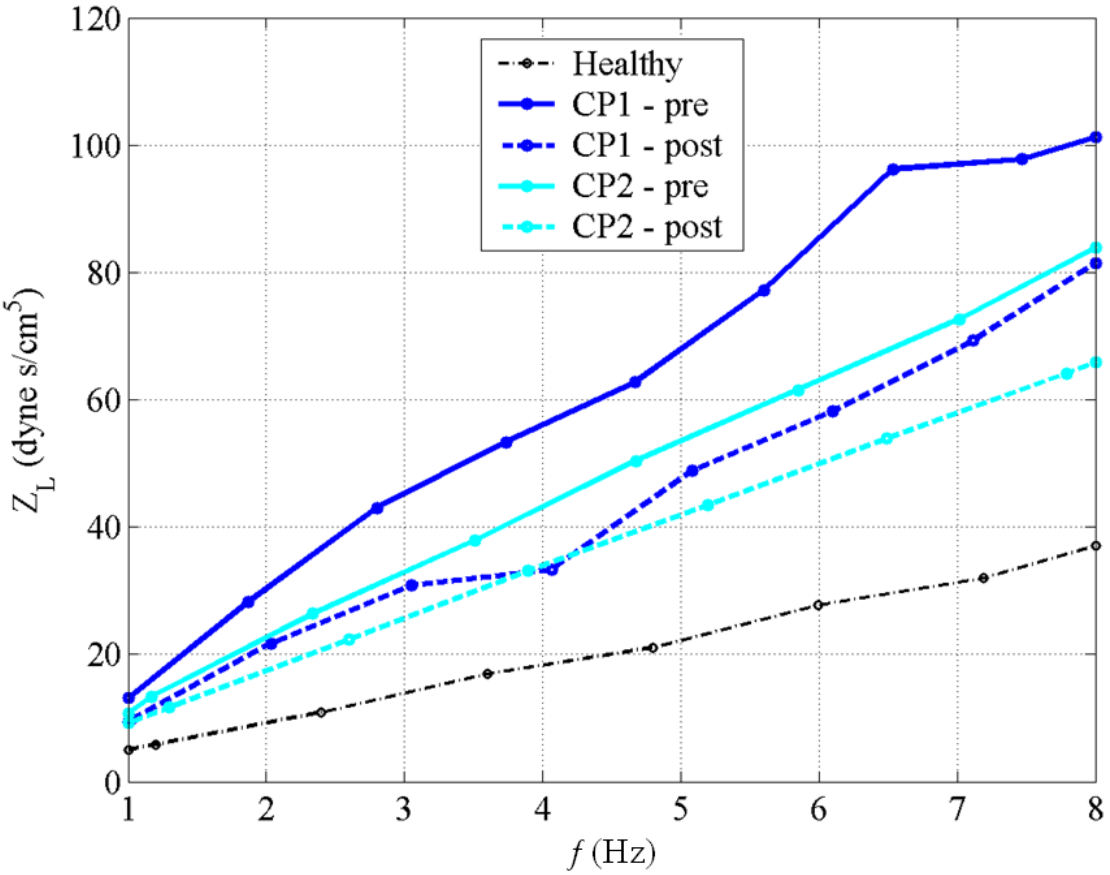

Figure 2.8. Longitudinal impedance for all 5 cases.

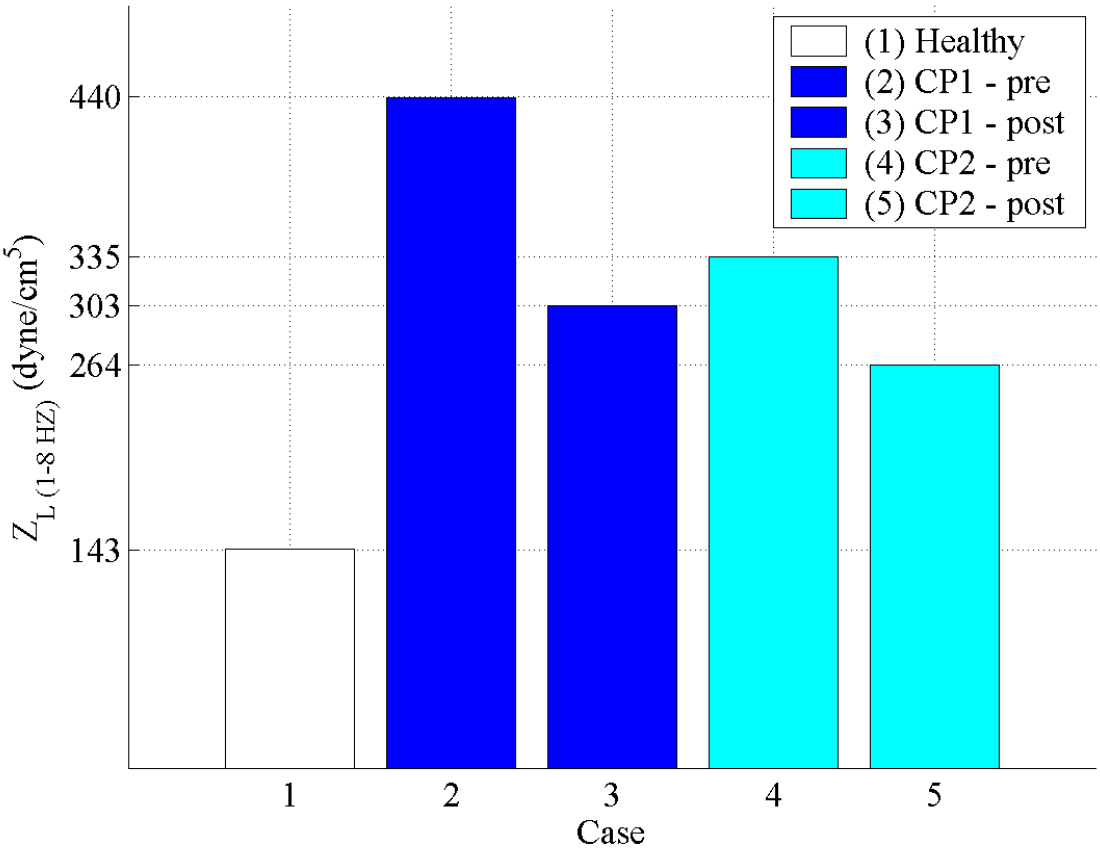

Figure 2.9. Integrated longitudinal impedance for all 5 cases.

Womersley Flow

Womersley Number

$$\alpha = \frac{D}{2}\sqrt{\frac{\omega}{\nu}}$$

ω: angular frequency
ν: kinematic viscosity

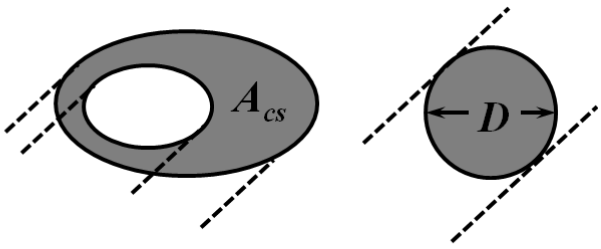

$$R = \frac{D}{2} = \sqrt{\frac{A_{CS}}{\pi}} \qquad Q(t) = \frac{\pi R^4}{i\alpha^2\mu}\left[1 - \frac{2J_1\left(i^{\frac{3}{2}}\alpha\right)}{i^{\frac{3}{2}}\alpha J_0\left(i^{\frac{3}{2}}\alpha\right)}\right]\frac{\partial p(t)}{\partial z}$$

Annular Unsteady Flow

$$r_i = \frac{R_i}{R_o} \qquad R_i = \frac{D_i}{2} = \sqrt{\frac{A_{cs,i}}{\pi}} \qquad R_o = \frac{D_o}{2} = \sqrt{\frac{A_{cs,i} + A_{cs,o}}{\pi}}$$

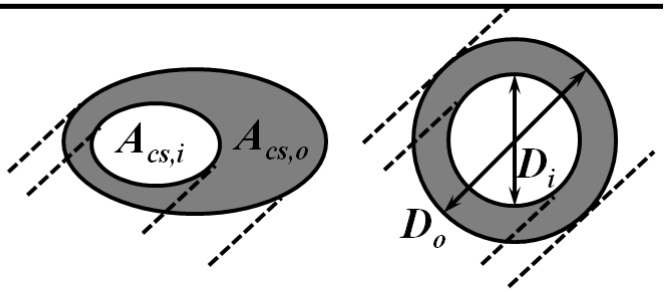

$$Q(t) = \frac{2R_o^4}{i\alpha^2\mu}\left\{\frac{E_1}{i^{\frac{3}{2}}\alpha}\left[J_1\left(i^{\frac{3}{2}}\alpha\right) - J_1\left(i^{\frac{3}{2}}\alpha r_i\right)\right] - \frac{E_2}{i^{\frac{3}{2}}\alpha}\left[Y_1\left(i^{\frac{3}{2}}\alpha\right) - Y_1\left(i^{\frac{3}{2}}\alpha r_i\right)\right] - \frac{1 - r_i^2}{2}\right\}\frac{\partial p(t)}{\partial z}$$

Where E_1 and E_2 are determined via BC conditions

Total 1-D Pressure Drop

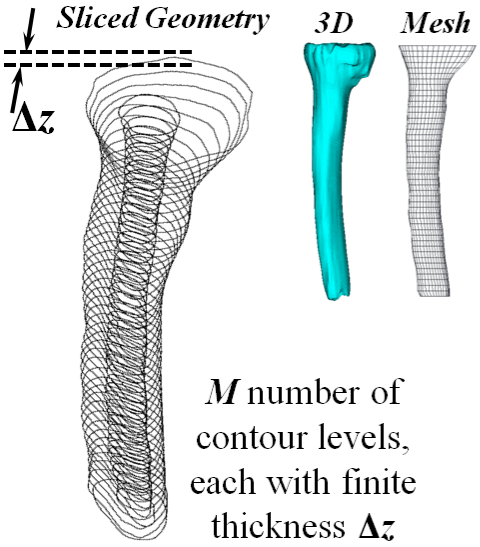

M number of contour levels, each with finite thickness Δz

$$\frac{\partial P(t)}{\partial z} = Ae^{i\omega t} = \sum_{n=1}^{N} A_n e^{in\omega t}$$

N: harmonic order

$$\sum_{n=1}^{N} A_n e^{in\omega t} = \sum_{n=1}^{N} \frac{1}{F_n} C_n e^{in\omega t}$$

$$Q(t) = F\frac{\partial P(t)}{\partial z}$$

C_n: flow input in harmonic form
F_n: harmonic form of the flow equation constant

$$\left.\frac{\partial P(t)}{\partial z}\right|_{total} = \sum_{m=1}^{M} \left.\frac{\partial P(t)}{\partial z}\right|_{m}$$

Figure 2.10. Brief schematic for 1-D methods to calculate total pressure drop.

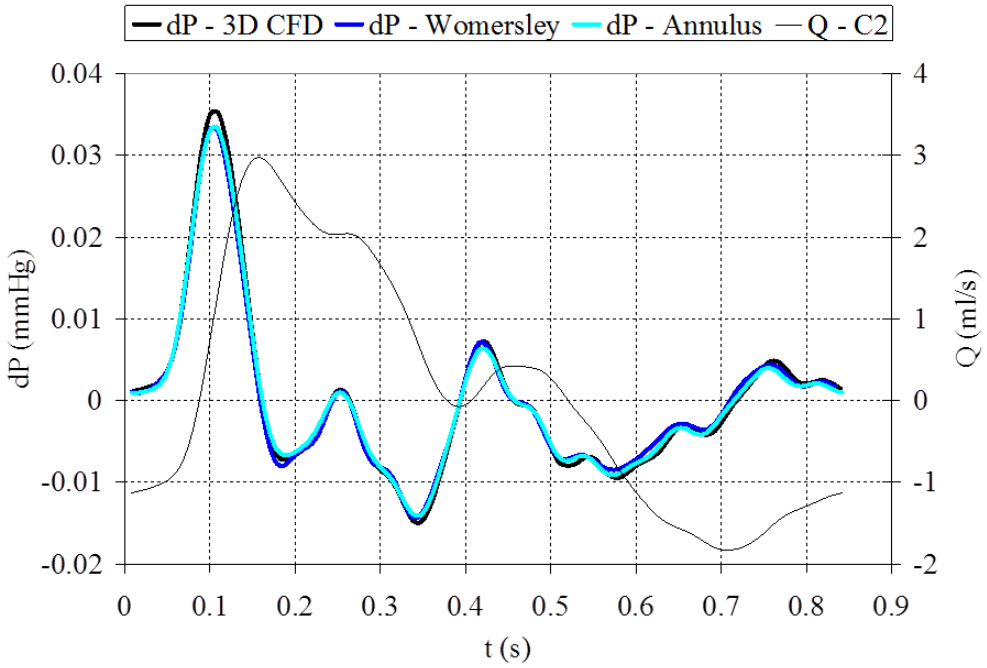

A

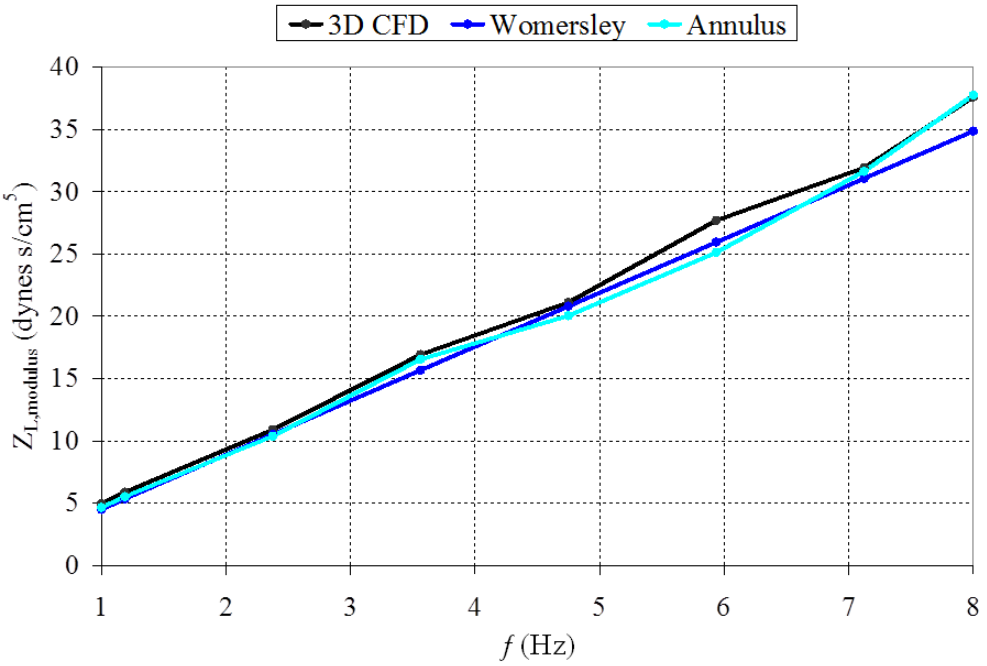

B

Figure 2.11. 3-D CFD versus 1-D computations for healthy case: **A.** Pressure drop and input flow rate. **B.** Longitudinal impedance modulus

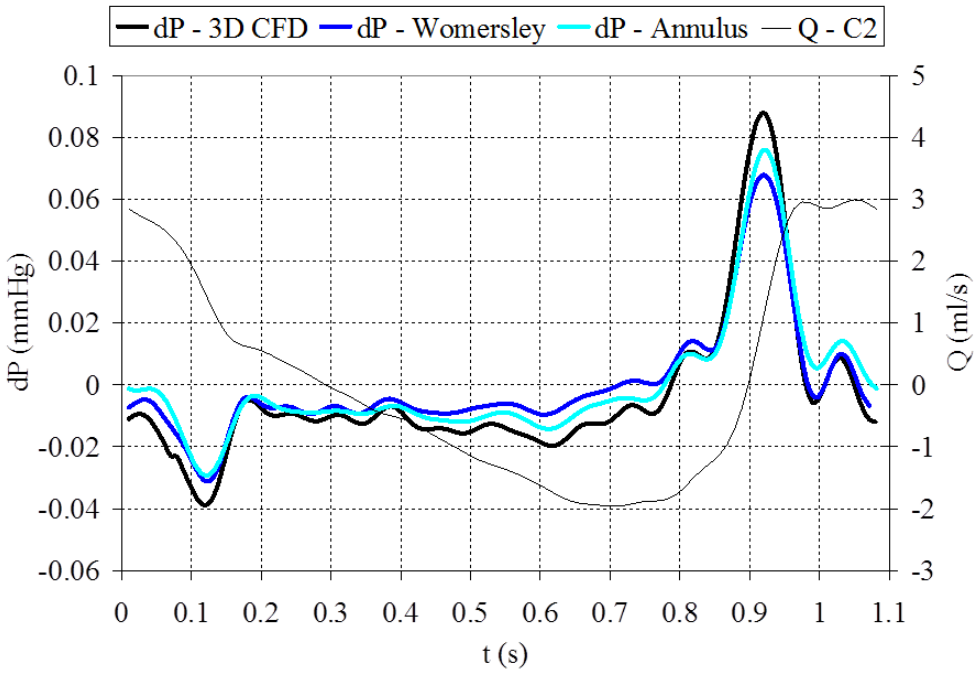

A

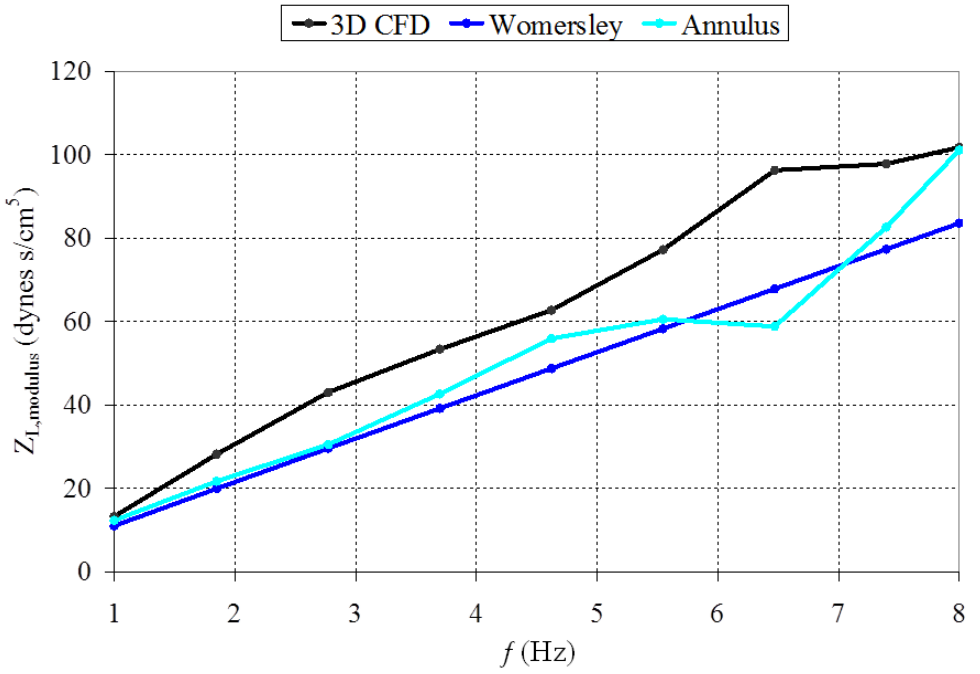

B

Figure 2.12. 3-D CFD versus 1-D computations for CP1-pre:
A. Pressure drop and input flow rate. **B.** Longitudinal impedance modulus

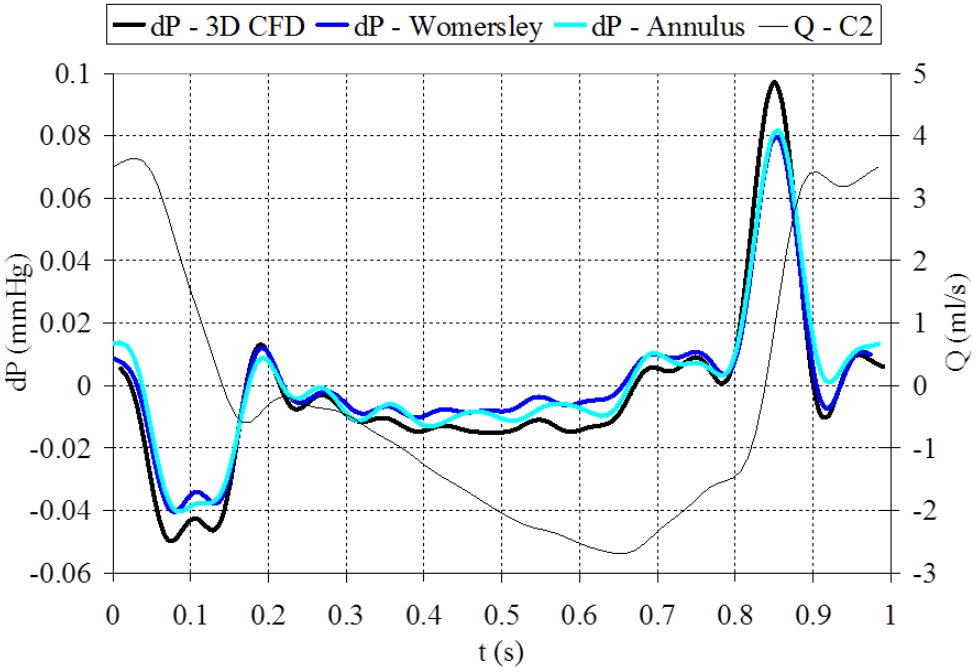

A

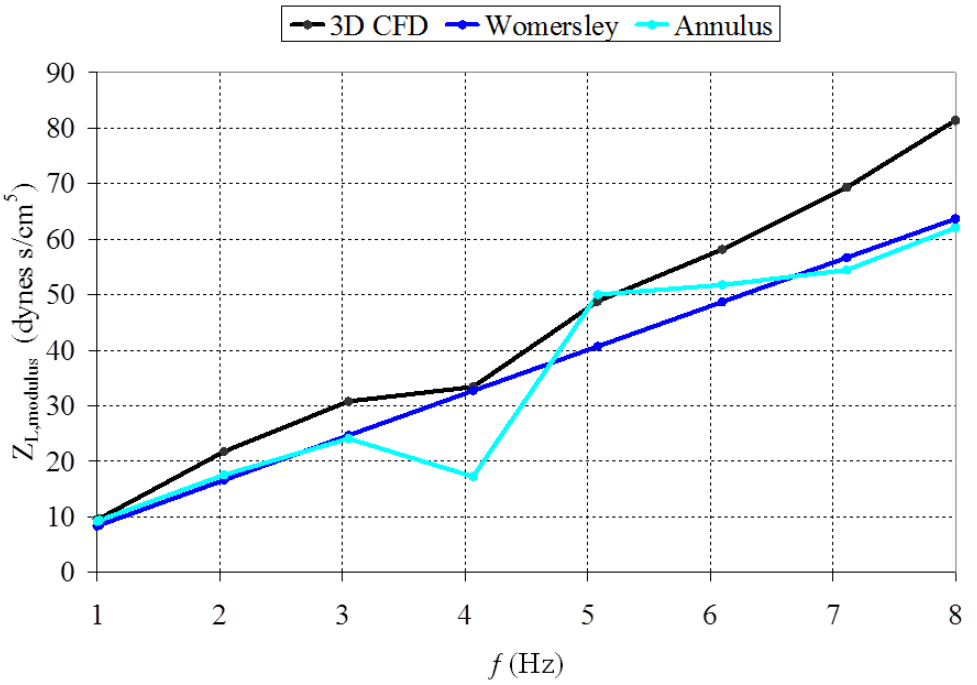

B

Figure 2.13. 3-D CFD versus 1-D computations for CP1-post: **A.** Pressure drop and input flow rate. **B.** Longitudinal impedance modulus

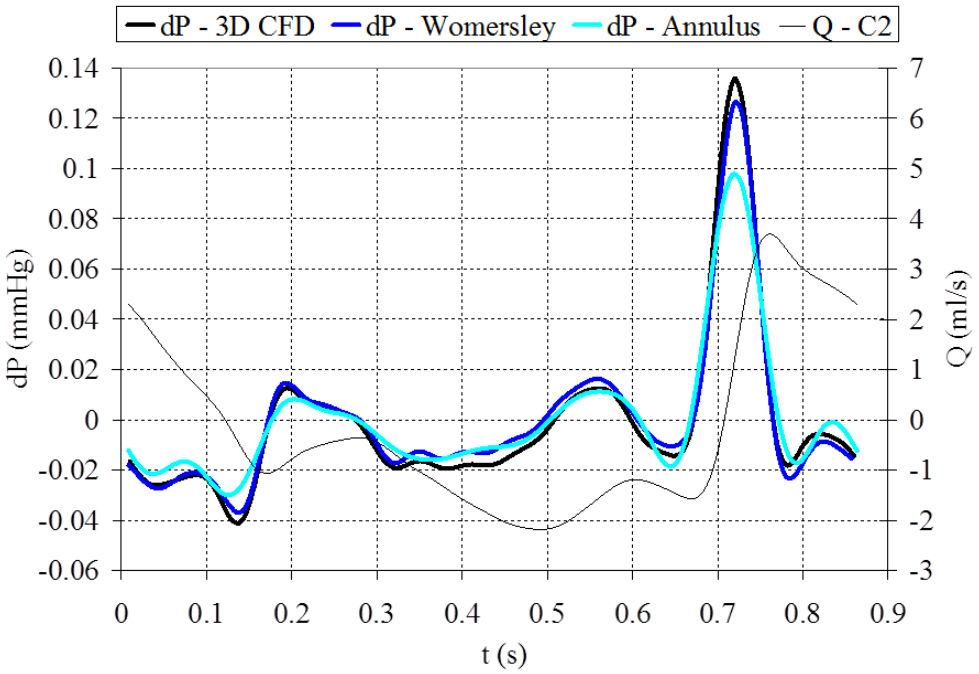

A

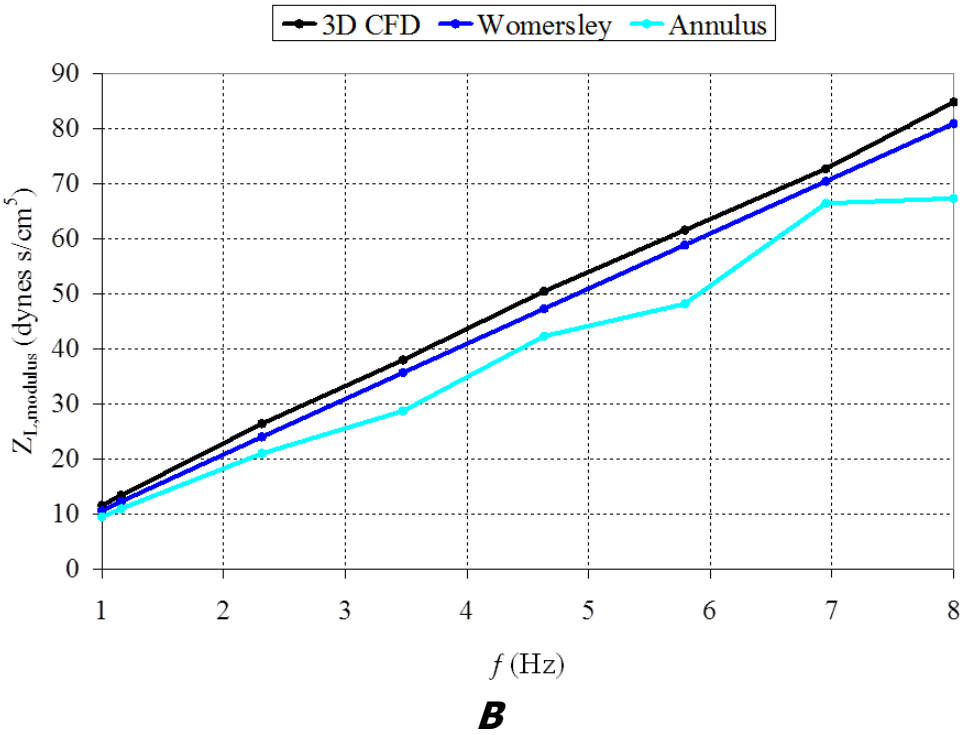

B

Figure 2.14. 3-D CFD versus 1-D computations for CP2-pre:
A. Pressure drop and input flow rate. **B.** Longitudinal impedance modulus

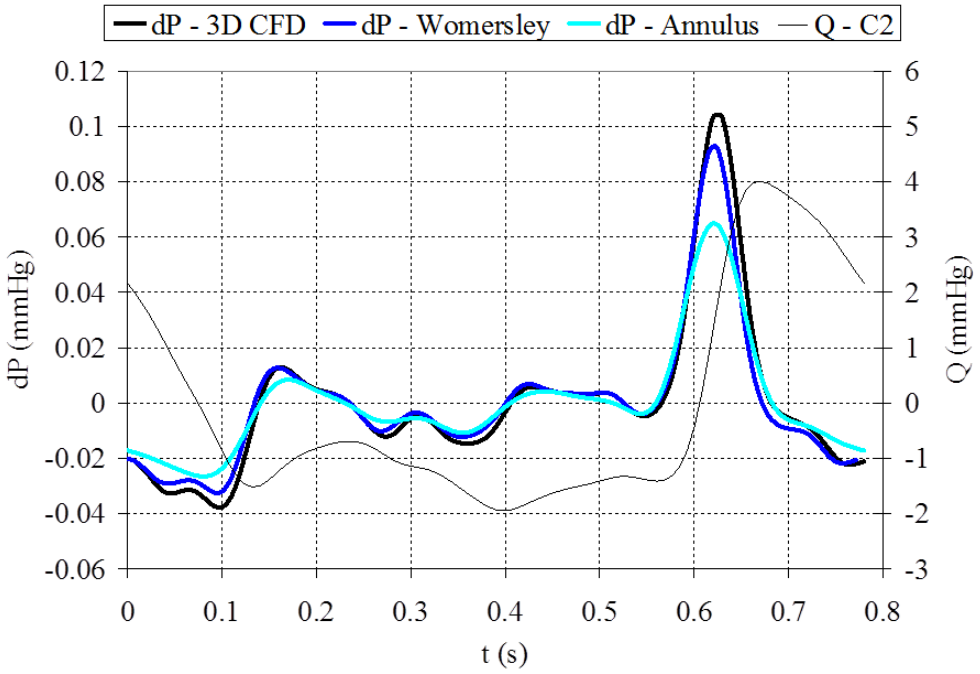

A

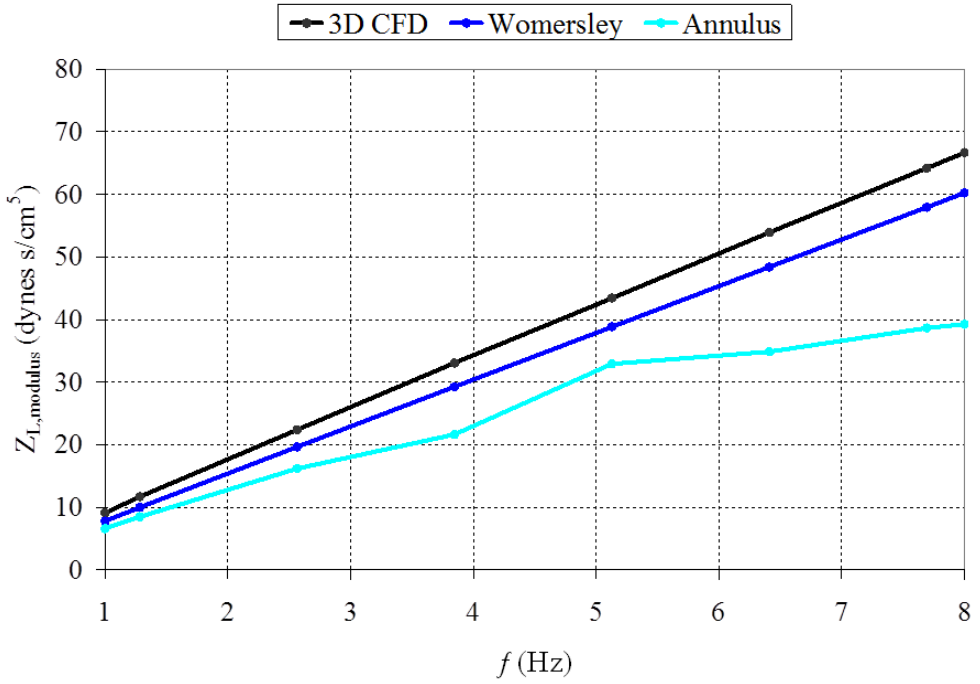

B

Figure 2.15. 3-D CFD versus 1-D computations for CP2-post:
A. Pressure drop and input flow rate. **B.** Longitudinal impedance modulus

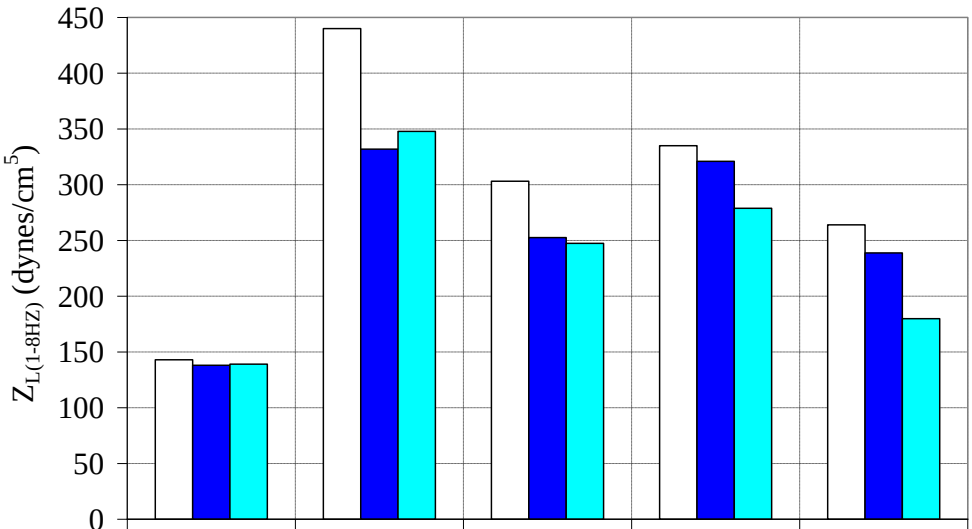

	Healthy	CP1-pre	CP1-post	CP2-pre	CP2-post
3-D CFD	143	440	303	335	264
Womersley	138	332	253	321	239
1-D Annulus	139	348	247	279	180

A

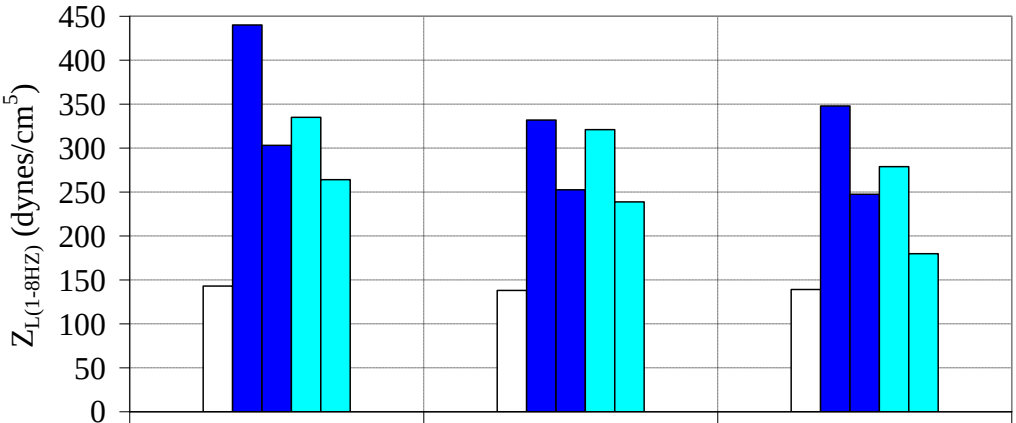

	3-D CFD	Womersley	1-D Annulus
Healthy	143	138	139
CP1-pre	440	332	348
CP1-post	303	253	247
CP2-pre	335	321	279
CP2-post	264	239	180

B

Figure 2.16. Comparison of integrated values of each case for each computational method: **A.** Comparison by grouped cases. **B.** Comparison by grouped computational methods.

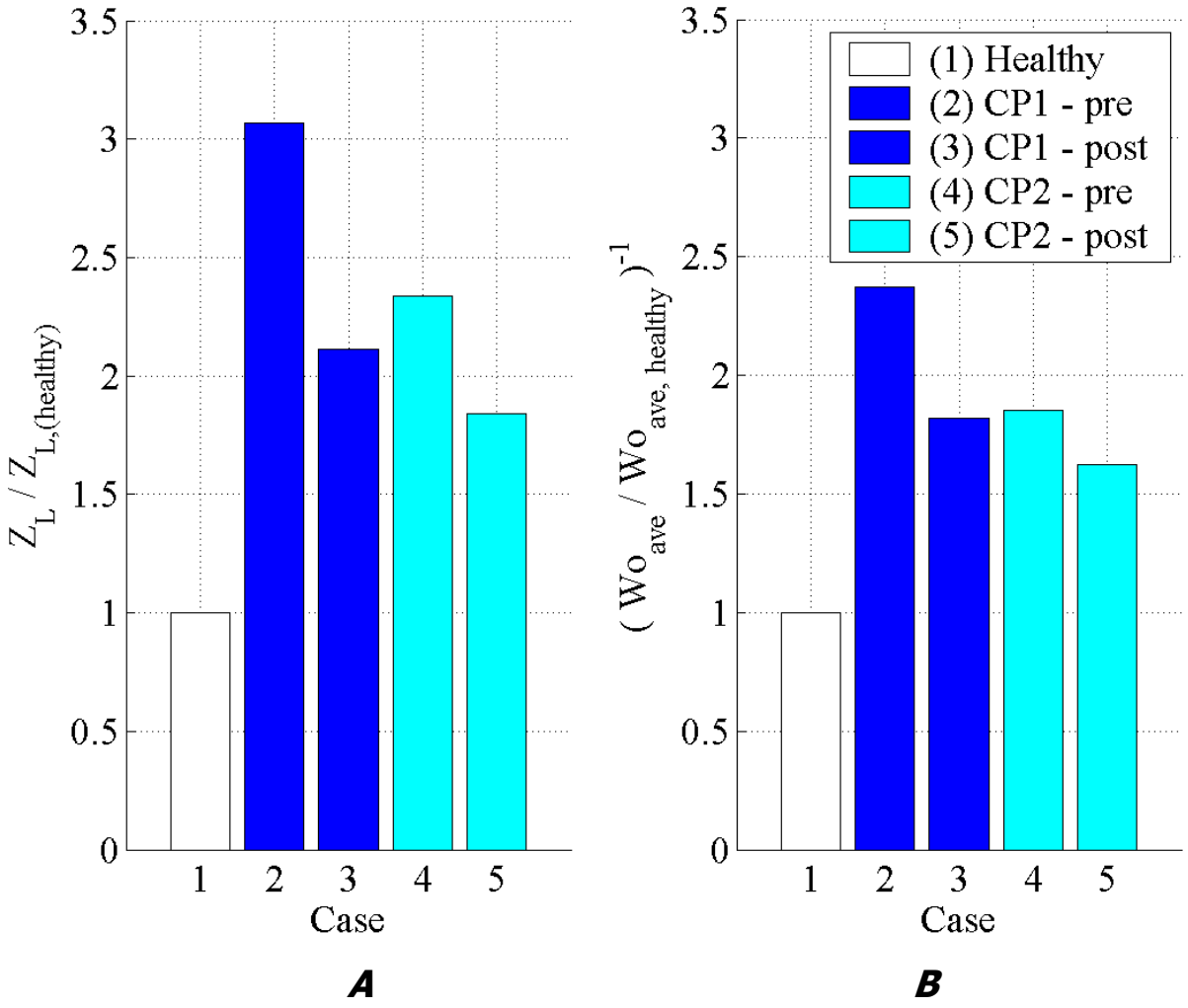

Figure 2.17. Comparison of: **A.** Normalized longitudinal impedance and **B.** Inverse of healthy-normalized Womersley number (right) for all 5 cases.

3. CSF FLOWS – STATISTICAL APPROACH

3.1 Introduction

3.1.1 Motivation

The characterization of the hydrodynamic environment via basic statistical analysis has the potential to provide mathematical tools that may help better understand the complex system of CSF flow with CM blockage. By comparing parameters from statistical analysis of CM patients and healthy controls, detection tools for altered CSF hydrodynamics may be possible.

This chapter is a comparative assessment of CSF flow waveforms obtained from CM patients and healthy volunteers. All waveforms were obtained via pcMRI and processed with MRView described in section 2.2.4. The majority of the CM patients had an MRI scan performed before surgery. Most cases had scans performed at multiple axial levels, which enabled an analysis for flow peak-to-peak differences.

The results showed variations between the volunteers and CM patients. Key features such as percent systole or diastole of a cardiac cycle and systolic peak-to-peak between axial levels were notably different. Also, the shape of the flow waveforms between volunteers and patients analyzed via FFT coefficients showed differences.

3.1.2 Statistical Approach in Literature

Statistical analysis of control subjects' (volunteers') CSF velocity was reported by Henry-Feugeas et al. [44]. This work investigated the statistics of key features during the cardiac cycle in thirty-six volunteers. This work reported CSF velocities at various locations within the SAS cross-section along the spine. At the upper cervical level, the duration of systole during the

cardiac cycle was reported to be 37.0±10.0, 39.1±10.0 and 43.3±7.9 % at the dorsal, lateral and ventral locations of SAS, respectively. Thus, the average duration of systole was 40% of the cardiac cycle. Henry-Feugeas et al. stated that intracranial pulsations seem to be the main source of CSF spinal pulsations.

CSF flow studies in patients with CM were also performed. Work by Bhadelia et al. [45] investigated healthy subjects (n=23), and patients before surgery (n=15) and after surgery (n=10). Similar to work by Henry-Feugeas et al. [44], Bhadelia's et al. work investigated velocity waveforms at various points within the SAS inside the head and spine. The velocity information was obtained from sagittal (side view) planes. Two out of four investigative points were above mid-C2 level and one at the border between the C2 and C3 levels. The fourth measurement point was at the approximate level of FM in the anterior part of the SAS (premedullary cistern). The average systole duration was shown to be slightly shorter in volunteers compared with patients (38% versus 42%). Bhadelia et al. concluded that CSF flow waveform analysis demonstrated abnormalities in CM patients' CSF flow. Further, Bhadelia et al. indicated that the flow analysis implied that CM patients benefited from decompression surgery.

Another study examining flow rates at the C2 level for control subjects (n=18) and CM patients (n=18) was conducted by Hofmann et al. [28]. Hofmann et al. also compared flow waveforms before and after decompression surgery for 10 subjects. In this study, flow waveforms were represented in three regions: anterior SAS region, posterior SAS region, and the spinal cord. On average, the duration of systole for the volunteers was slightly lower than for the patients (34% versus 36%). The systole peaks averaged at 3.4 ml/s for volunteers and 2.9 ml/s for patients. The diastole peaks averaged at 1.45 and 1.7 ml/s for volunteers and patients,

respectively. The authors concluded that the cerebellar blockage located in the foramen magnum of the patients causes "abrupt systolic downward displacement of the spinal cord and impairs the recoil of CSF during diastole" [28].

3.2 Methods

3.2.1 Flow Waveform Data

The MRI data presented in this chapter comes from measurements on six volunteers and eight patients (one pre and post-surgical case, 6 pre-surgical cases only, 1 post-surgical case only). They were all scanned at same facility. MRI was obtained on a 1.5 Tesla Philips Gyroscan NT Intera scanner. Along with pcMRI flow images, anatomy images were obtained. The MRI anatomy scans mainly consisted of axial and sagittal planes in the head and upper cervical regions. The flow measurements were obtained from the patients and volunteers at the second cervical vertebrae level (C2) and depending on the case, at various lower spinal locations (from the fourth cervical vertebrae level to the third thoracic vertebrae level). The pcMRI images were processed using MRView. The process was briefly described in Chapter 2, and in more detail by Kalata [1].

3.2.2 Systole and Diastole - Average and Standard Deviation

All flow waveforms from volunteers and patients were obtained with MRView (Figures 2.1 and 2.2). The raw flow data was then adjusted with a mean value (usually small relative to systole peak) to obtain zero total flow displacement during the cardiac cycle. Based on these flow data points, some basic statistical values were obtained. For both volunteers and patients, the average and standard deviation values were obtained for heart rate, systole peak, systole

duration during the cardiac cycle, diastole peak and the diastole duration. The difference was quantified with an averaged percentage difference formula as shown in Equation 2.1.

$$\Delta = \frac{|X_{\text{Volunteers}} - X_{\text{CM Patients}}|}{(X_{\text{Volunteers}} + X_{\text{CM Patients}})/2} 100\% \quad (2.1)$$

The C2 flow waveforms for both volunteers and CM patients are shown in Figures 3.3 and 3.4. MATLAB was used to interpolate the C2 flow waveform points (number of pcMRI frames within the cardiac cycle) with an FFT interpolation function (command: interpft) to get 100 flow data points for each curve (Figures 3.5A - 3.8A). The data was interpolated with a harmonic order equal to the number of original data points divided by two. This effectively normalizes the time scale such that each flow waveform can be plotted as a percentage of the cardiac cycle. After interpolation, data was adjusted to obtain a mean value of zero total displacement and the same statistics were obtained from the interpolated data. In addition, each FFT-interpolated flow waveform was normalized with the systolic peak, which is usually higher than the diastolic peak (Figures 3.5B - 3.8B).

For the volunteers and the patients, the average and its corresponding standard deviation were obtained at all normalized time points for each FFT flow waveform. This resulted in two representative flow waveforms, one for volunteers and one for pre-surgical CM patients. The averaging was done to both the magnitude and systole-normalized flow data to see effects of systole-normalizing each data points' standard deviation (Figures 3.5C - 3.8C and 3.5D - 3.8D).

3.2.4 FFT Decomposition

To quantify the shape of each flow waveform, the FFT coefficients were examined for each interpolated C2 flow waveform. The real and imaginary FFT coefficients were obtained

using MATLAB, from zeroth to the sixth harmonic order (Figures 3.9 and 3.10). The goal of this analysis was to determine which harmonics dominate in the flow waveforms.

3.2.5 Multi Level Peak to Peak Difference

Volunteers and patients (cases before surgery) with scans performed at multiple axial locations were analyzed to determine the differences between systolic and diastolic peaks at two different axial locations. Systolic and diastolic peaks were identified as described in Section 3.2.2. All subjects had scans performed at the C2 level. Unfortunately, the second level below C2 was not always obtained at the same location for each subject. The second scan level ranged from cervical nerve level at C7 to nerve thoracic level at T2 (Figures 3.1, 3.2 and 3.11).

To correct for differences in the location of the second scan, a correction factor (CF) was introduced to adjust the peak-to-peak differences (systolic peak-to-peak flow difference - SP2PdQ, diastolic peak-to-peak flow difference - DP2PdQ) based on an assumption of linear change in flow along the flow axis. The CF factor represents an interpolation or extrapolation multiplier adjusted by the length scale as shown in Figure 3.11. The CF referenced position is at the C8 level. Thus, systolic and diastolic peak flow differences (SP2PdQ and DP2PdQ) were multiplied by a CF factor of 1.13, 1.00, 0.83, or 0.67 for data at C7, C8, T1 or T2, respectively.

3.3 Results

3.3.1 Systole and Diastole - Average and Standard Deviation

The summary of statistical data at the C2 level is given in Table IV below. Figures 3.3 and 3.4 show the flow waveforms for the volunteers and CM patients. Systolic phase of the cardiac cycle in volunteers was shorter than in the patients (32±7 % versus 40±6 % of the cardiac

cycle, respectively with Δ=23%). The systolic flow peak did not differ greatly between volunteers and patients (3.6±1.3 and 3.9±1.0 ml/s, respectively and Δ=6%). There was a larger difference for the diastolic peak between volunteers and patients (-1.5±0.4 and -2.1±0.4 ml/s, respectively with Δ=30%).

3.3.2 Normalization

The summary of statistical FFT-interpolated data at the C2 level is found in Table IV along with statistical data from original pcMRI data. As expected, the values are similar to the pcMRI data. The mean difference was generally at, or below 3%, except in CM Patients' diastole peak where Δ=9%. The normalization results are shown in Figures 3.5A -3.8A.

The FFT-interpolated systole duration within the cardiac cycle in volunteers was slightly shorter than in the patients (33±7 % versus 39±4 % of the cardiac cycle with Δ=18%). Although the systolic flow peaks did not differ greatly between volunteers and patients (3.7±1.3 and 3.9±0.9 ml/s, respectively and Δ=6%), the diastolic peak showed large differences (-1.6±0.4 and -2.3±0.5 ml/s, respectively with Δ=36%).

The cardiac-wise normalization enabled creation of representative flow waveforms for volunteers and the patients that have different heart rates. For each cardiac normalization time point, the standard deviation of flow magnitude was represented in error bars as shown in Figures 3.5A and 3.7A for volunteers and patients, respectively. For volunteers, the systole peak position and its magnitude varied the most (Figure 3.5A), where error bars reflected this variance clearly (Figure 3.5C). Interestingly, the smallest variation was at the post-systolic foot (systolic deceleration) and near the post-systolic peak of an averaged flow waveform. In diastole, the peak magnitude was not as different, but the location of the peak varied greatly with respect to

the averaged flow waveform peak. In patients, a significant change in flow magnitude was noticed at the systolic and diastolic peaks (Figures 3.7A and 3.7C). The smallest standard deviation was observed during the pre-systolic foot (systole acceleration) and near the transition between systole and diastole (near phase = 180º).

TABLE IV.

C2 FLOW WAVEFORM COMPARISON: VOLUNTEERS VS. CM PATIENTS.

Parameter	**Units**	**Flow Paramer Values (Mean ± Std. Dev.) Original Flow FFT Interp. Flow Orig. vs. FFT Δ(%)**		**Volunteers vs. Patients Mean Δ(%)**
		Volunteers	**CM Patients[a]**	
Number of Cases (n)	-	6	7	-
Heart Rate	bpm	58 ± 5	71 ± 6	20
Systole Peak	ml/s	**3.61 ± 1.29** **3.72 ± 1.33** 3%	**3.85 ± 0.95** **3.93 ± 0.86** 2%	**6** **6** -
Systole Duration	%	**31.8 ± 7.0** **32.5 ± 6.6** 2%	**40.2 ± 5.6** **39.1 ± 4.4** 3%	**23** **18** -
Diastole Peak	ml/s	**1.52 ± 0.37** **1.57 ± 0.39** 3%	**2.05 ± 0.43** **2.25 ± 0.50** 9%	**30** **36** -
Diastole Duration	%	**68.2 ± 7.0** **67.5 ± 6.6** 1%	**59.8 ± 5.6** **60.9 ± 4.4** 2%	**13** **10** -

[a] CM patient cases before the decompression surgery.

Additional normalization of flows via their respective systolic peaks eliminated the high variance due to magnitude, as mentioned above. In volunteers (as shown in Figures 3.5B, 3.5D and 3.6B), the normalization did not completely remove variation due to magnitudes at the representative peaks, which is caused by a variation in the peak's location. In patient cases (Figures 3.7B, 3.7D and 3.8B), the systolic acceleration phase and systolic peak had small standard deviation. Thus, the magnitude normalization showed consistency in systole shape within the cycle.

An interesting feature can be observed in Figures 3.6C and 3.8C. The post-systolic peak or hump was larger in volunteers compared to patients (Figures 3.1-3.4). The averaged representations of volunteer and patient flow waveforms also demonstrate this feature (Figures 3.5-3.8). The Figures 3.6C and 3.8C show that this peak indicated secondary positive CSF displacement more often in volunteers than in patients. Also, the averaged flow waveform showed a peak after systole with positive CSF displacement in the volunteer data but not in patients.

3.3.3 FFT Decomposition - Shape Analysis

In the previous section, the results showed that the healthy flow waveforms were found to be different in shape from those of the patients. In order to quantify these flow shape differences, FFT coefficients of the flow waveforms were examined. The results show that flow waveforms from volunteers have a dominant magnitude at higher harmonics (N_{fft} = 2 and 3) for real components than in CM patient data (N_{fft} = 1 and 2) as shown in Figures 3.9 and 3.10. The complex parts of FFT coefficients were quite similar for both volunteers and patients.

3.3.4 Peak to Peak Difference

Both SP2PdQ and DP2PdQ indicate clear differences between volunteers and CM patients as shown in Table V. On average, the SP2PdQ and DP2PdQ showed Δ at 55% and 36%, respectively.

TABLE V.

SYSTOLE AND DIASTOLE PEAK TO PEAK FLOW DIFFERENCE BETWEEN C2 AND C8.

Parameter	**Units**	**Volunteers (Mean ± Std. Dev.)**	**CM Patients[a] (Mean ± Std. Dev.)**	**Δ (%)**
Number of Cases (n)	-	6	7	-
SP2PdQ[b]	ml/s	1.96 ± 1.55	1.11 ± 1.03	55
DP2PdQ[b]	ml/s	0.62 ± 0.51	0.43 ± 0.24	36

[a] Only CM patient cases before the surgery.

[b] Adjustment was performed to flow waveforms that were not measured at C8 level (C7, T1 and T2).

3.4 Discussion and Conclusions

3.4.1 Flow Features

The CSF flow waveforms were found to be different between patients and healthy volunteers. These differences are summarized in various plots of averaged flow waveforms and FFT decomposition as shown in Figures 3.12 and 3.13. The representative flow features and flow waveform shapes for both patients and volunteers indicate differences, which could serve as quantitative measures to categorize the flow waveforms into problematic or healthy.

Furthermore, a similar study should be conducted to assess the post-surgical flow waveforms versus the pre-surgical and healthy. It would be interesting to determine if the flow waveform characteristics of CM patients with positive post-surgical symptom outcome would approach the characteristics of healthy volunteers.

Duration of systole was shown to be shorter for volunteers in this study, which agrees with the work by Bhadelia et al. [45], and Hofmann et al. [28], as shown in Table VI. Hofmann et al. [28] also computed representative flow waveforms for volunteers and patients. The flow waveforms were computed from anterior and posterior portions of SAS at the C2 level. These waveforms were reproduced and integrated to obtain total CSF displacement. This allowed for side by side comparison of flow waveforms between this work and that by Hofmann et al. as shown in Figure 3.13. The results show that patient flow waveform from this study is similar to that of Hofmann et al. while the volunteer data has some differences. In the results by Hofmann et al., systolic duration is longer with post-systolic peak barely within the positive flow displacement regime.

TABLE VI.

SYSTOLE DURATION IN LITERATURE COMPARED IN THIS WORK.

Study	**Volunteers Systole Duration (%)**	**CM Patients Systole Duration (%)**	**Δ (%)**
Bhadelia et al. [45][a]	38 (n=23)	42 (n=15)	10
Hofmann et al. [28][b]	34 (n=18)	36 (n=18)	6
Kalata	33 (n=6)	39 (n=7)	18

[a] Based on velocity waveforms at multiple locations.

[b] Based on addition of flow waveforms in anterior and posterior portions of SAS at C2 level.

3.4.2 FFT Decomposition

The post-systolic peak was noticed in all volunteers (Figure 3.1). In some patient cases, during the systole-diastole transition, (Figure 3.2) a less distinct peak was present, and in some patient cases, partial flattening was observed. While these differences are observed with the "naked eye," the differences should be quantifiable as well. Hence, FFT decomposition of flow waveforms was performed and various graphical representations are shown in Figures 3.9, 3.10, 3.12 and 3.13.

The real components from FFT coefficients depict the most pronounced differences (Figures 3.12B and 3.13C). The representative curves indicate that the negative magnitude region in patients is at lower frequencies (N_{fft}=1,2 and 3) as opposed to volunteers where the negative magnitude region is at higher frequencies (N_{fft}=2,3,4 and 5). Thus, volunteer C2 flows with distinct positive post-systolic peak correlated with the first positive harmonic and elongated negative frequency range. This leads to the conclusion that patient C2 flow waveforms lack of more dominant secondary peak which correlates with elongated systole duration.

The imaginary components from FFT coefficients were similar for both volunteers and the patients. The most distinct feature that differentiates between representative curves of patients and volunteers is shown in Figures 3.12B and 3.13D. The volunteers' curve had wider range in the negative region (N_{fft}=1,2 for volunteers, N_{fft}=1 for patients). In this particular range, the highest magnitude of imaginary component (-15 at N_{fft}=1) was present for both volunteers and patients.

3.4.3 Indication of SAS Compliance

The noticeable change in both systolic and diastolic peaks between C2 and various lower locations indicate compliance in the spinal canal, which acts as a damping mechanism for the blood volume change in the head. The larger volume changes between two locations in healthy volunteers (Table V) indicate flexibility in the cervical spinal region. This indicates that CM patients have less compliance given that volumetric displacement from the head is similar to that in volunteers. In Kalata's work [1], a healthy volunteer case had pcMRI scans performed at multiple cross-sections throughout the spine (Figure 3.14). These were done 18 cm apart. There was significant compliance observed at the upper spine portion. In contrast, at the lower back region, the compliance was not noticeable.

Since velocity scans are often performed only at the cervical and upper thoracic levels, there is a lack of flow measurements in the lumbar region. The assessment of the compliance in the lower back may be useful in determining the role of CM on SAS rigidity in the cervical region. Currently, new MRI protocols are being developed to assess compliance relating to pulse wave velocity (see Chapter 5) or cross-sectional area changes. When refined, these techniques may be useful in the assessment or treatment of CM and SM.

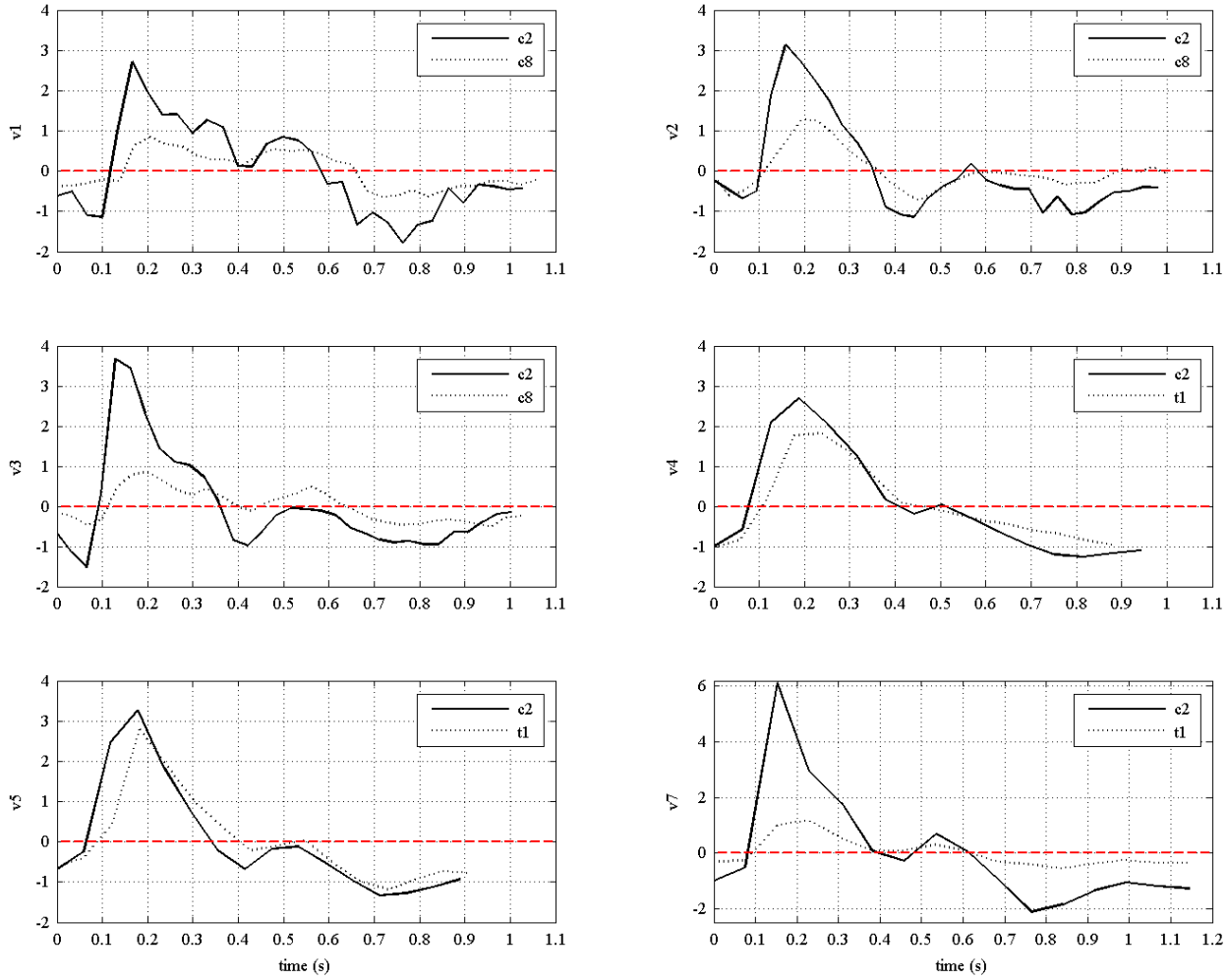

Figure 3.1. Volunteer flow data (n=6) at multiple vertebra positions.

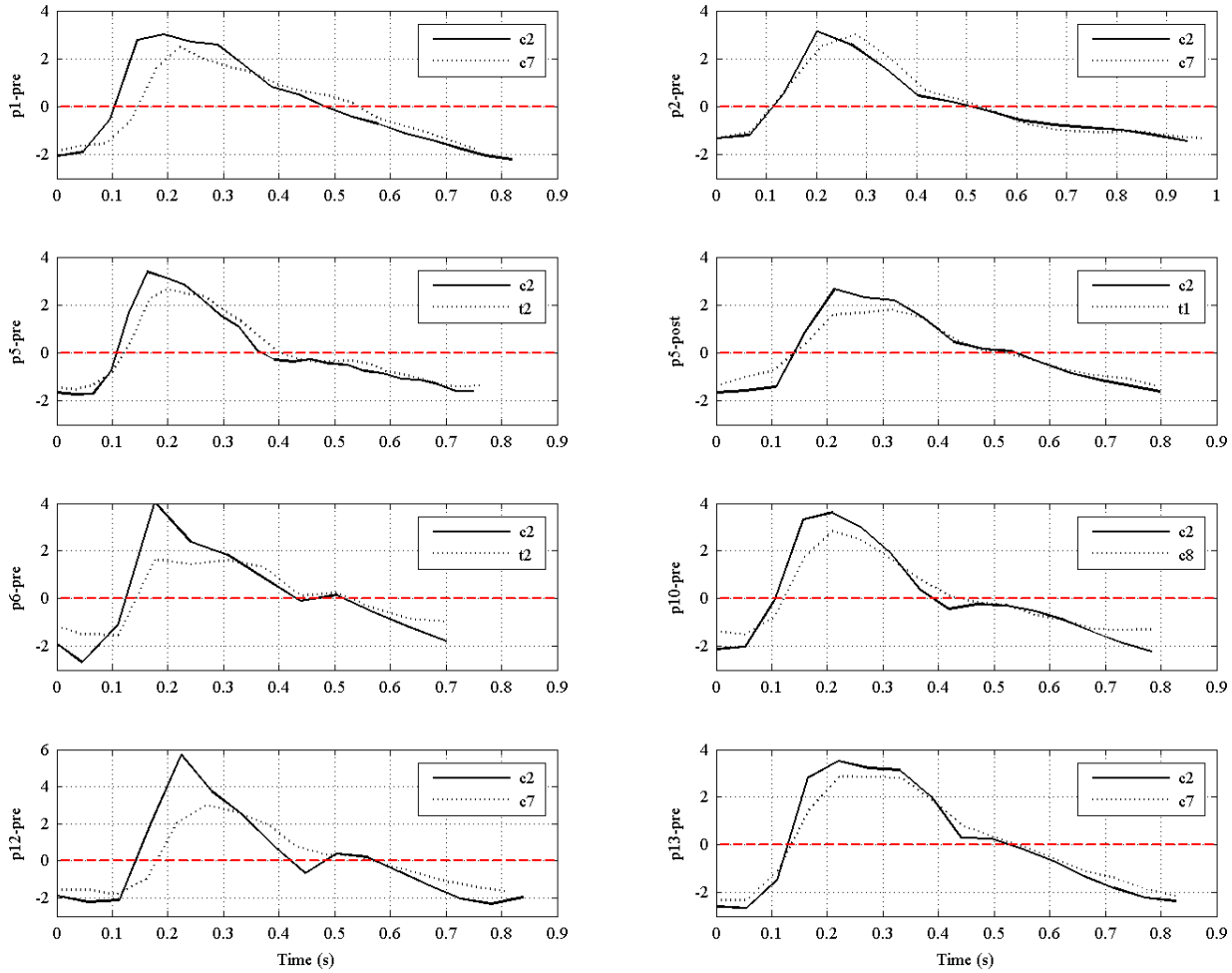

Figure 3.2. Patient flow data (n=8) at multiple vertebra positions. Pre- (n=7) and post-surgery (n=1) cases included.

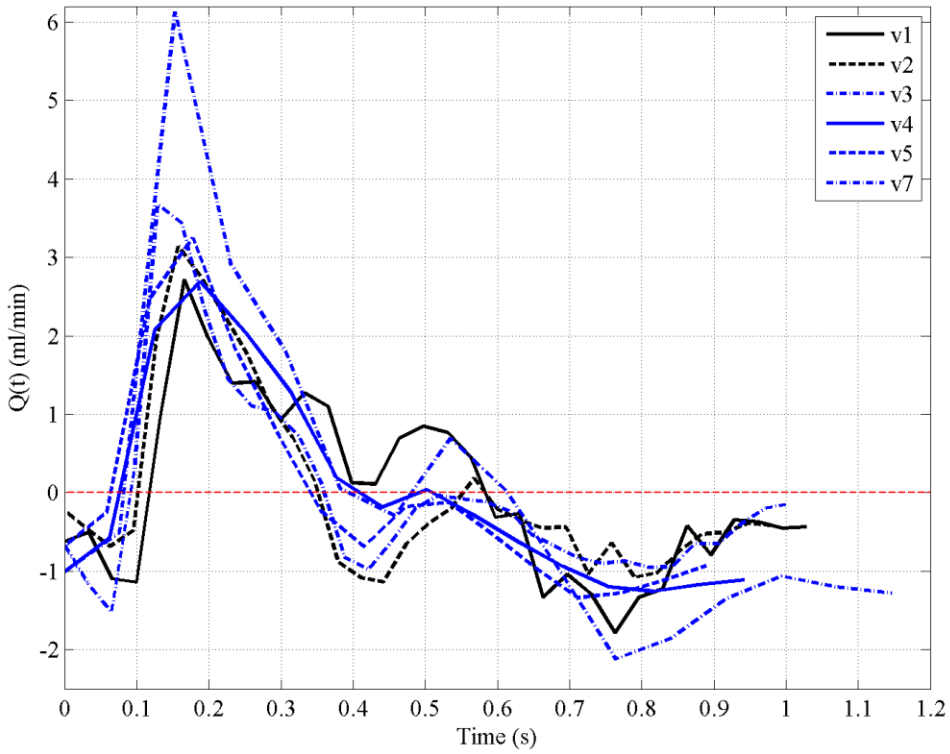

Figure 3.3. Volunteer flow data at C2.

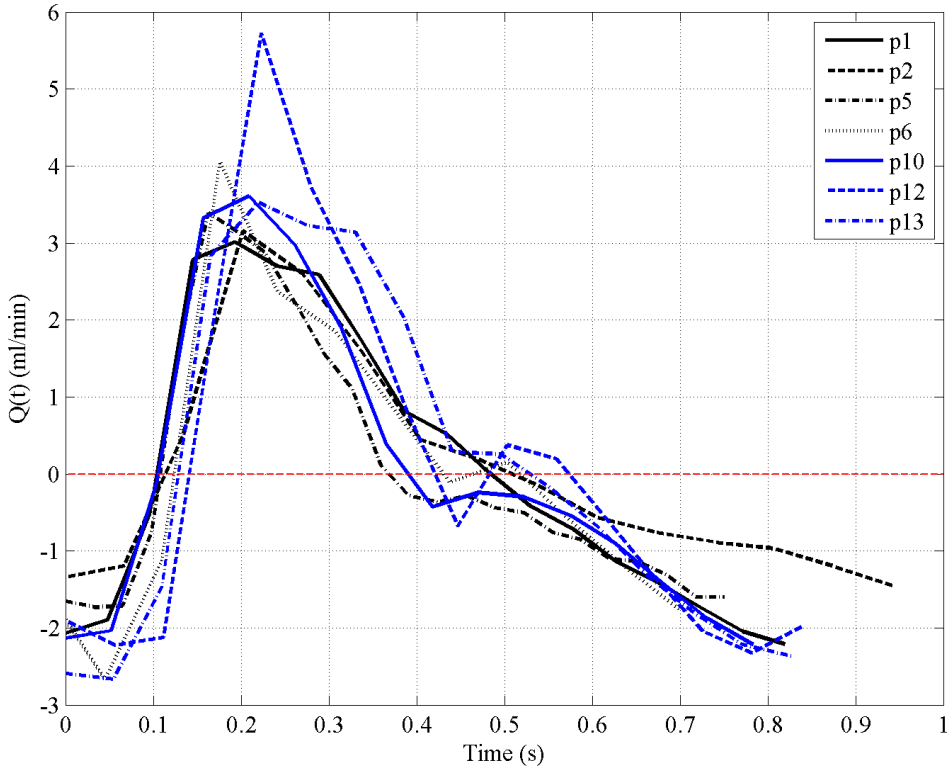

Figure 3.4. Pre-surgical patient flow data at C2.

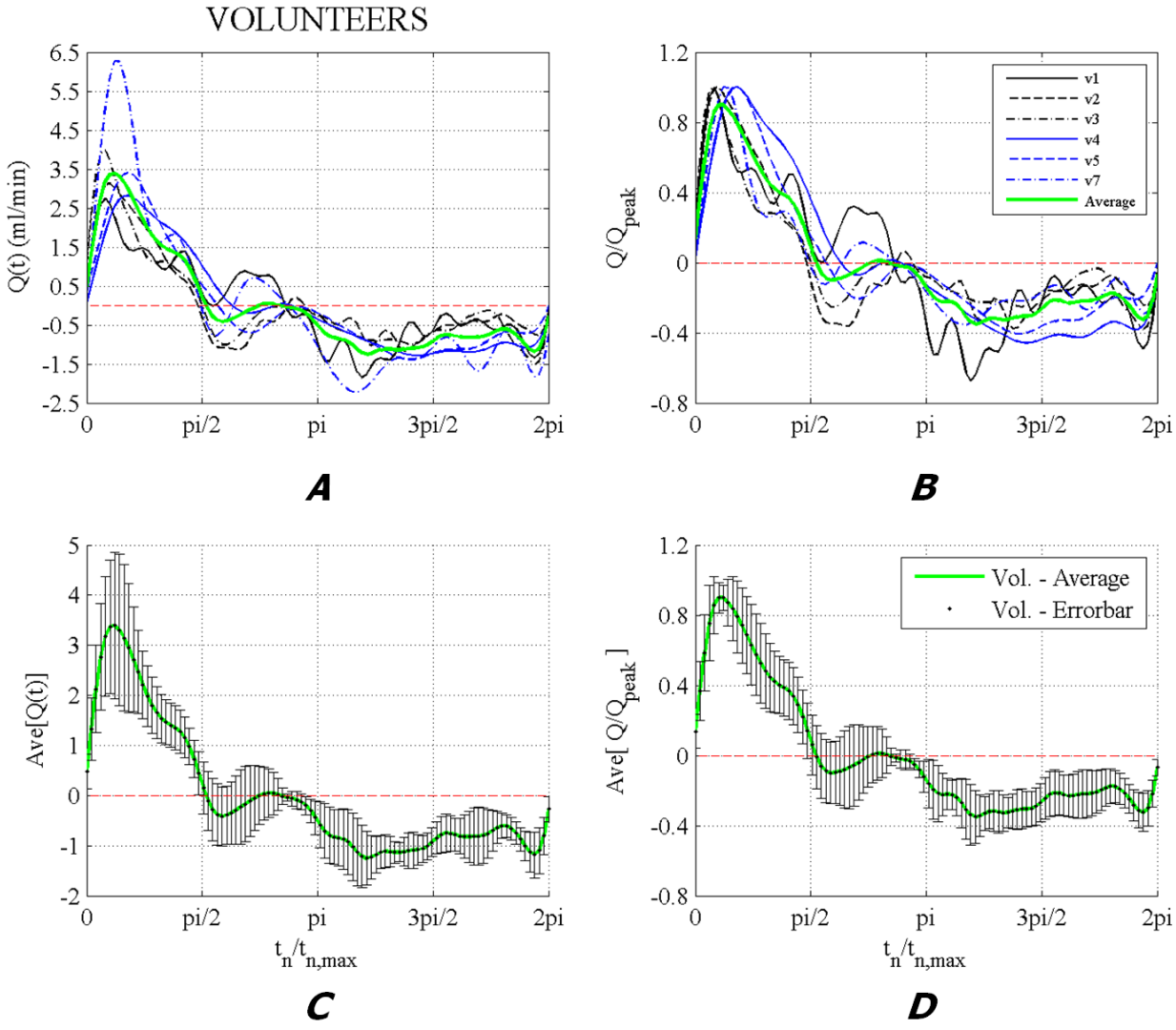

Figure 3.5. Normalization of volunteer C2 flow data: **A.** Flow data with cardiac cycle normalization only, **B.** Flow data with normalization with respect of maximum flow, **C.** Averaged input data with standard deviation errors bars, and **D.** Averaged normalized data with standard deviation errors bars.

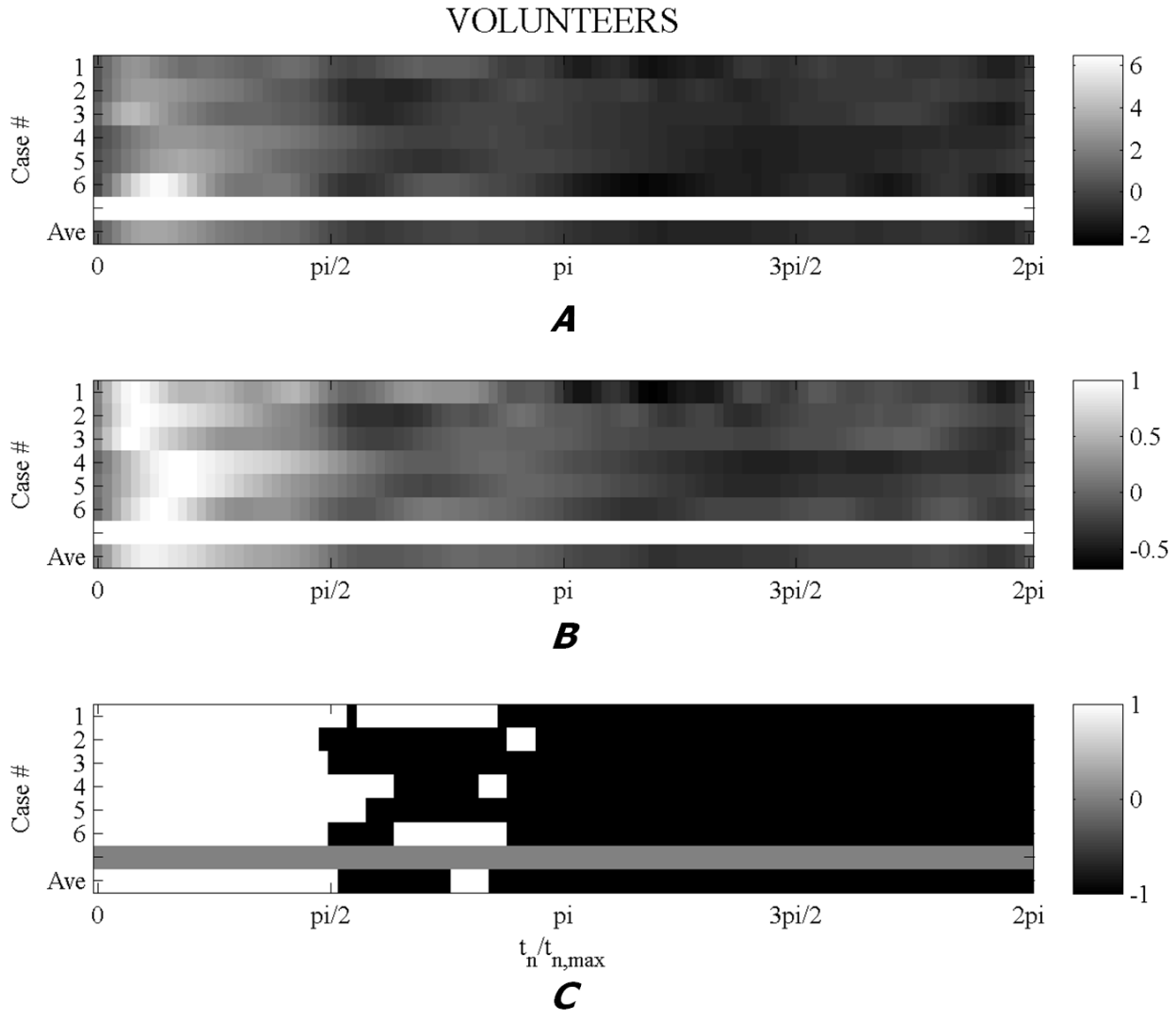

Figure 3.6. Image intensity plots of volunteer C2 flow data: **A.** Flow data with cardiac cycle normalization only, **B.** Flow data with normalization with respect of maximum flow, and **C.** Distinction of positive (systole) and negative (diastole) flow displacement.

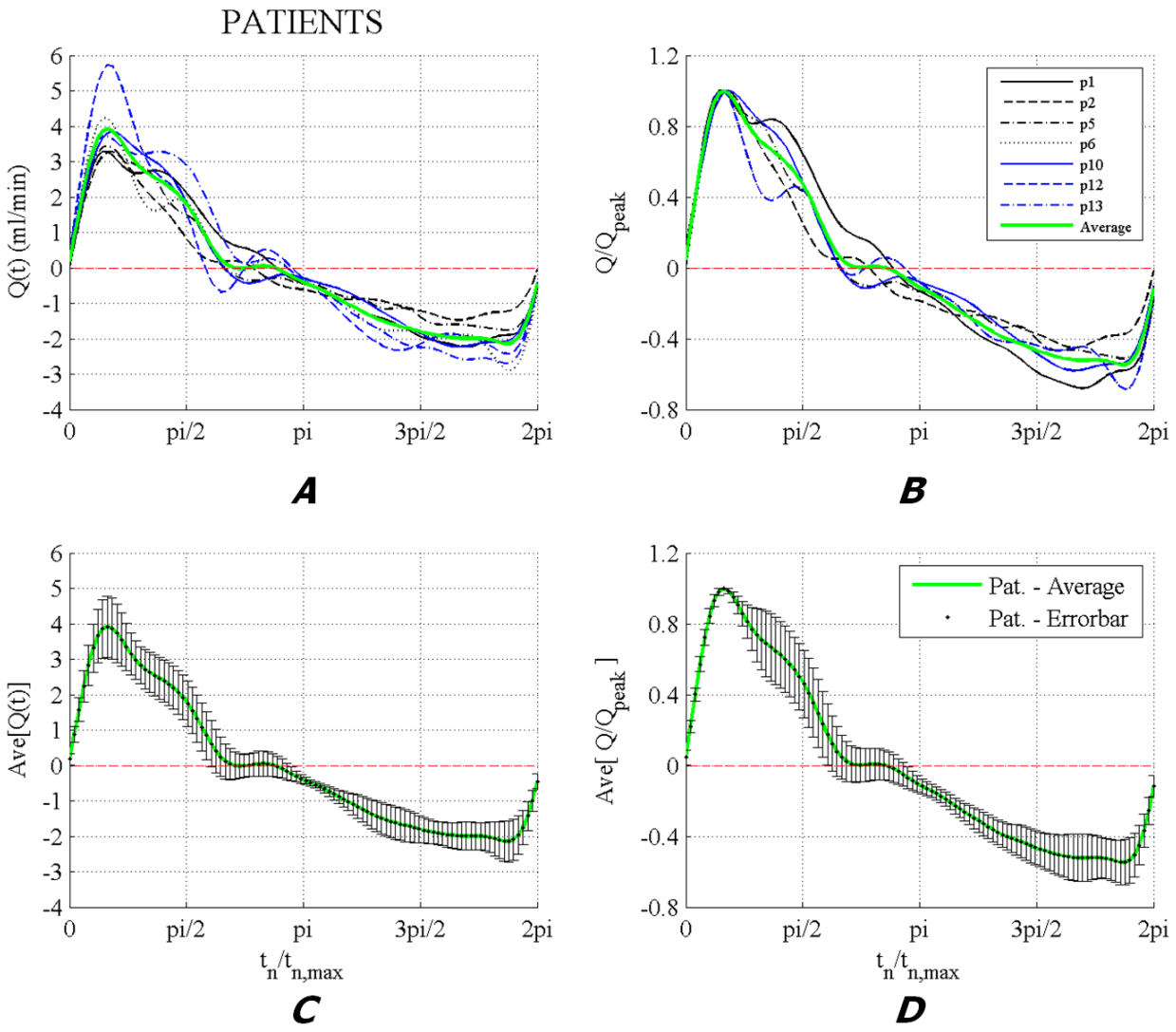

Figure 3.7. Normalization of pre-surgical patient C2 flow data: **A.** Flow data with cardiac cycle normalization only, **B.** Flow data with normalization with respect of maximum flow, **C.** Averaged input data with standard deviation errors bars, and **D.** Averaged normalized data with standard deviation errors bars.

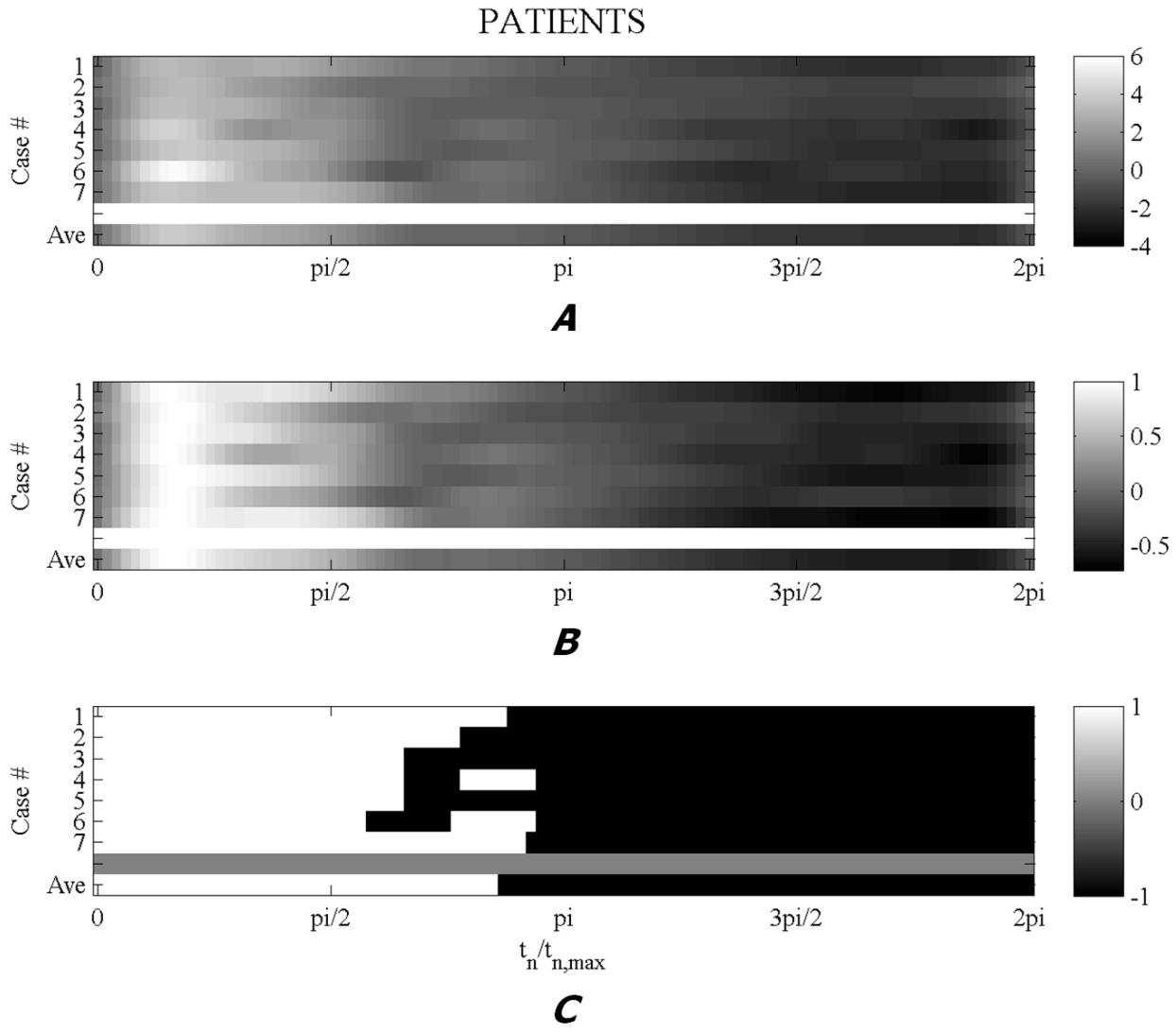

Figure 3.8. Image intensity plots of pre-surgical patient C2 flow data: **A.** Flow data with cardiac cycle normalization only, **B.** Flow data with normalization with respect of maximum flow, and **C.** Distinction of positive (systole) and negative (diastole) flow displacement.

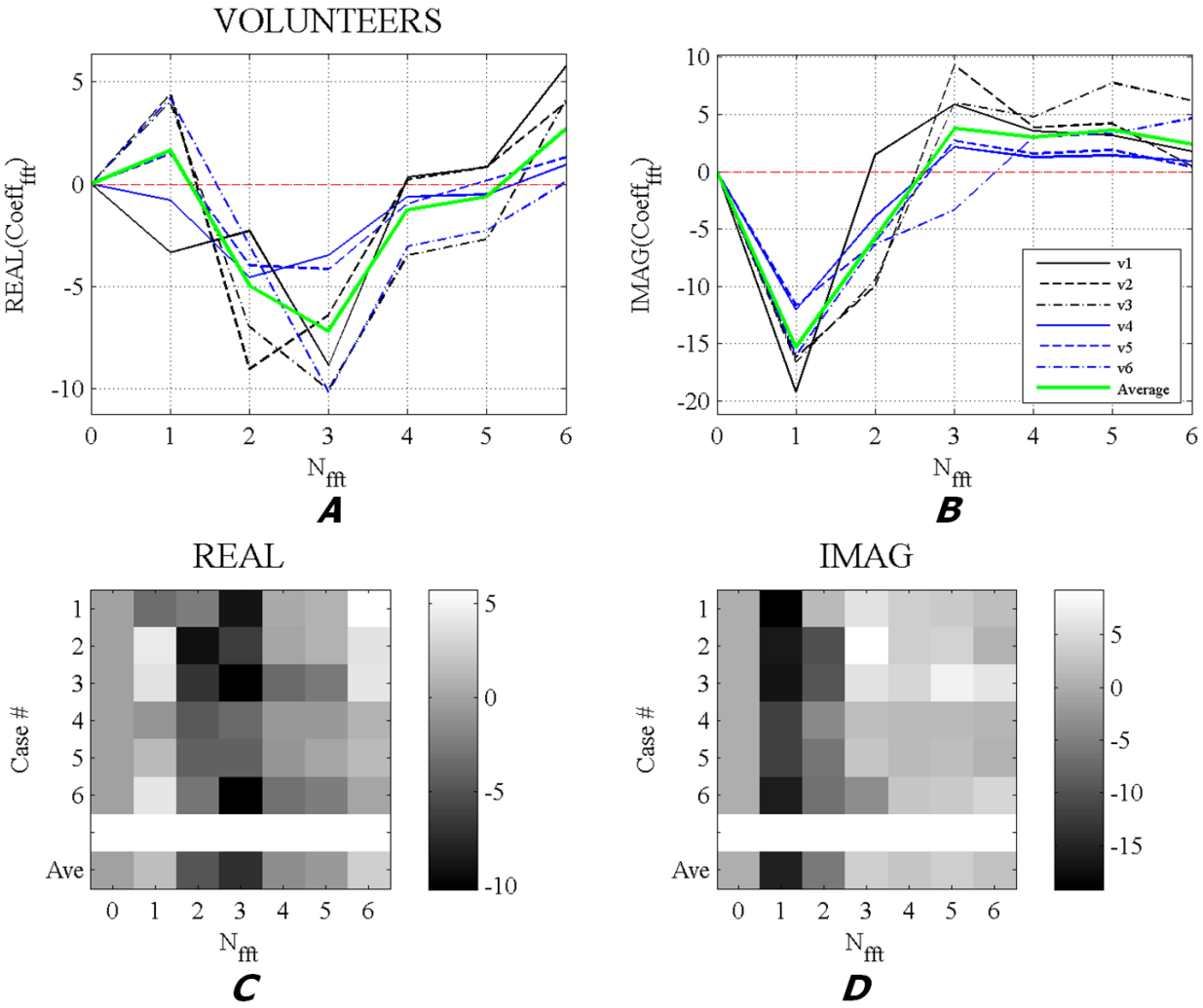

Figure 3.9. Harmonic breakdown of volunteer C2 flow data: **A.** Plots of real components of FFT coefficients, **B.** Plot of imaginary components of FFT coefficients, **C.** Image intensity representation of real components of FFT coefficients, and **D.** Image intensity representation of imaginary components of FFT coefficients

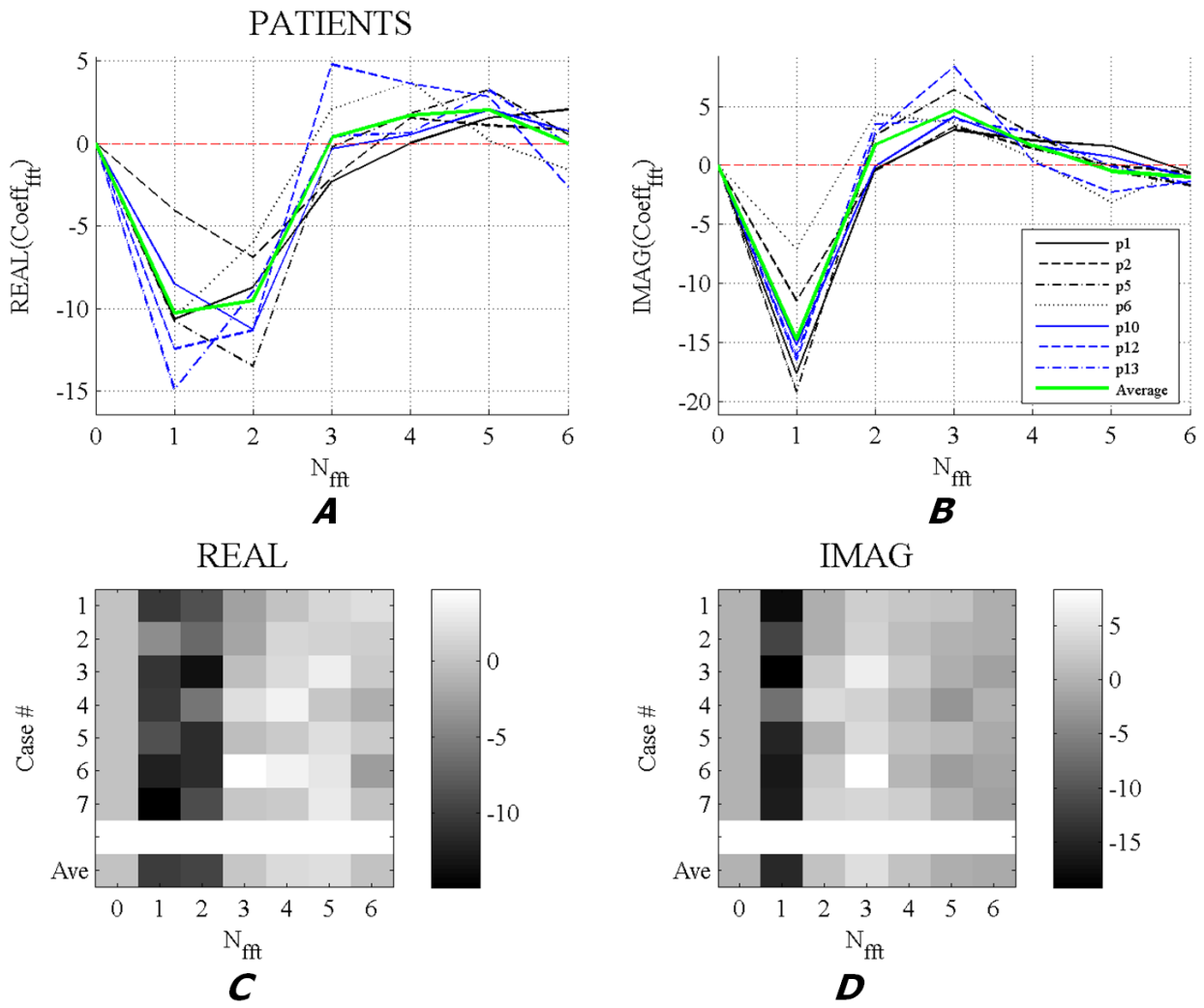

Figure 3.10. Harmonic breakdown of pre-surgical patient C2 flow data. **A.** Plots of real components of FFT coefficients, **B.** Plot of imaginary components of FFT coefficients, **C.** Image intensity representation of real components of FFT coefficients, and **D.** Image intensity representation of imaginary components of FFT coefficients

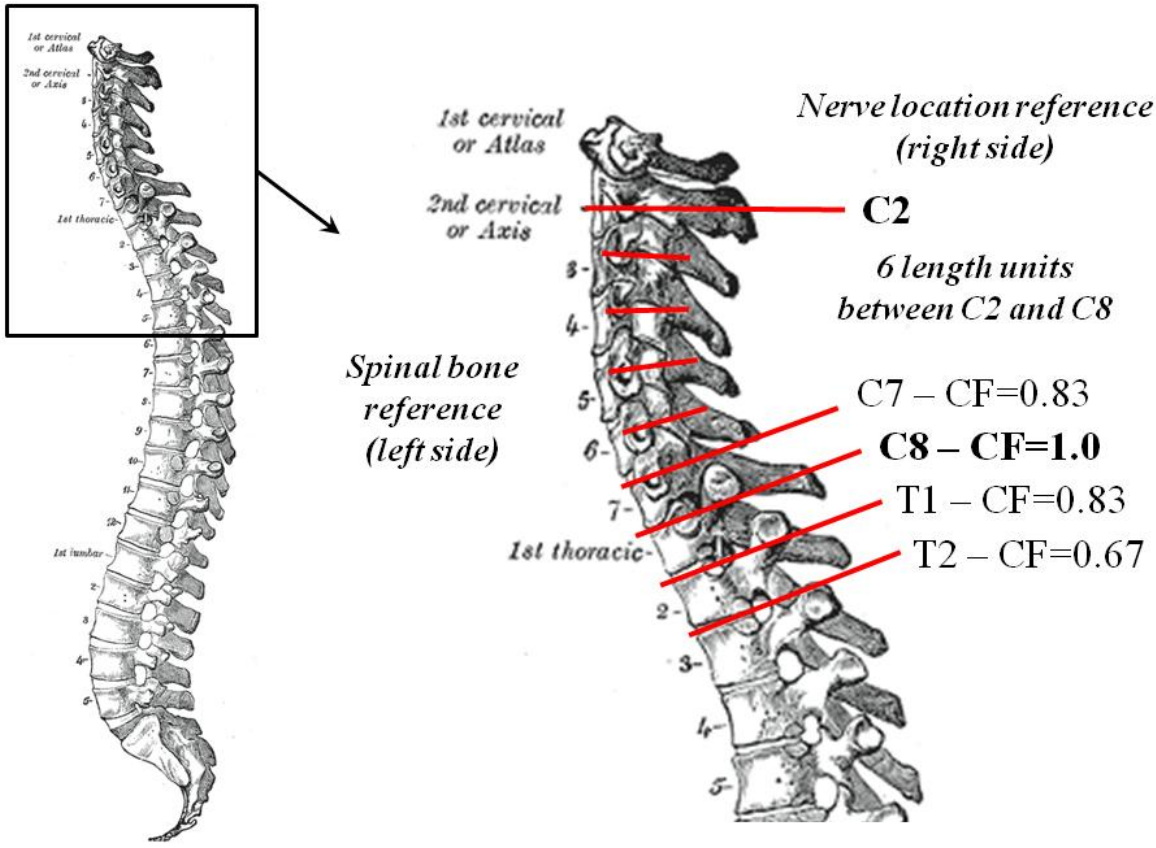

Figure 3.11. Location reference for flow waveforms. The reference for correction factor included. Spine illustrations were obtained from Gray's Anatomy by Henry Gray [46].

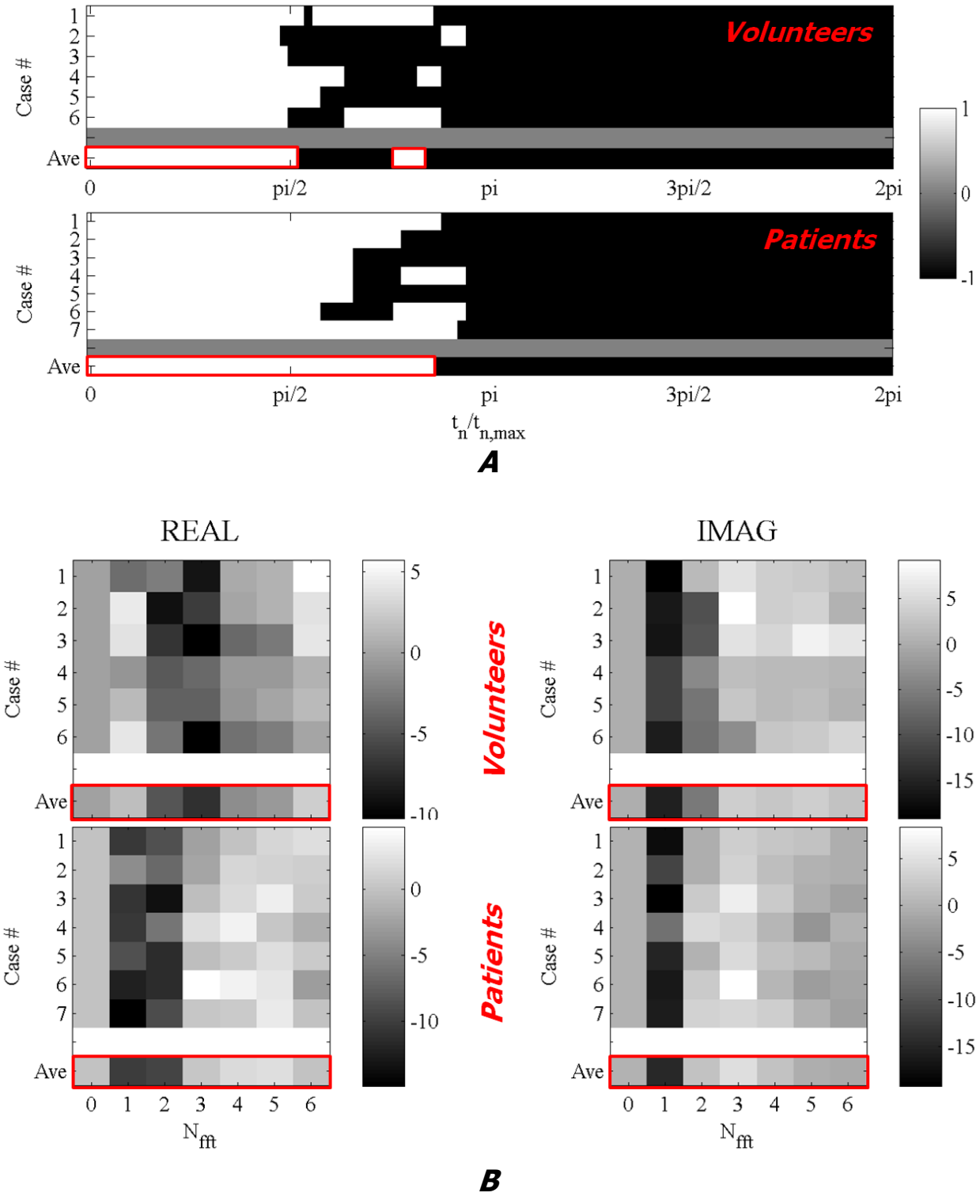

Figure 3.12. Volunteer versus pre-surgical patient comparison summary of normalized flow data and harmonic breakdown of C2 flow data: **A.** Distinction of positive (systole) and negative (diastole) flow displacement, and **B.** Image intensity representation of both real and imaginary components of FFT coefficients.

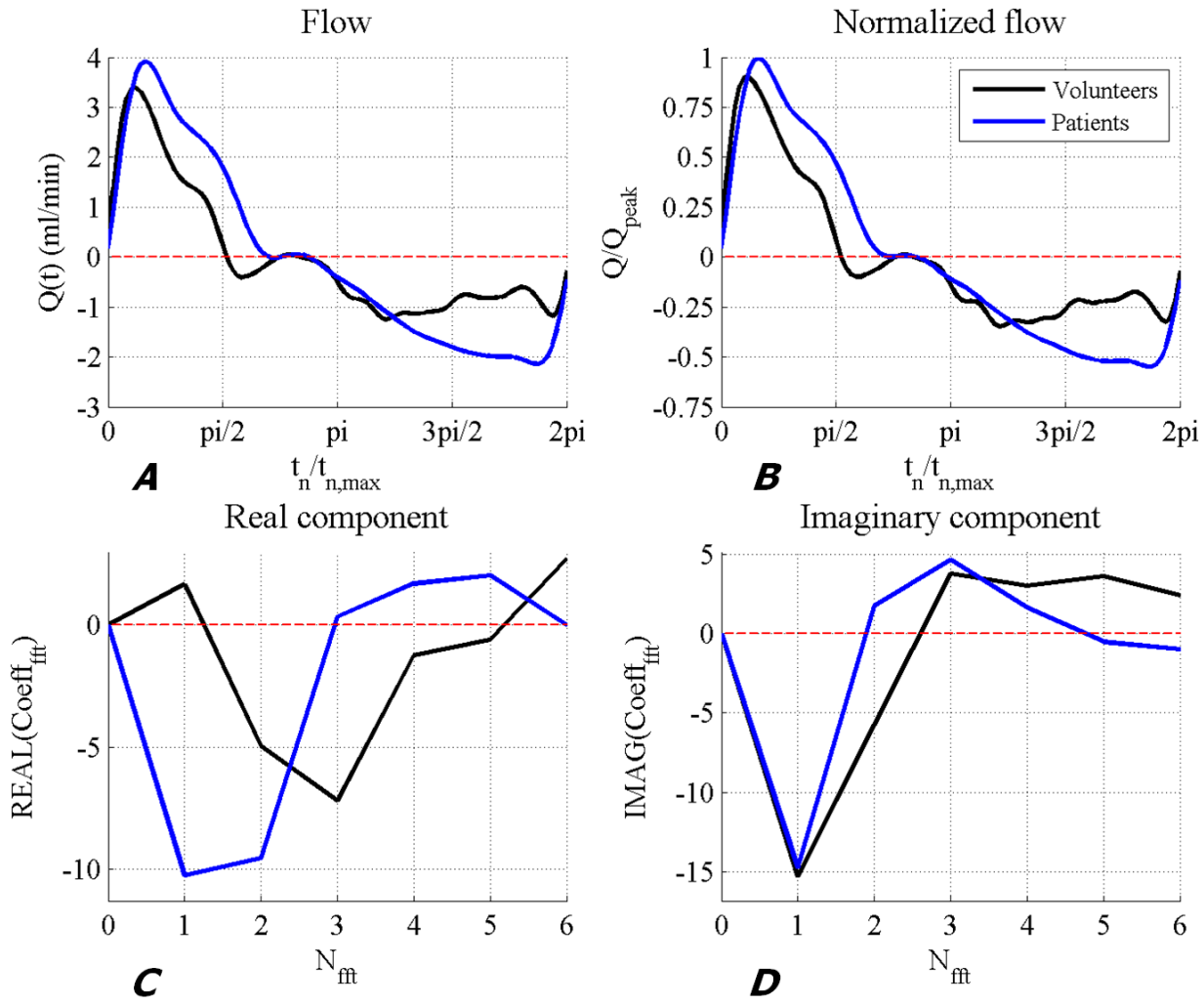

Figure 3.13. Volunteer versus pre-surgical patient comparison summary of normalized flow data and harmonic breakdown of C2 flow data: **A.** Averaged flows, **B.** Averaged and normalized flows, **C.** Averaged real components of FFT coefficients, and **D.** Averaged imaginary components of FFT coefficients.

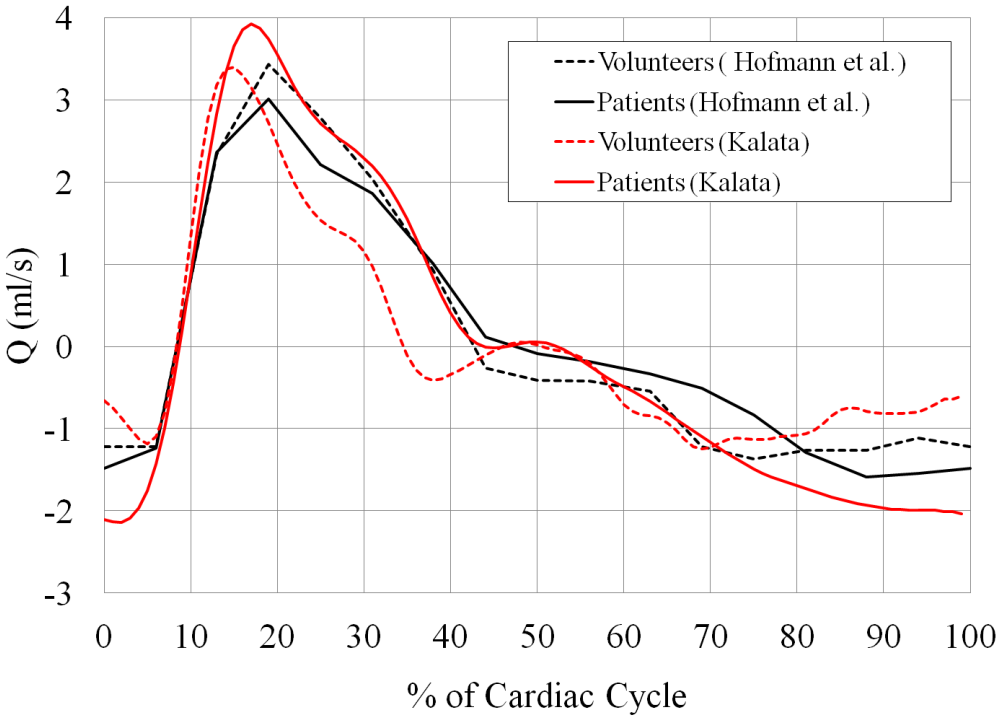

Figure 3.14. Representative flow waveforms for volunteers and patients computed from Hofmann et al [28] compared with current data.

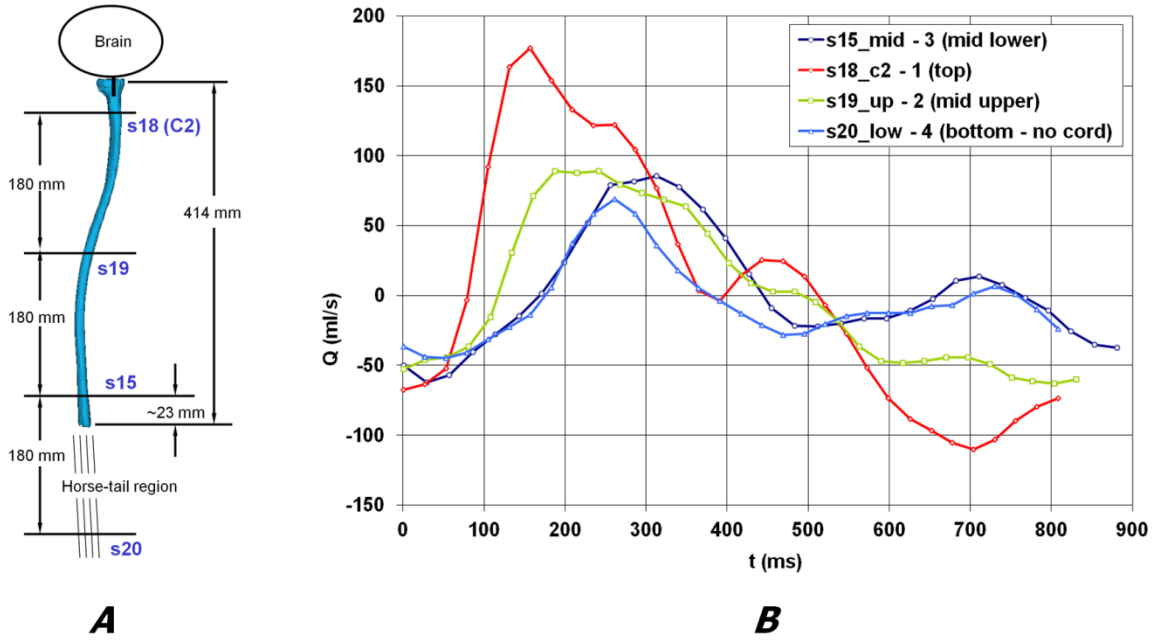

Figure 3.15. Volunteer flow waveforms at multiple axial locations from Kalata (reference). **A.** Location reference, **B.** Flow waveforms

4. CM IN-VITRO MODEL

4.1 Introduction

The experimental approach to investigate flow in round conduits has been utilized by fluid dynamics pioneers like Osborne Reynolds and Jean Louis Marie Poiseuille since the mid nineteenth century. Experiments are progressively becoming more complex as the modeling assumptions are eliminated by inclusion of more complex features. Most of the biological flow modeling was focused on reproduction of blood flow within atherosclerotic vessels [32-35]. Physical models of CSF flow are not common. CSF models of the SAS were investigated by Martin et al. where they focused on reproducing a pressure environment in SAS and inside a syrinx [47, 48].

In the past two decades, CFD became an increasingly popular tool to investigate pathological blood flows in atherosclerotic vessels [33-35]. Loth et al. [36] introduced a 2-D CFD method for annular structures which was based on physiological SAS cross-sections. Recent work by Gupta et al. [49] investigated CSF flow below and around the bottom part of the cerebellum. Gupta et al. used a CFD model that included detailed geometry of a healthy subject. Gupta et al. concluded that CFD based on a subject–specific geometry and flow can be used to optimize drug delivery and spinal-cerebral pathologies such as SM.

In this chapter, flow measurements inside a physical model are presented. Also, CFD was used to simulate CSF flow and compute transient resistance in a CM blockage. The sub-cranial SAS geometries investigated in Chapter 2 were simplified into continuous annular geometries with variant cross-sectional areas. In this chapter, the CM SAS geometry is more

complex. The blockage geometry includes tonsil irregularities where flow passages in FM regions are very narrow.

4.2 Patient Data

One CM/SM patient (designated as P1) was scanned before the craniectomy or decompression surgery. MRI geometries of the bottom half of the brain, sub-cranial SAS, and upper spinal cord were obtained. The 3-D model of the sub-cranial SAS was reconstructed using MIMICS in a same manner as described in Section 2.2.2 and in more detail by Kalata [1]. The two zones of SAS were reconstructed for this patient case, as shown in Figure 4.1. The first zone was the sub-cranial SAS (Figure 4.1A-C) and the second zone was the SAS with syrinx (Figure 4.1D-E). The geometry of the blockage was complicated in shape, particularly in the region where the brain tonsils descended and created narrow passages for CSF flow. The vertebral arteries were included that partially run through the anterior part of the upper SAS.

During the same scan session, cardiac gated phase encoded velocity was measured at four different axial positions of the upper back and neck (C2, C4, C7, and T3). Using MRView, the SAS flow waveforms were obtained for these pcMRI data sets. The resulting CSF flow waveforms are shown in Figure 4.2C with position references (Figures 4.2A-B). Levels C7 and T3 included flow of the fluid inside the syrinx (Figure 4.2B-C).

4.3 3-D Model

The physical SAS model was built in a similar fashion of previously built models [39, 50]. The 3-D model (Figure 4.3A) from patient's MR anatomy images was used to construct a rigid 3-D Sylgard model of the SAS. The virtual model was processed with a smoothing

algorithm as described in Section 2.2.2 and Kalata [1]. This algorithm imports Stratasys Layer (SSL) data that was exported by MIMICS. After smoothing, 3-D points for surface were exported.

Extensions were virtually added to ensure the hydrodynamic reproducibility to the in-vivo condition as shown in Figure 3 as described in sections 2.2.2 and by Kalata [45] and Yedavalli et al. [39]. Using MATLAB, extensions for the model were created on both ends of the flow conduit. All 3-D features were created in sliced format (SSL format) which was easily read by rapid prototyping software (Stratasys Insight). The thickness of each build layer was 0.254 mm (0.01 in). At the bottom end, 2.5 cm of annular shape was extended and then an attachment was created for tubing (Figure 4.3B). The top end had more complex geometry with three different flow passages (Figures 4.3A and 4.4). The anterior SAS passage had also contours of arteries. The top end of the SAS geometry was extended for 2 cm by gradually scaling up the top cross-section. Additionally, a top reservoir extension connecting to the tubing was created (Figure 4.3B).

The spatial negative of the flow models (Figures 4.3B and 4.5A) were built with a rapid prototyping machine (Stratasys FDM-3000). Initially a model was built with an acrylonitrile butadiene styrene (ABS) material which is easier to build with. A WaterWorks material (StrataSys, Eden Praire, MN) was used to create a second negative geometry. The built layers were 0.254 mm (0.01 inch) as prescribed in a custom MATLAB program. After the build, rapid prototyping artifacts and excess support material were removed manually. Additional sharp edges and layer groves on the model were sanded off manually with sanding paper and a Dremel tool.

The SAS geometry with a full bottom and partial top extensions was cast with Sylgard 184 (Dow Corning, Midland, MI), as shown in Figures 4.4C and 4.5B. After curing, the negative was dissolved with a mixture of water and a special WaterWorks solvent using a temperature controlled ultrasonic tank (Figure 4.5C-D). The remainder of top extension was cast separately with a plastic negative (Figure 4.5E). The negative plastic extension was removed from partially cured Sylgard. The cured model was then attached to a partially cured extension, such that the final curing process would include adhesion of the uncured part to the cured part. After a complete curing process, the optically clear model (shown Figures 4.4D and 4.5F) was successfully tested for leaks. Finally, the flow model was assembled and connected to the flow pump as shown in Figure 4.6. The flow in the Sylgard model was driven by a pulsatile pump constructed from a computer-controlled linear motor (TT Micro Model #TB1106, Copley Controls Corp., Canton, MA) as shown in Figure 4.7. This pulsatile pump had the capability to accurately reproduce CSF flow waveforms (same pump was used by Martin et al. in SM studies [47, 48]). The pulsatile pump consisted of a tubular linear servo motor, which drove a high grade glass syringe in a pulsatile manner according to a low voltage signal delivered by a laptop computer. The motor was equipped with a linear encoder (RG24 Digital Read, Model #RGH24X30A00A, Renishaw, Hoffman Estates, IL) to precisely track the position of the syringe down to 1 μm. Ten-poise spindle oil was used to lubricate the syringe while the motor pulsed.

4.4 MRI Velocity

4.4.1 MRI Measurement Methods

The MRI images for the geometry and the transient velocity measurements inside the model were aquired on the same MRI scanner as the patient (P1 which was included in Chapter 3). The pulsatile pump was connected to the CM flow mode with long nylon tubing. The model was placed at the same location as a subjects neck would be located (see Figure 4.8A). All parts that were connected to the model were non-metallic since the measurements were performed inside the MRI machine that has a powerful magnetic coil as one of its main components (Figure 4.8B). The pulsatile pump was placed by the door, as far away as possible, from the MRI scanner. The control hardware (computer, oscilloscope, input-output board, and linear motor power supply) was placed in the adjacent room to MRI scanner room.

At the location representing the in-vivo C2 level, measurements of all velocity components were obtained. Also, axial velocity was obtained at levels 25 mm above (blockage or CM region) and 25 mm below the representative C2 level (approximately C3 level), as shown in Figure 4.9A. The velocity data was processed with MRView. For the C2 level, velocity for all three components was obtained (Figure 4.9A and B). At the blockage level (CM), three separate flow conduits were evaluated (Figure 4.9A and C).

During MRI measurements, along with velocity information, the geometry of the model was obtained in sagittal and axial planes.

4.4.2 MRI Flow Results

Based on unsteady axial velocity at 3 locations (C3, C2, CM), as shown in Figure 4.10, the resulting flow waveforms were similar in shape and magnitude (Figure 4.11A). At the

systolic peak CM flow was noticeably higher (-3.5 ml/s) than C2 or C3 flows (-3.0 and 2.5 ml/s) respectively (Figure 4.10). The resulting model flow was similar to patient flow in magnitude as shown in Figures 4.11 and 4.12. Although the magnitude was similar, the acceleration phases between systole and diastole were not well matched (Figure 4.11A). Figure 4.11B shows axial velocity at systolic peak where Reynolds number in model was 116 as compared to patient's Reynolds number of 127.

At the C2 level, spatially averaged values of all three velocity components were obtained (see Figure 4.13). As it can be expected, the axial component (V_Z or W) was the dominant velocity component. Throughout the cardiac cycle, the V_Y (or V) generally followed the 10-20% of axial velocity. The V_X (or U) showed almost zero spatially averaged velocity. At the CM level, a flow split based on three conduits was computed based on flow waveforms as shown in Figure 4.14. The majority of the flow went through the anterior part of the CM level (78% of total flow – temporal average).

4.5 CFD

4.5.1 Methods for 3-D CFD

The geometry for the CFD model was processed from anatomical MRI images obtained during experiments with the CM model. The geometry was processed in MIMICS in a similar fashion as the patient's geometry. The 3-D SAS model surface in STL format was imported into MeshLab (GPL, 1.3.0b, Rome, Italy) for surface smoothing. The Laplacian smoothing algorithm was used to smooth out unnecessary edges and artifacts (Figure 4.15).

The smooth version 3-D SAS model surface in STL format was imported into the ANSYS Gambit (Version 2.4.6) meshing software. The triangulated surface data was imported

without edges, therefore, the continuous surface was created within Gambit. At each end of the geometry "real" surfaces were created to clip the ends in order to create edges that would define inlet and out boundaries. The planes that were used for clipping were divided by SAS edges to define the contours for the inlet and outlet boundaries. All excess geometries outside the domain of interest were deleted. The resulting surfaces were forming a closed group of surfaces representing SAS geometry. The newly created boundary surfaces were "stitched" and processed to create a "virtual" volume of SAS.

The mesh was created with a tetrahedral size of 0.25 mm at the walls. The meshing included sizing functions at the SAS walls with a growth rate of 1.2 with maximum cell size of 2 mm. After the SAS domain was meshed, mesh extensions were added at the inlet and outlet boundaries. The mixed, unstructured mesh consisted of 3,654,042 mixed elements (mainly tetrahedral cells) as seen in Figure 4.16. Within ANSYS FLUENT 12.1, the mesh was converted to a polyhedral cell mesh with 912,918 elements (Figure 4.17). The simulations were conducted using finite volume solver ANSYS FLUENT 12.1.

IBC was based on unsteady mass flow rate (Figure 4.17), similar to the CFD method in Chapter 2. A user defined function was used to incorporate FFT coefficients in order to reproduce the flow waveform shapes. An outlet was set as CPBC at 0 Pa.

The flow was simulated with a transient pressure-based, isothermal and laminar solver. The spatial discretization was handled with a "least square cell based" gradient. The pressure-coupling scheme was SIMPLE with PRESTO! discretization. The momentum was using "second order upwind" spatial discretization. The transient scheme employed first order implicit formulation.

With the same geometry, three parametric cases were simulated to assess variations between cases with different flow waveforms and liquid properties. The following cases with flow waveforms and fluid properties were considered:

1. Inlet based on **model** flow rate (Figure 4.18A) - water at ~**20°C** (ρ = 1000 kg/m^3, μ = 0.001 N·s/m^2)
2. Inlet based on **model** flow rate (Figure 4.18A) - water at **37°C** (ρ = 993 kg/m^3, μ = 0.00069 N·s/m^2)
3. Inlet based on **patient** flow rate (Figure 4.18B) - water at **37°C** (ρ = 993 kg/m^3, μ = 0.00069 N·s/m^2)

4.5.3 CFD Results (Case 2)

The results for this section are based on the second case described at the end of the previous section. The velocity magnitude (Figures 4.19-4.22) and axial velocity (Figures 4.23-4.26) contours indicated high velocity regions within tight passages (CM and C3). In these regions, the CSF velocity exceeded 2 cm/s, and depending on time within cardiac cycle, the velocities reached up to 3.6 cm/s. This can be clearly observed in on the posterior side within CM region, where a jet is formed due to significant narrowing.

For the same case, the velocity vectors at the C2 level on XZ and YZ planes are shown in Figures 4.27 and 4.28 respectively. At this level, velocities did not exceed 1.5 cm/s. These vectors clearly indicated Womersley Flow like flow features. During the transition periods (systole to diastole and vice versa), horn-like velocity profiles were noticed. They indicated the out-of-phase interaction of viscous and momentum flow features.

Pressure contours (Figures 4.29 and 4.30) indicated fluctuations due to the changing of flow directions between systole and diastole phases. Based on this pressure, the data for longitudinal impedance was obtained at C2 and 25 mm above the C2 level to compute pressure drop.

The wall shear stress (WSS) contours shown in Figures 4.29 and 4.30, indicated regions where CSF fluid experienced higher resistance. These contours correlated well to regions where velocity contours exceeded 2 cm/s. The most noticeable section where WSS exceeds 1 dyne/cm^2 is in the same region which experiences the already mentioned jets.

4.6 Comparisons

4.6.1 Model MRI Versus CFD

Axial velocity profiles at the C2 level on the XZ and YZ planes were plotted along with pcMRI data from the model flow (Figures 4.33 and 4.34). The location was the same as vector plots in Figures 4.27 and 4.28. The comparison showed that both were in phase and approximately the same magnitude. Although the axial velocity profile shapes did not always match, considering the noise in the MRI, the agreement between CFD and experimental results was reasonably good.

4.6.2 20°C Versus 37°C

For the model flow at temperatures of 20°C and 37°C pressure drop and longitudinal impedance was computed (Figure 4.35). The resulting $/M_L$ value for both cases has shown that

there is no significant difference between two of the cases. Cases with 20°C and 37°C had $\int M_L$ equaling 353 and 362 dynes/cm^5 respectively. This resulted in a $\Delta = 2.5\%$.

4.6.3 Patient CFD Versus Model CFD

Similarly to the previous section, along with model case 2, pressure drop and longitudinal impedance was computed for case 3, where the patient's flow waveform was used as inlet BC (Figure 4.35). The resulting $\int M_L$ value for both cases has shown that there is still a small difference between both of the cases. Cases with model flow at 37°C and actual patient flow had $\int M_L$ equaling 362 and 343 dynes/cm^5 respectively. This resulted in a $\Delta = 5.4\%$.

4.7 Discussion

The waveforms of the patient (Figure 4.2) demonstrated similar magnitudes with a small phase shift of 0.05 s from the C2 level to C7. The phase shifts occurred due to the compliant nature of the spinal cord and the thin layer of tissue along the spine. Compliance of the spinal canal must exist due to the soft tissue of the spinal cord as evidenced by the phase shift of flow waveforms at different axial locations.

The compliance issue arises since the experimental model was nearly rigid and the CFD model assumed rigid walls. Throughout comparisons of patient versus the experimental model, and further the experimental model versus CFD models, the parameters remained relatively close to each other as shown in previous sections. Although compliance has potential implications in CSF flow within SAS both in the cranium and spinal canal, the short section that was used for CM modeling studies make a rigid assumption reasonable. Current MR technology gives geometrical representation of the spinal canal as a static image that represents overall volume for

CSF. During a cardiac cycle, the wall displacement is too small for the MR scanner to capture, therefore current rigid assumption accommodates the current abilities of MR scanners. The CM patient's representative flow resistance value that can be computed on a 3-D geometry and unsteady cyclic flow has already a significant advantage in terms of its dynamic characteristics over current "gold standard" static analysis of 2-D MR images.

The comparison of two cases at slightly different density and viscosity (water at 20°C and 37°C) indicated Δ = 2.5% change in longitudinal impedance. This indicates that experiments conducted with water at room temperature would not result in significant resistance changes when compared to that at 37°C. As already mentioned, CSF is a water-like liquid which has similar density and viscosity to water at 37°C. The CFD simulations showed that the studies performed with water in a 20-37°C span are relevant to anatomic CSF flow.

The comparison of two cases of different flow waveforms as input generated Δ = 5.4% change in longitudinal impedance. Although acceleration aspects of each flow waveform were different (Figure 4.11A), the longitudinal impedance as shown in Figure 4.35 was similar within the 1-8 harmonic range that is used for integrated (overall) resistance value. In this case, the CFD simulations showed that the studies performed on the same SAS geometry with different flow waveforms were similar. This leads to the conclusion that resistance is highly dependent on geometry and, to a lesser degree, on the flow waveform shape. It is important to point out that the length of the cardiac cycle (i.e. period) could be more significant than flow shape.

In brief conclusion, this section demonstrated that the experimental and CFD model reproduced an in-vivo hydrodynamic environment within the upper cervical region in the CM patient.

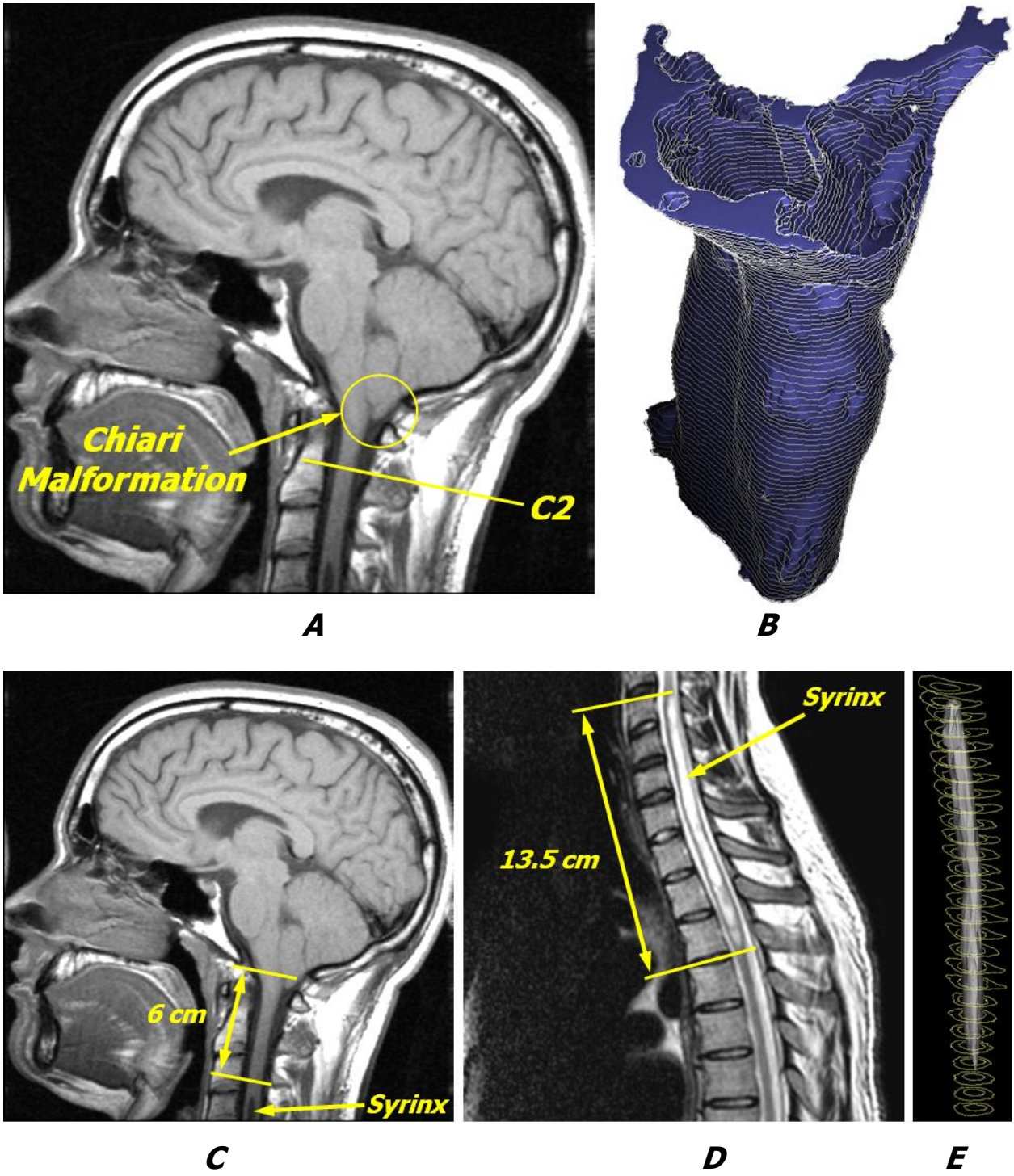

Figure 4.1. CM patient 3-D reconstructions of SAS in two zones: **A.** MR image of sub-cranial zone with CM blockage and C2 location, **B.** 3-D reconstruction of sub-cranial SAS, **C.** Sub-cranial zone reference and syrinx location, **D.** Syrinx zone reference, and **E.** 3-D reconstruction of syrinx and SAS around the syrinx.

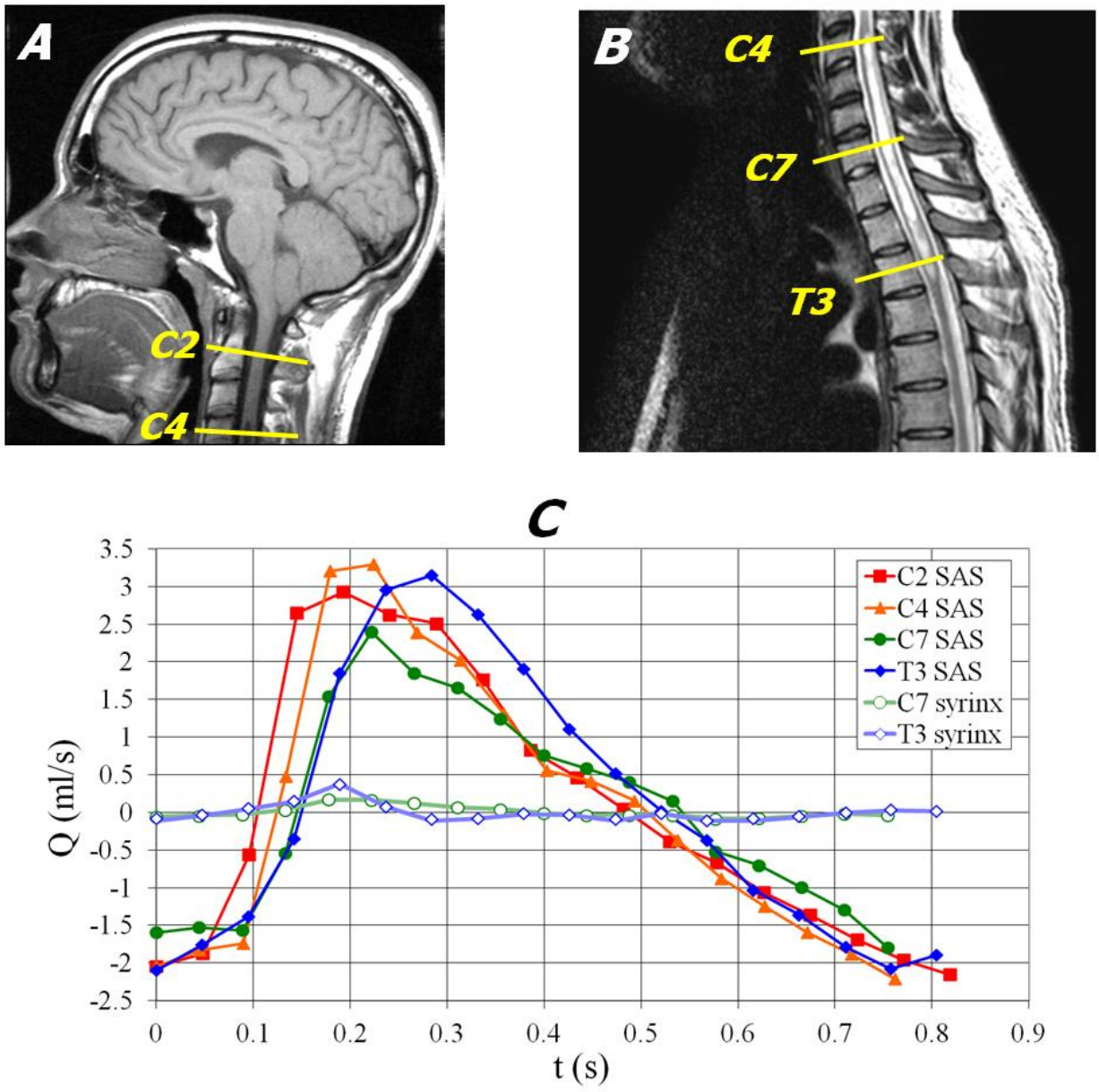

Figure 4.2. CM Patient flows: **A.** Position reference for C2 and C4, **B.** Position reference for C4, C7 and T3, and **C.** SAS and syrinx flow waveforms at multiple locations.

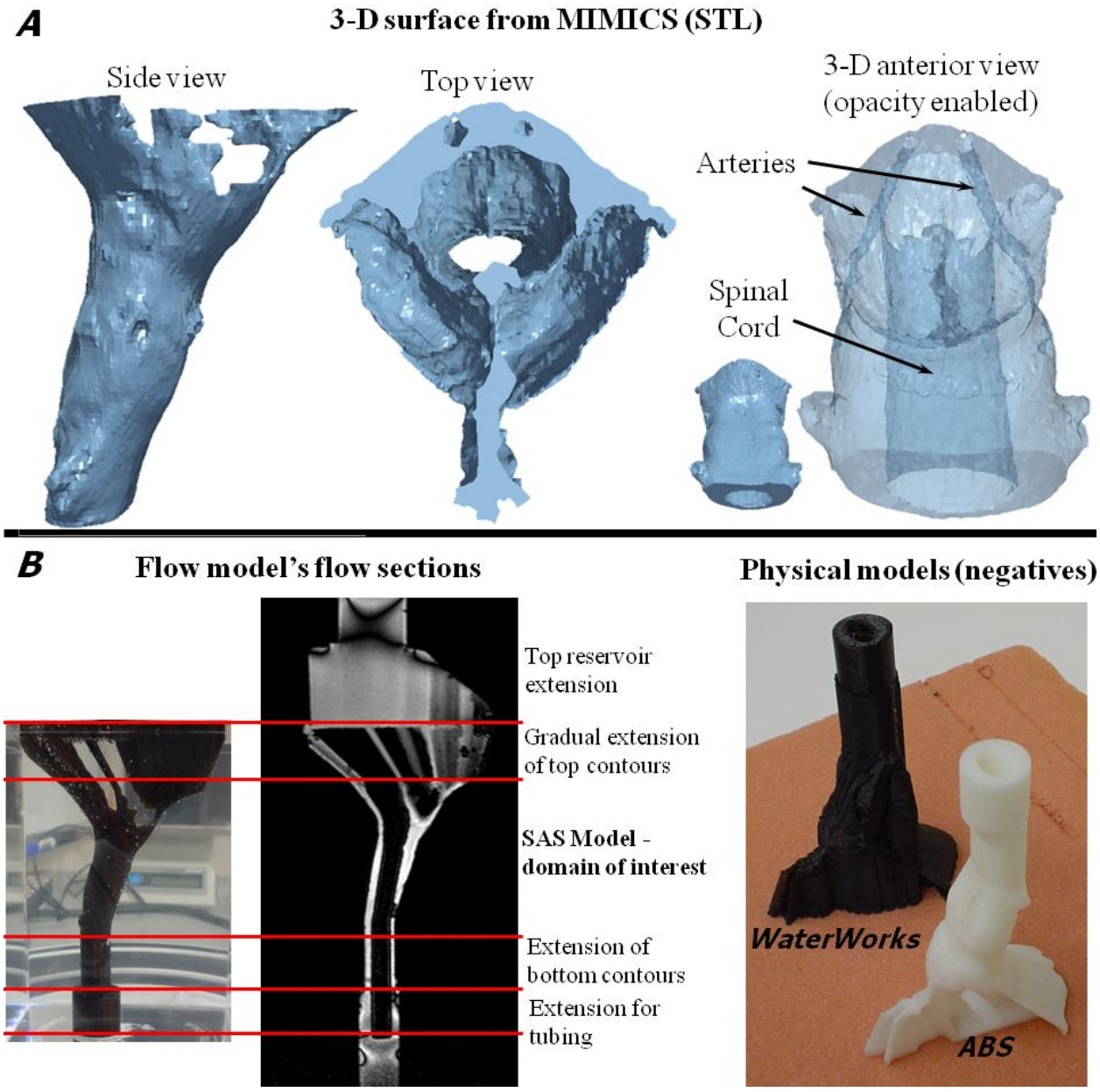

Figure 4.3. 3-D reconstruction of CM patient's obstructed SAS exported from MIMICS (STL format): **A.** 3-D views of SAS blockage, **B.** Addition of extensions.

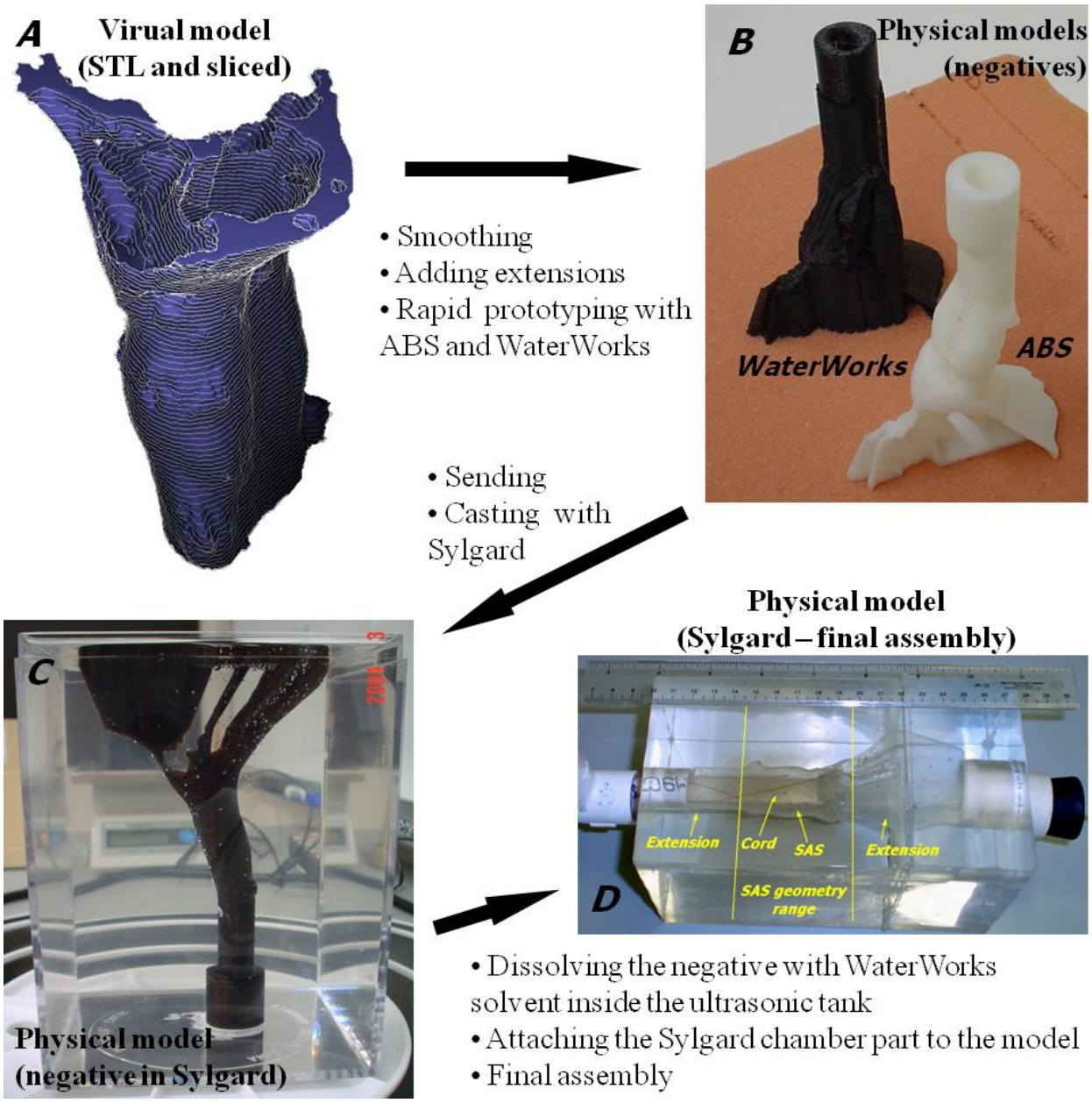

Figure 4.4. Procedure for building the 3D model of CM: **A.** Virtual 3-D model, **B.** Rapid prototyping models, **C.** Model curing inside Sylgard, and **D.** Fully assembled model of CM.

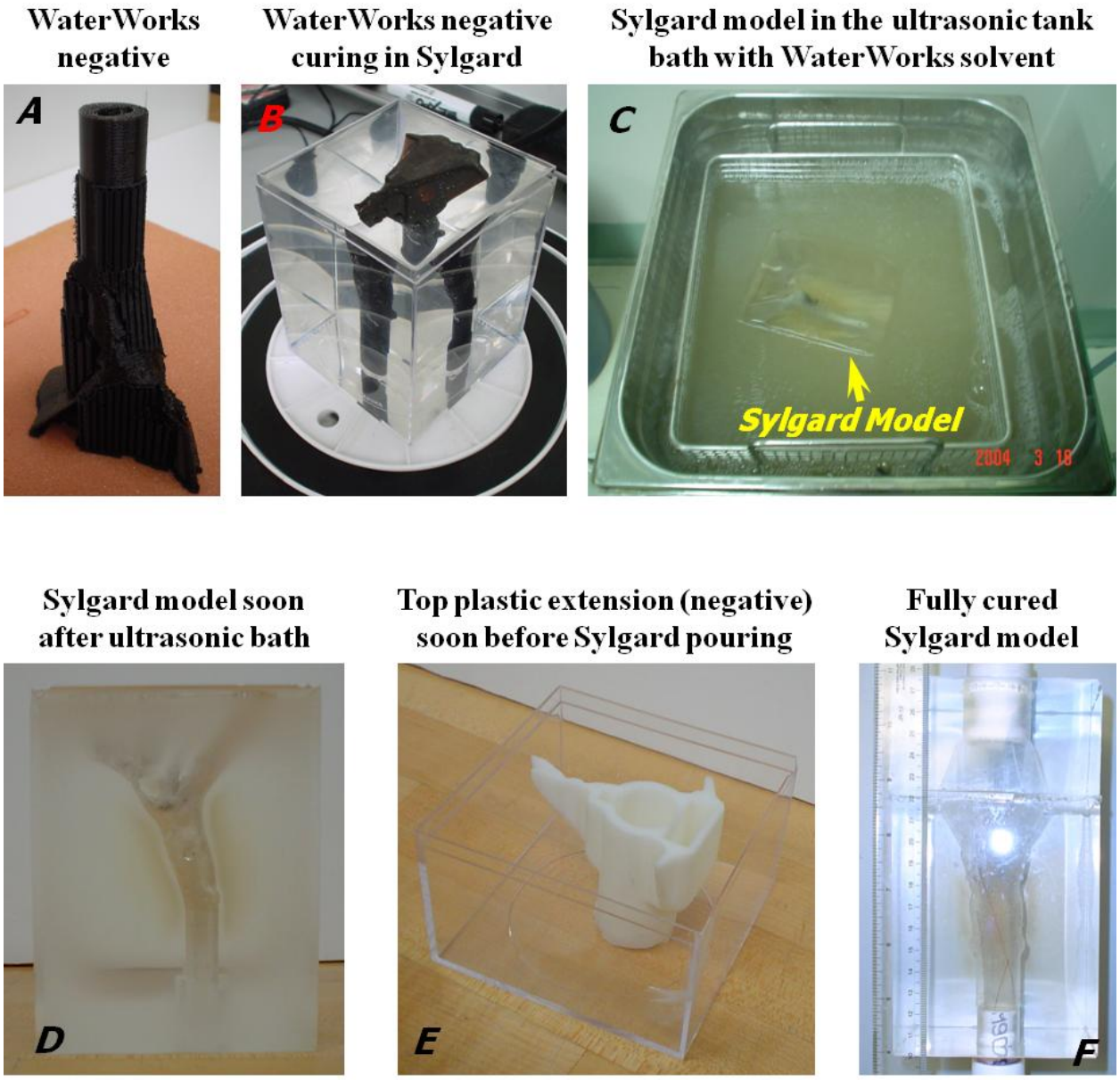

Figure 4.5. Working CM model: **A.** WaterWorks negative CM geometry, **B.** CM negative curing in Sylgard, **C.** WaterWorks dissolving in solvent bath inside ultrasonic tank, **D.** Fully dissolved Sylgard model soon after the bath. **E.** Top extension negative for the model, and F. Fully cured model after attachment of top extension.

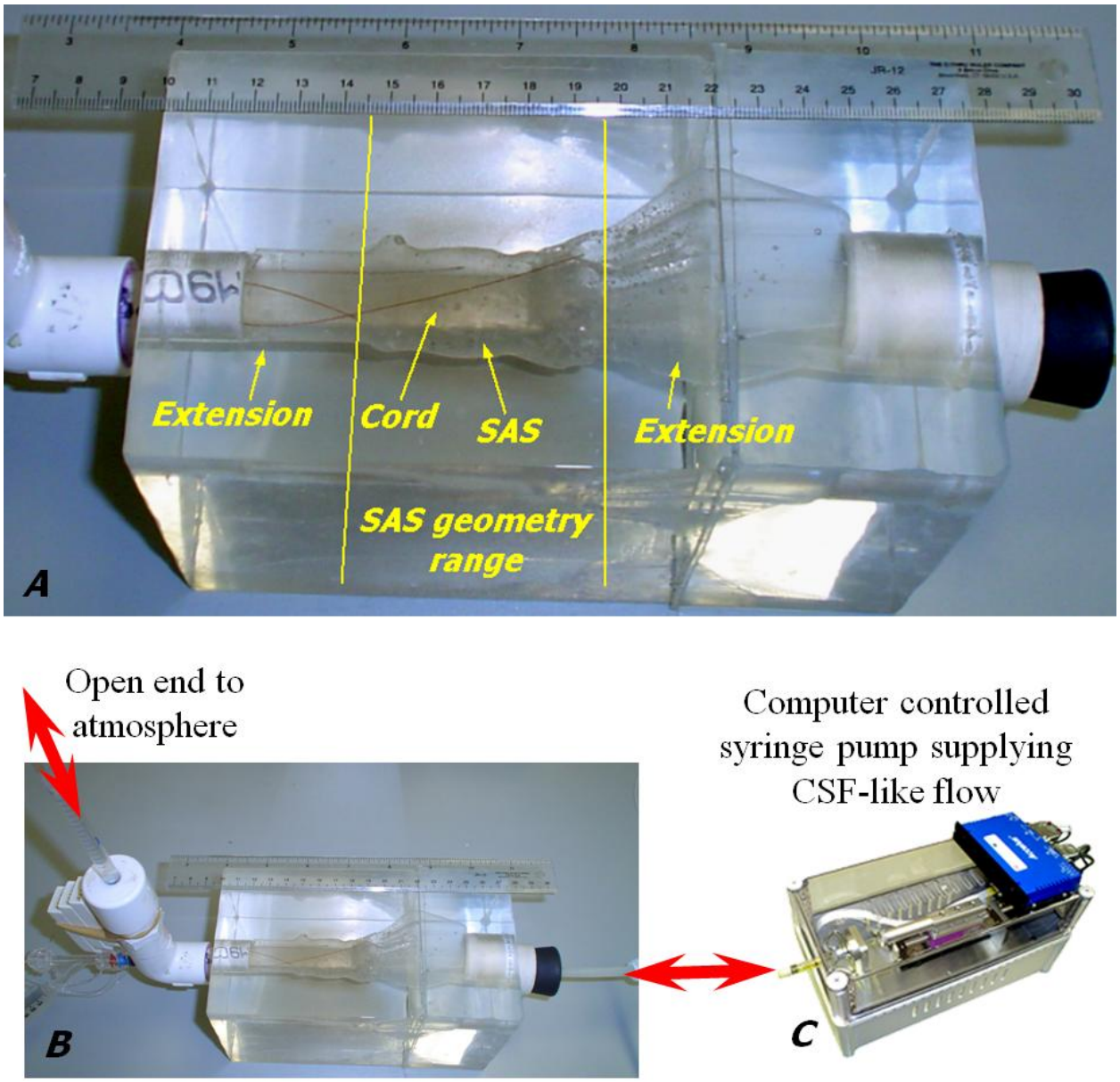

Figure 4.6. Working CM model: **A.** Domain of interest within the model, **B.** Assembled flow model, and **C.** Pulsatile pump.

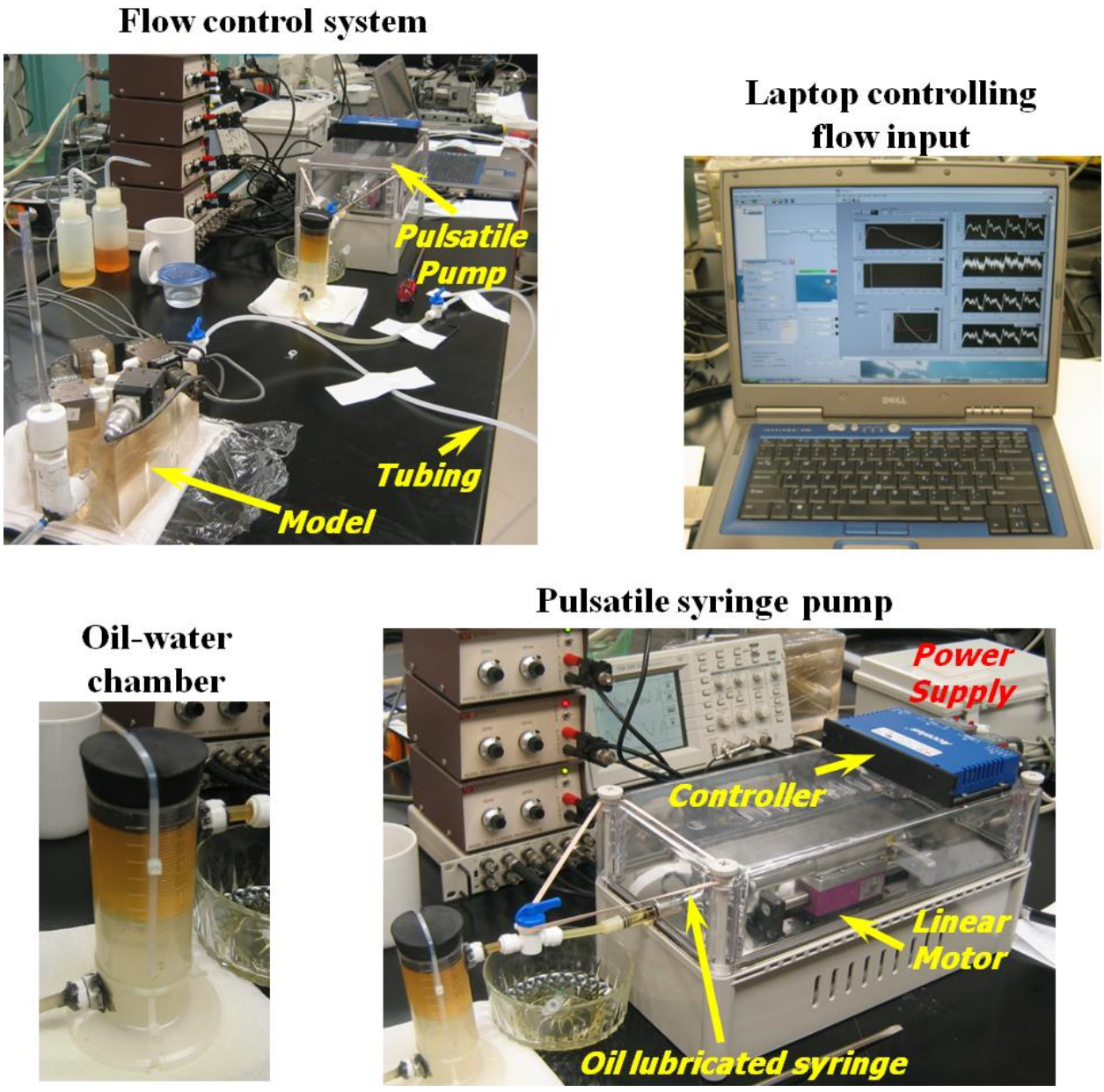

Figure 4.7. Control system for linear motor-based pulsatile pump.

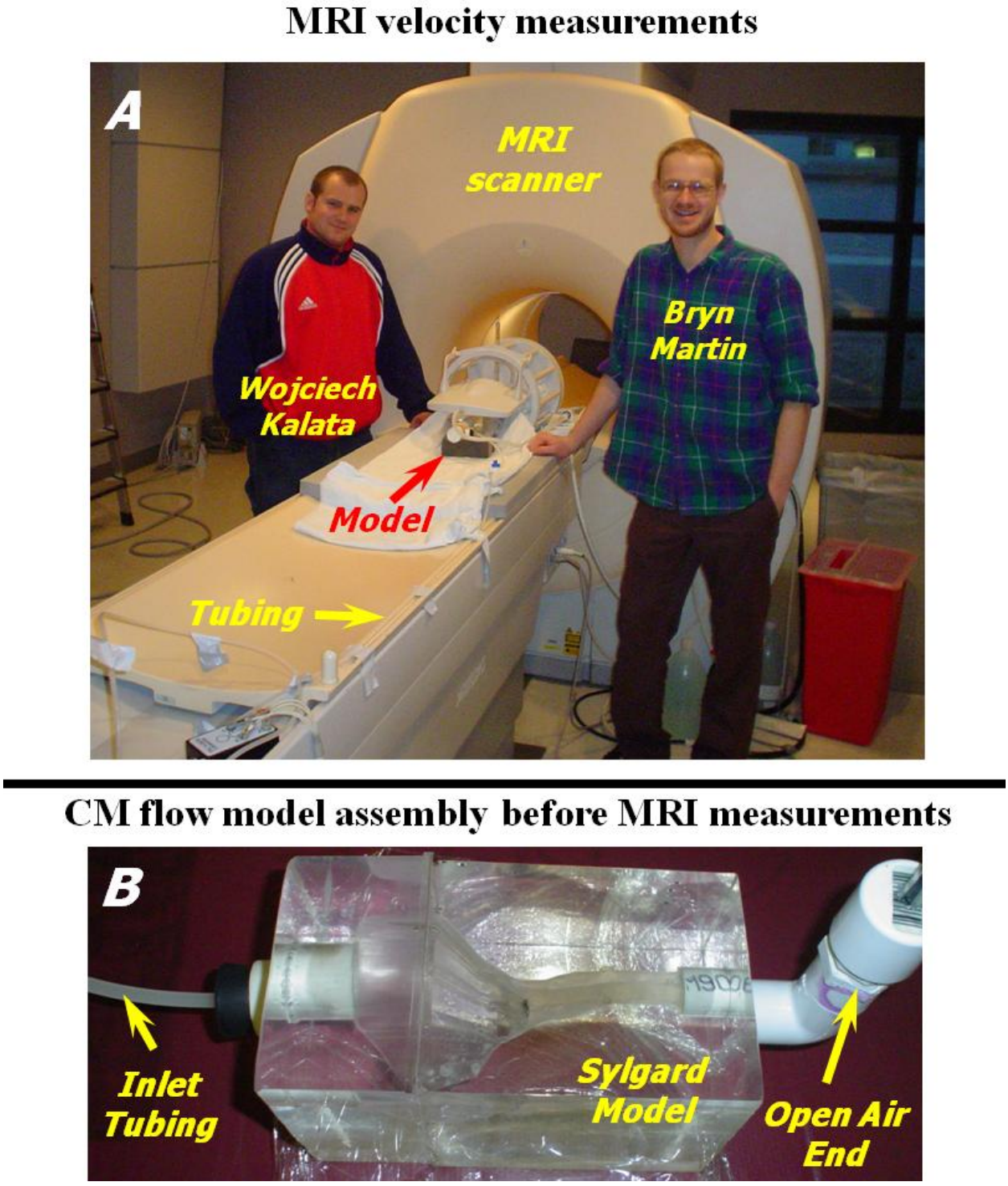

Figure 4.8. Velocity measurements with MRI scanner: **A.** General setup inside for MRI measurement. **B.** CM model used in the MRI test.

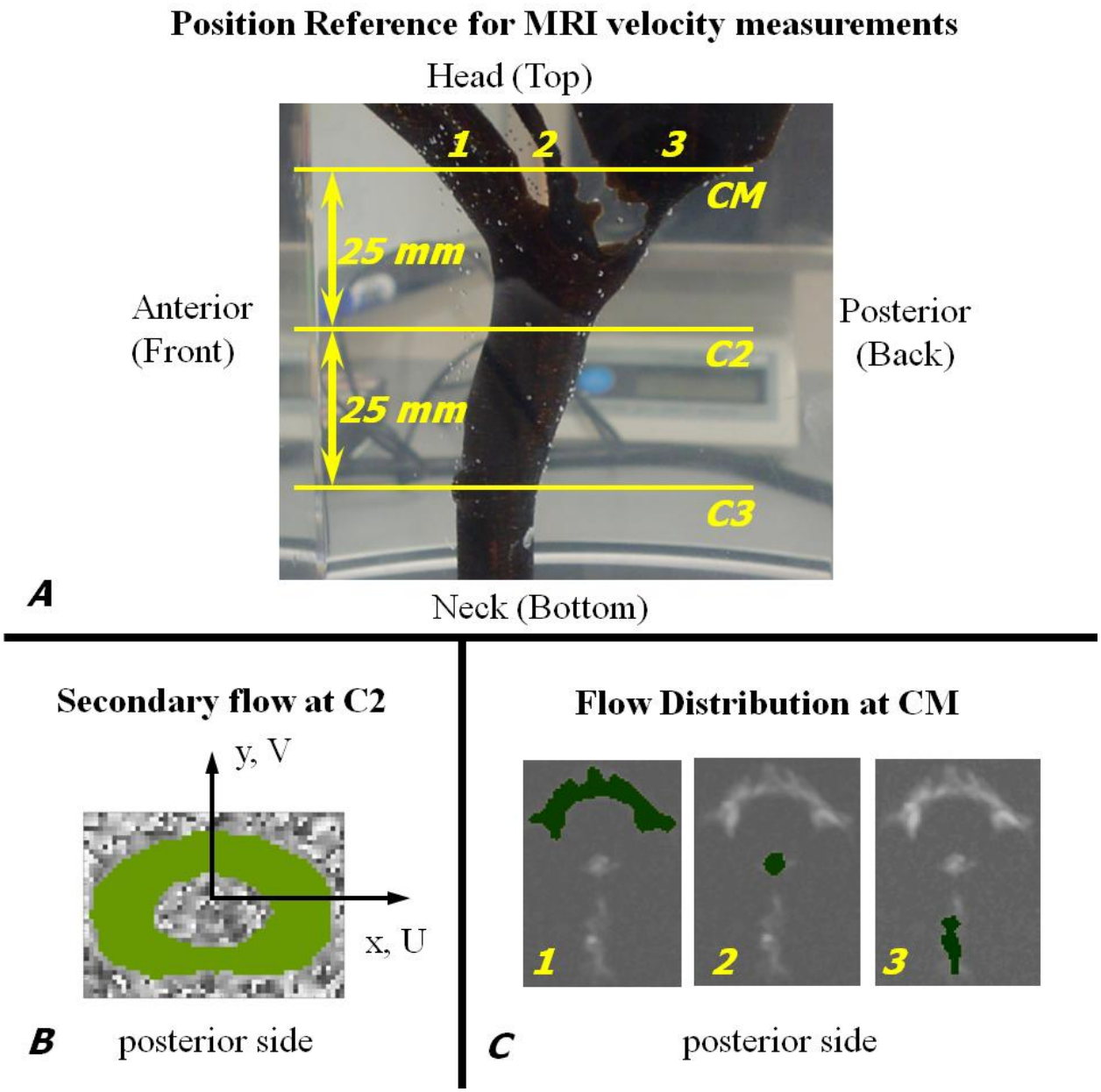

Figure 4.9. Velocity measurements with MRI scanner: **A.** Axial locations and CM level flow distribution, **B.** Reference for secondary flow at C2, and **C.** Masking for flow distribution at CM level

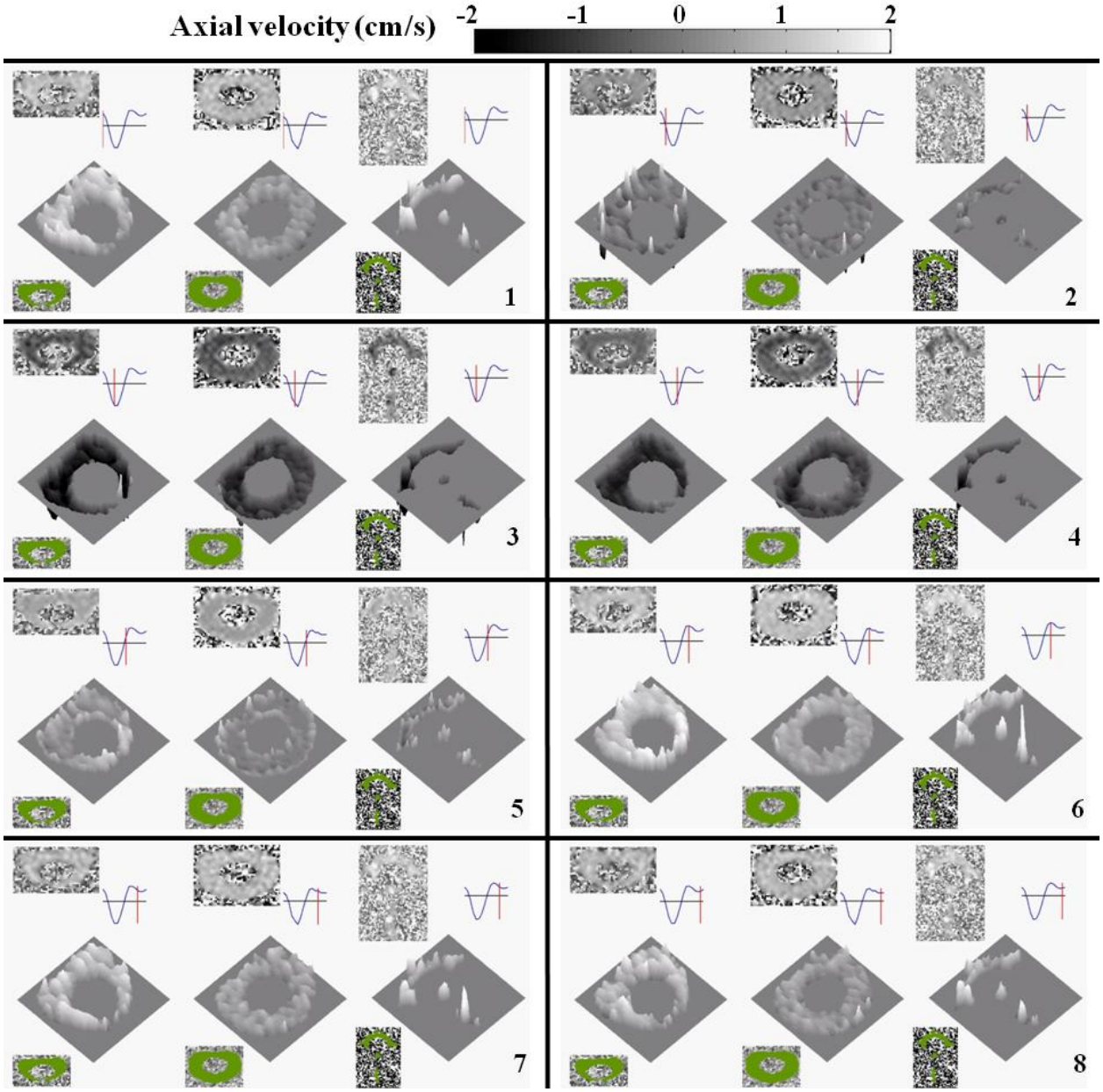

Figure 4.10. Flow visualization from MRI experiments. Surface plots of axial velocity at three axial locations CM, C2 and C3 (see Figure 4.9A for position reference).

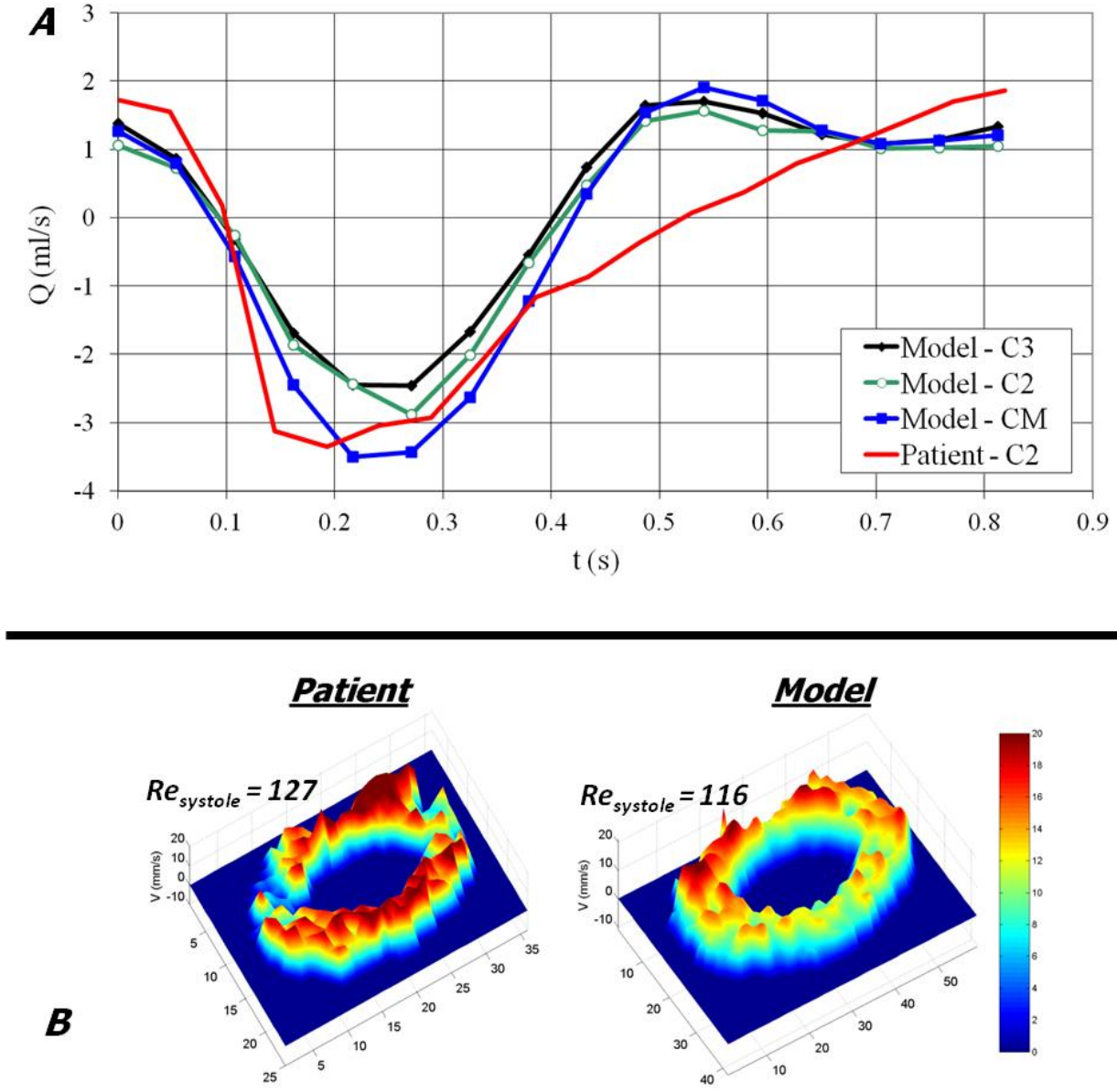

Figure 4.11. Flow waveforms from MRI experiments. Comparison to CM patient is included: **A.** Flow waveforms at three axial locations (position reference is shown in Figure 4.9, **B.** Axial velocity distribution at C2 at systolic flow peak.

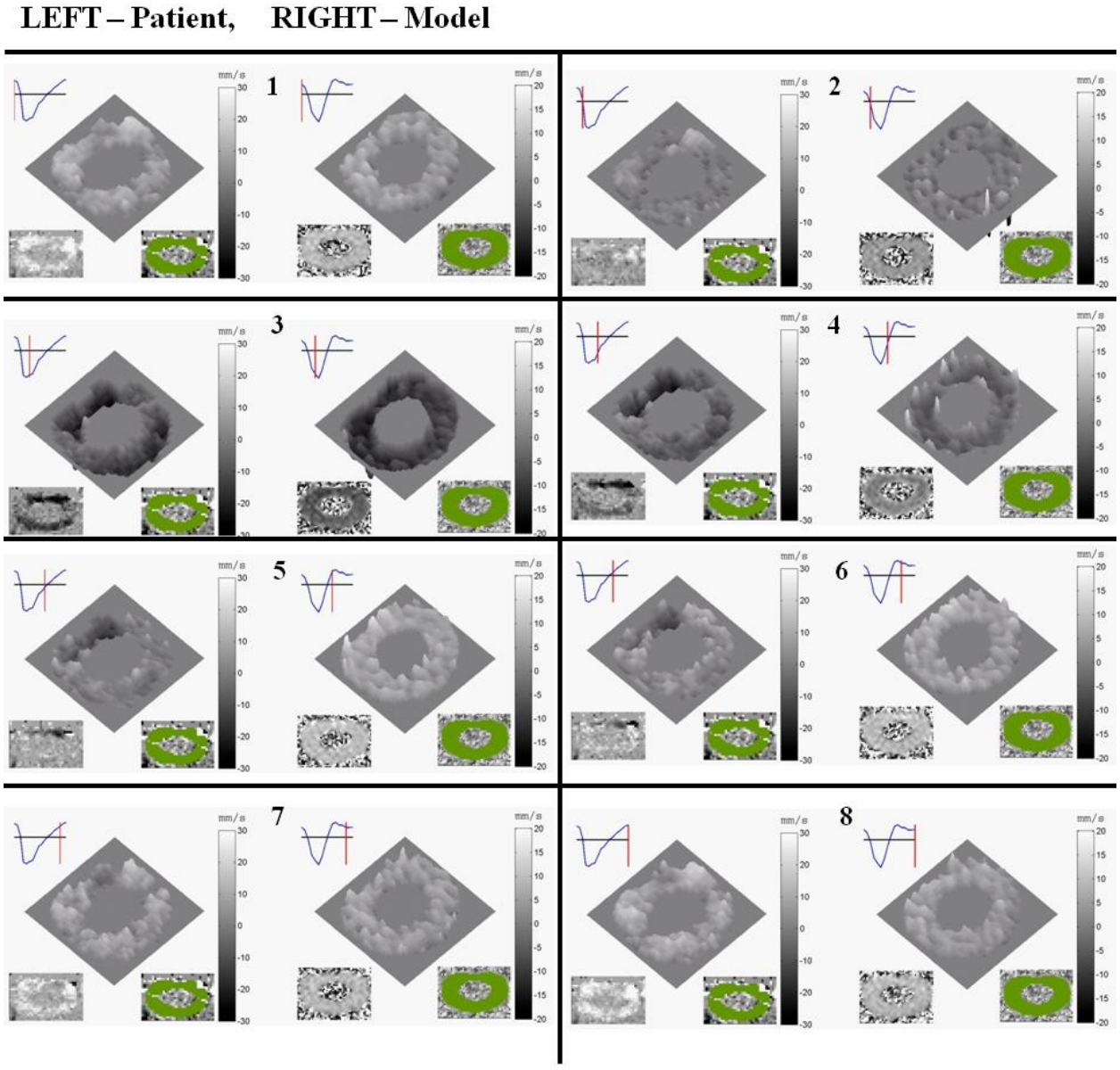

Figure 4.12. Flow visualization from MRI experiments. Surface plots of axial velocity at C2 compared with velocities from CM patient.

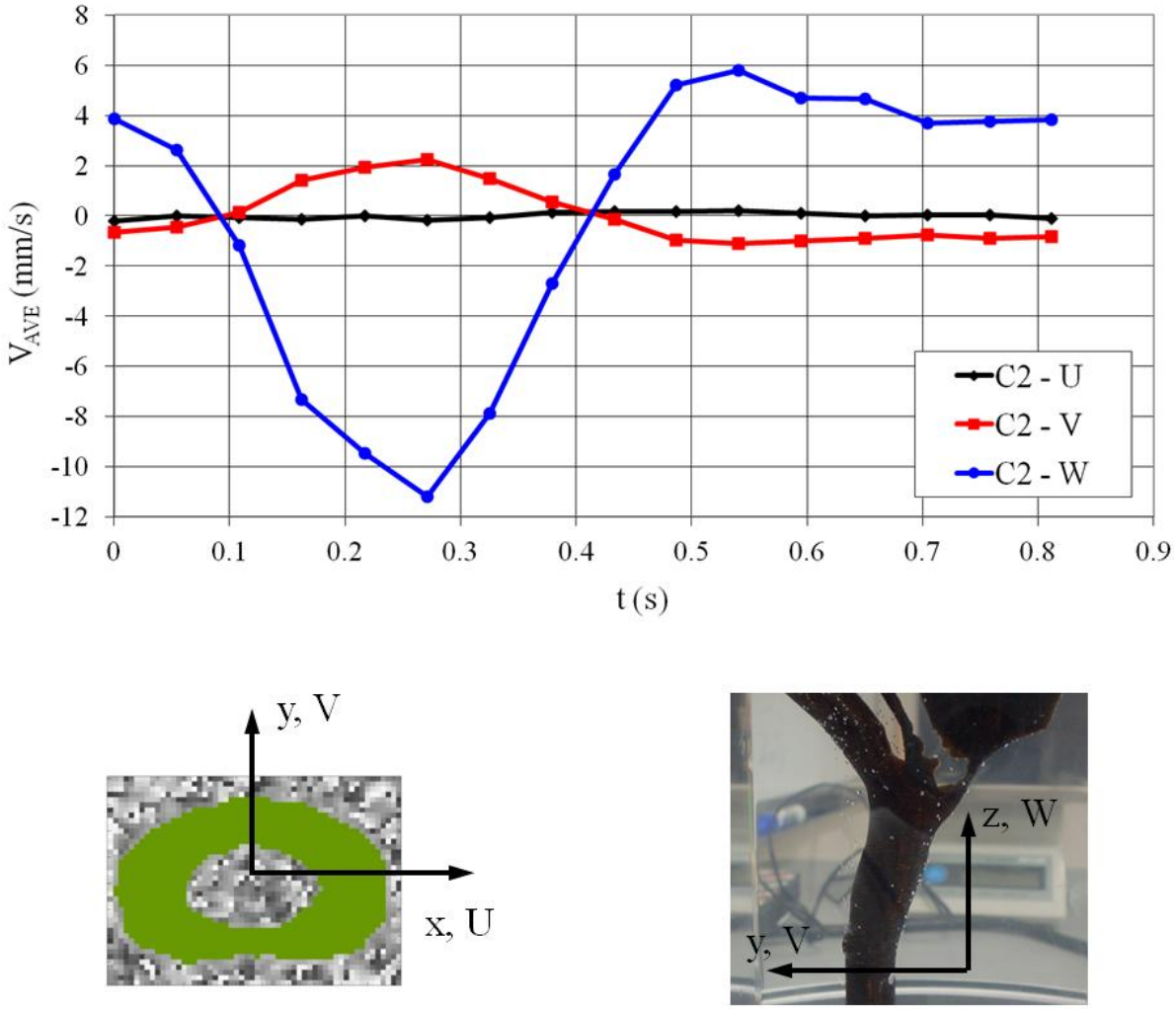

Figure 4.13. Spatially averaged 3-D velocity at C2 with corresponding coordinate orientation.

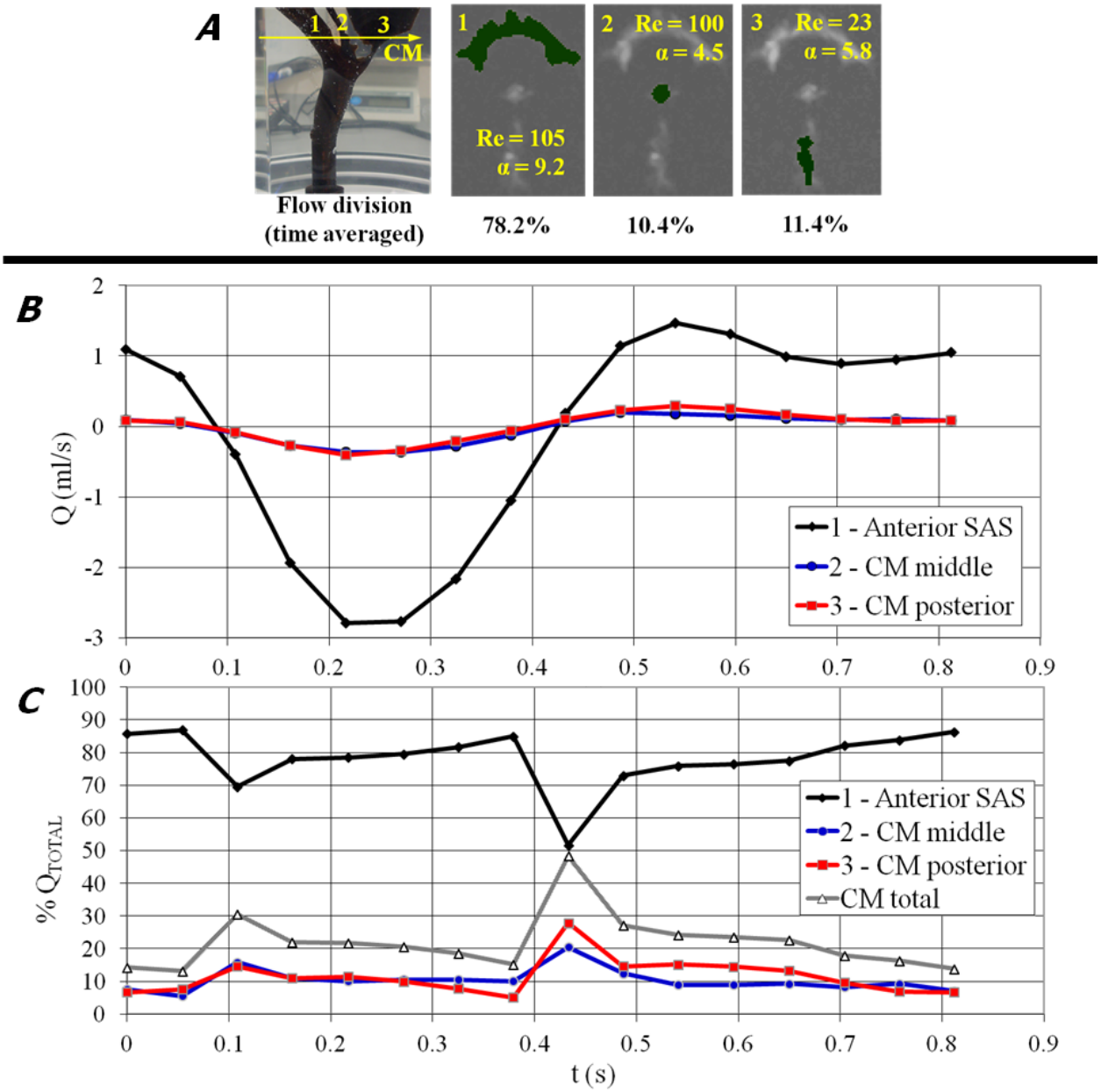

Figure 4.14. Flow distribution (split) at CM level in three separate regions. **A.** Position reference and their hydrodynamic parameters, **B.** Volumetric flow distribution for the regions, **C.** Percentage of total flow.

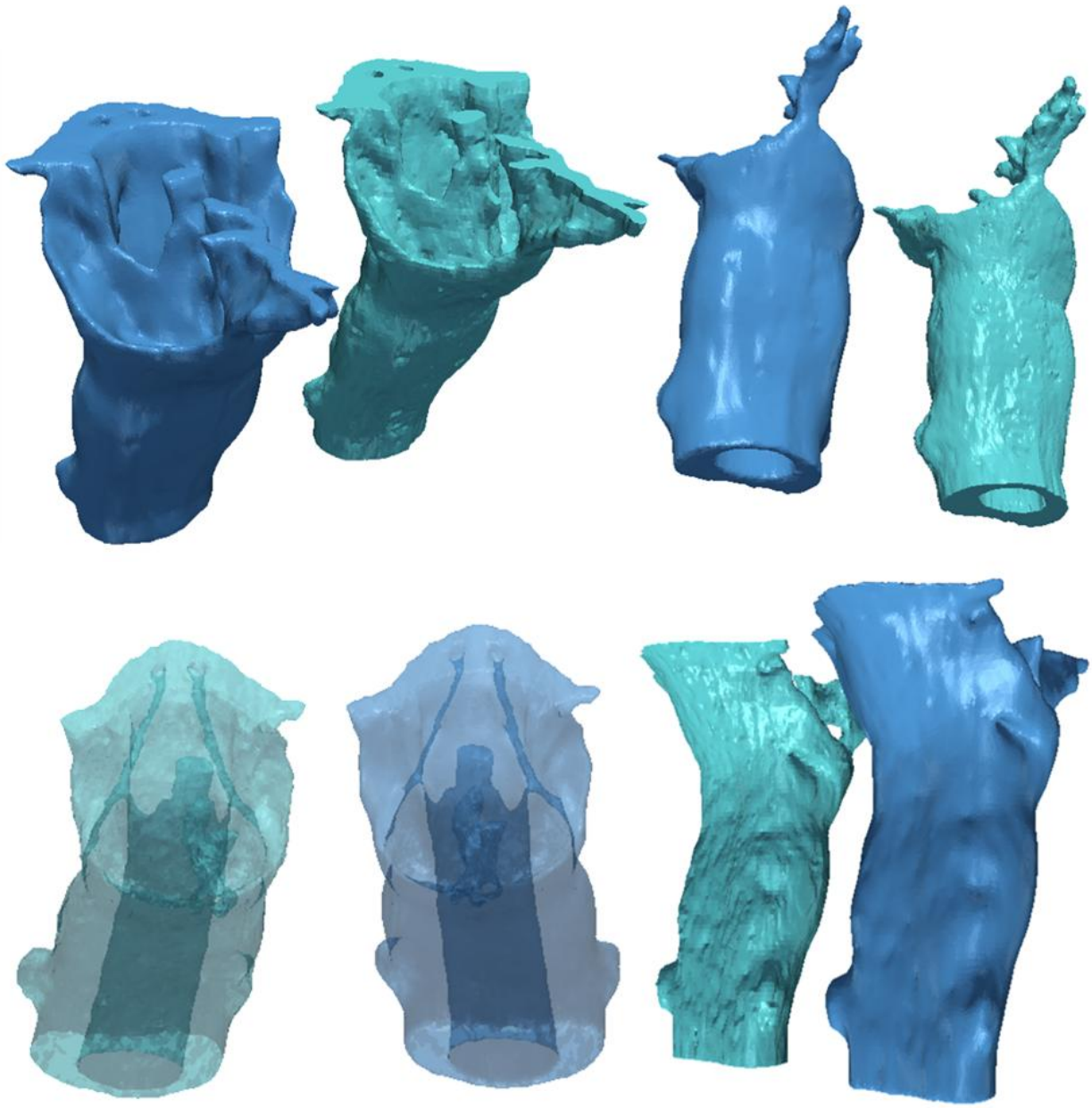

Figure 4.15. SAS wall surfaces for meshing (STL). Surface geometry before smoothing (cyan) and surface geometry after smoothing (blue).

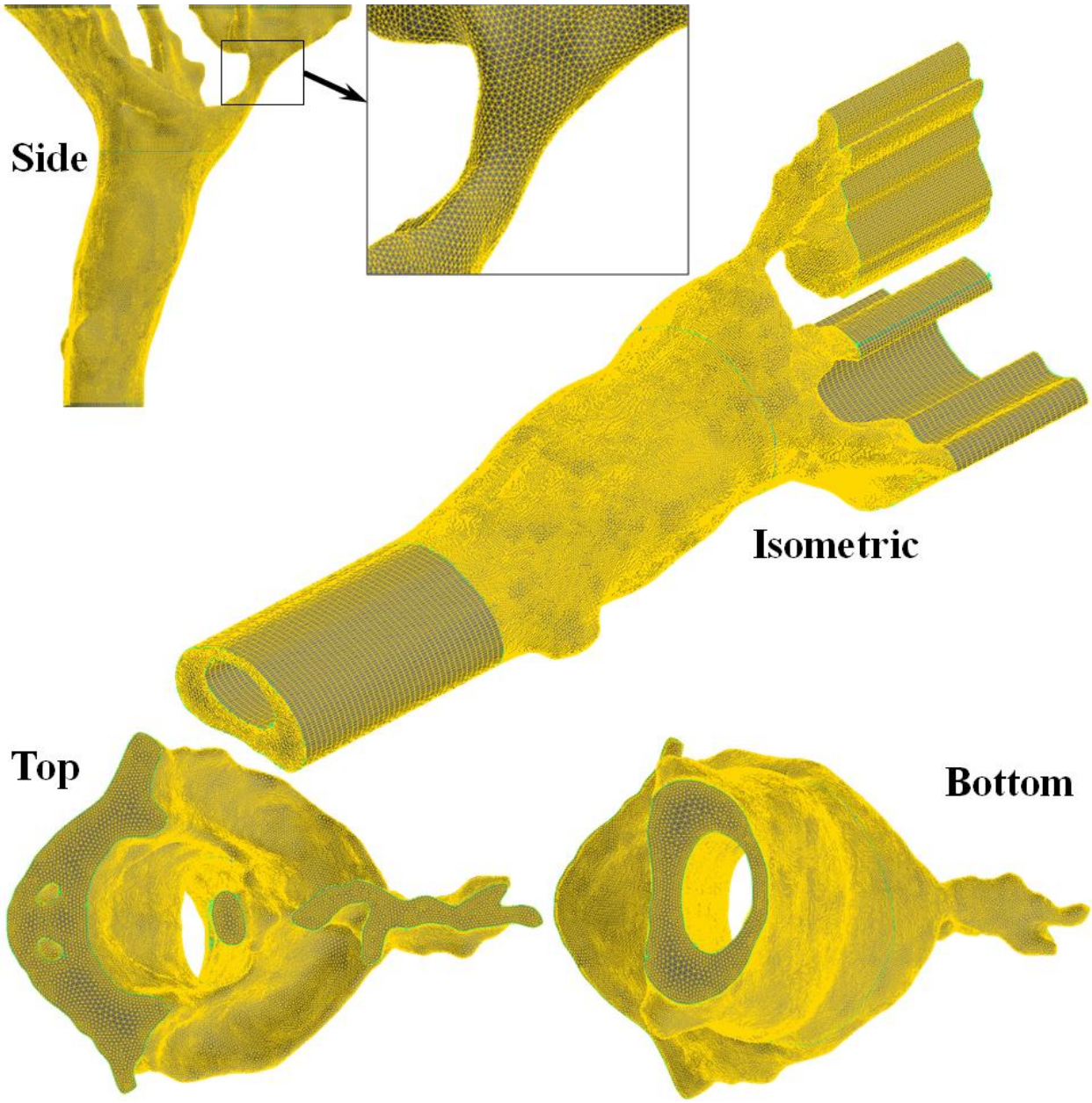

Figure 4.16. Tetrahedral mesh with triangle mapped extensions (3,654,042 cells).

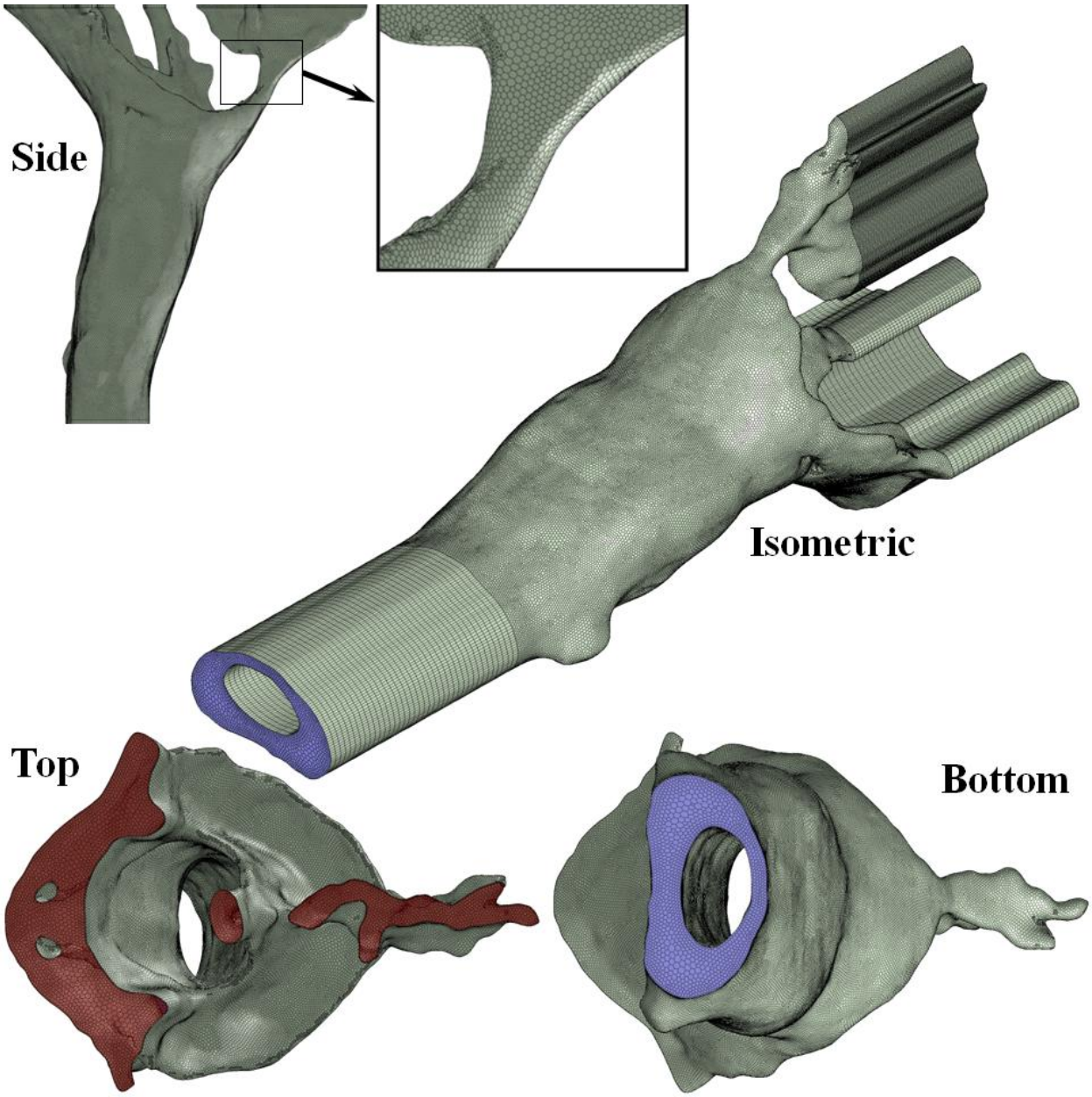

Figure 4.17. Polyhedral mesh with polygon mapped extensions (912,918 cells).

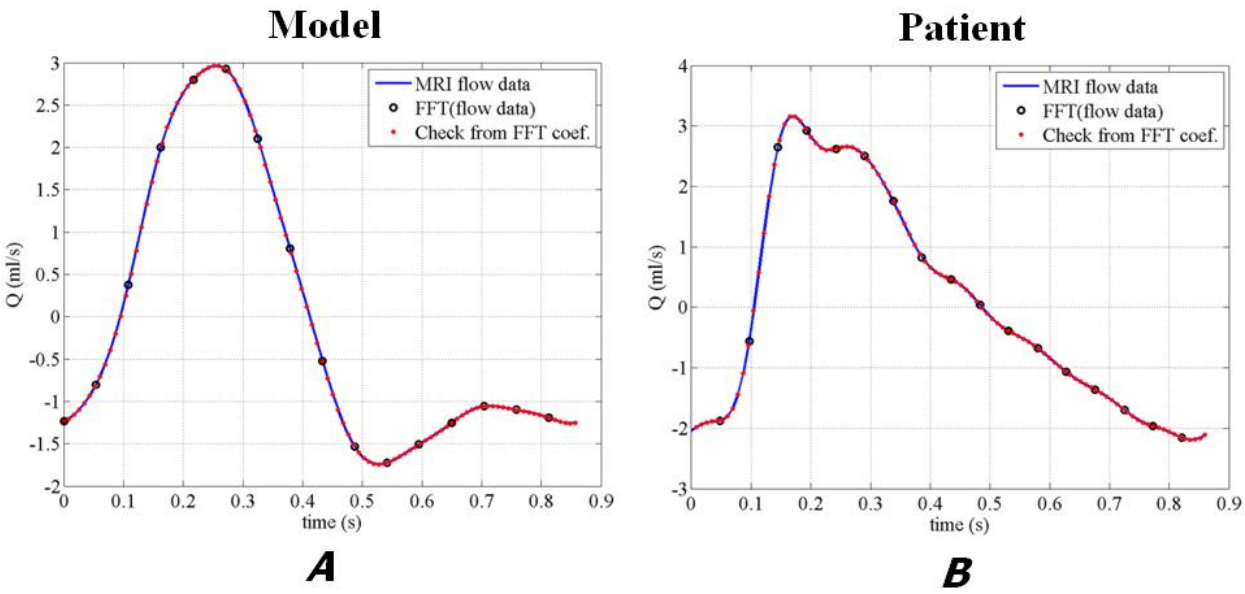

Figure 4.18. Flow waveform inputs: **A.** Model flow waveforms, **B.** Patient flow waveform.

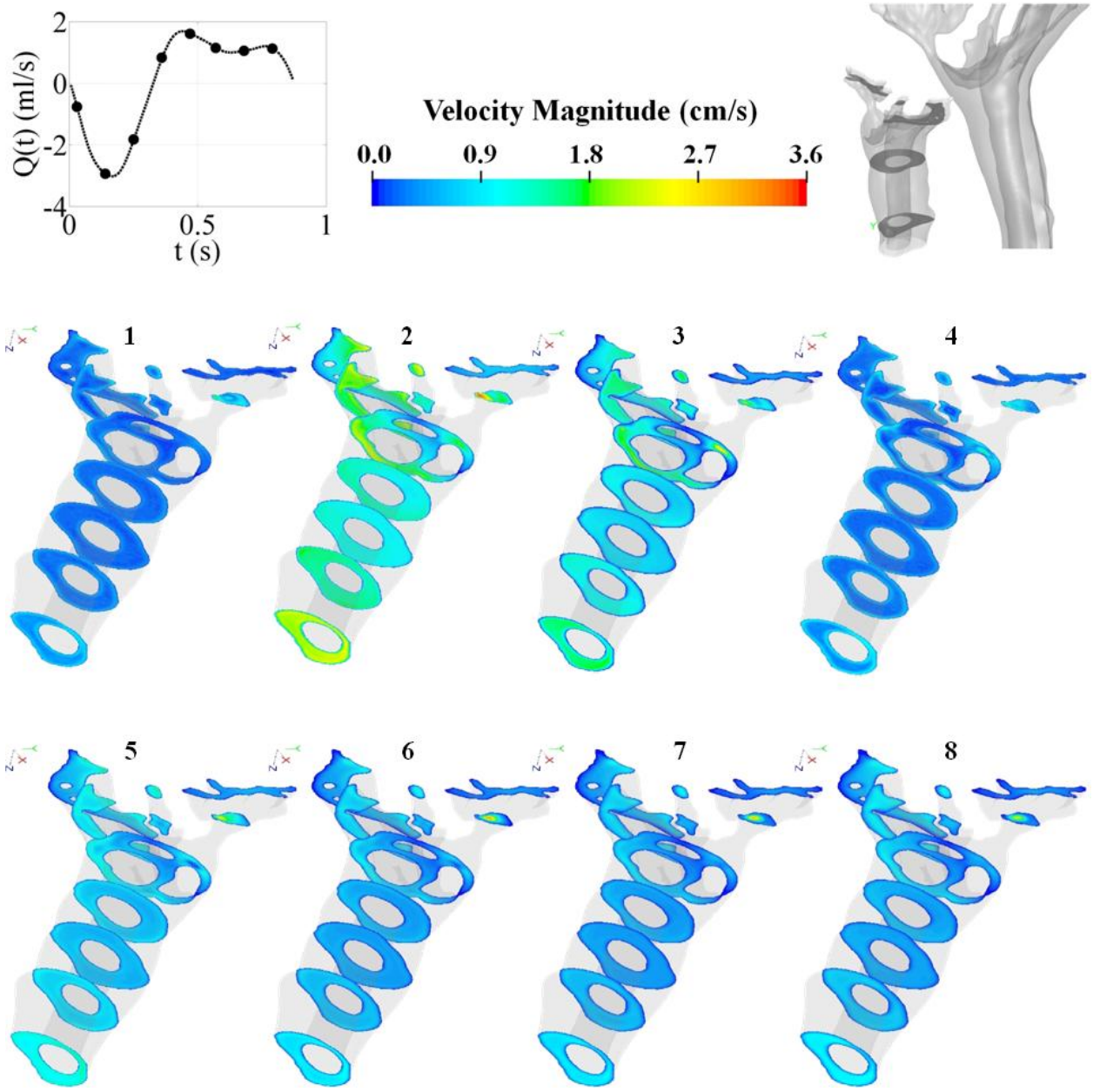

Figure 4.19. Velocity magnitude contours on multiple axial planes at 8 time points within a cardiac cycle.

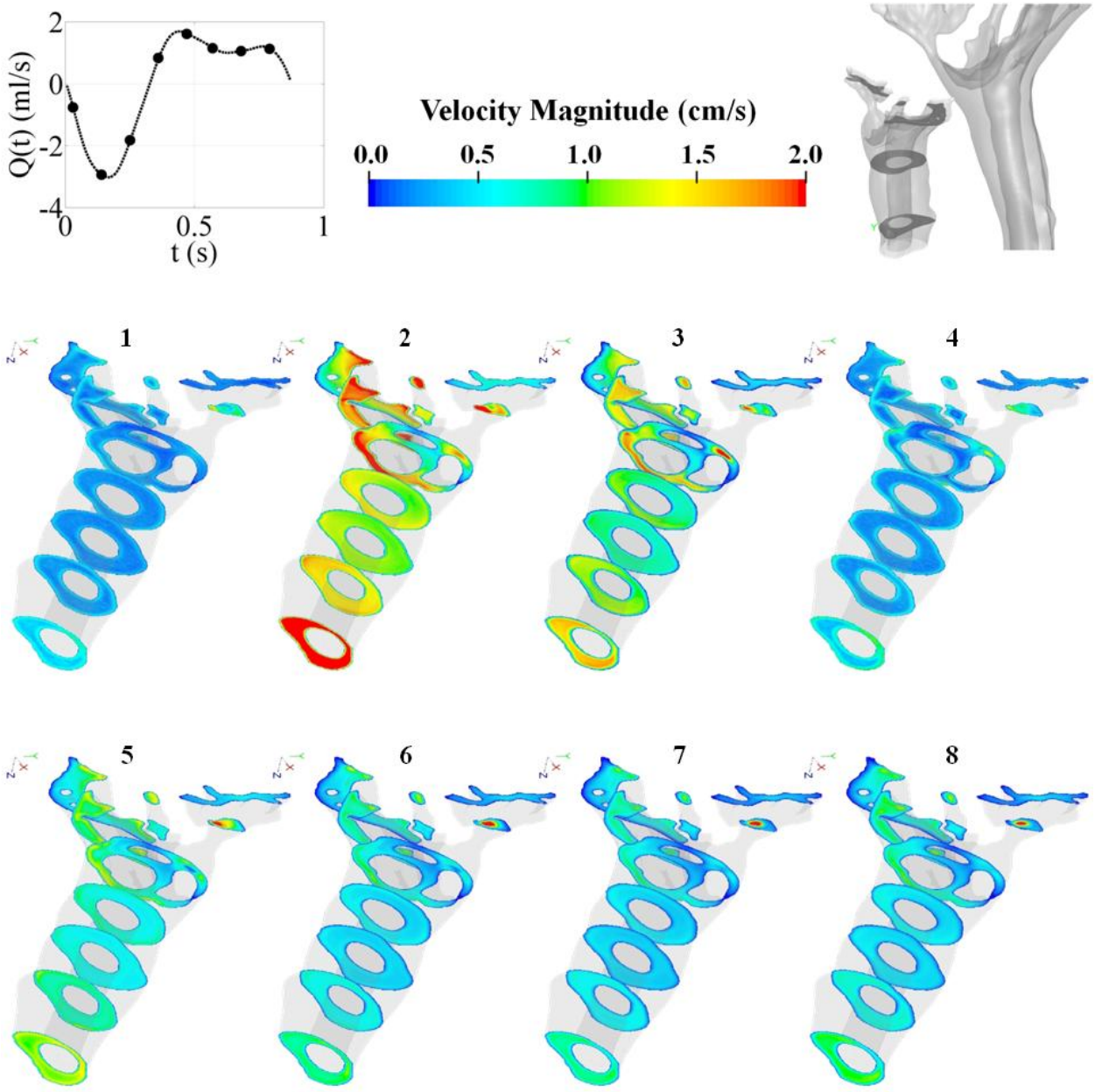

Figure 4.20. Velocity magnitude contours on multiple axial planes at 8 time points within a cardiac cycle. Velocity range reduced to highlight differences within flow field.

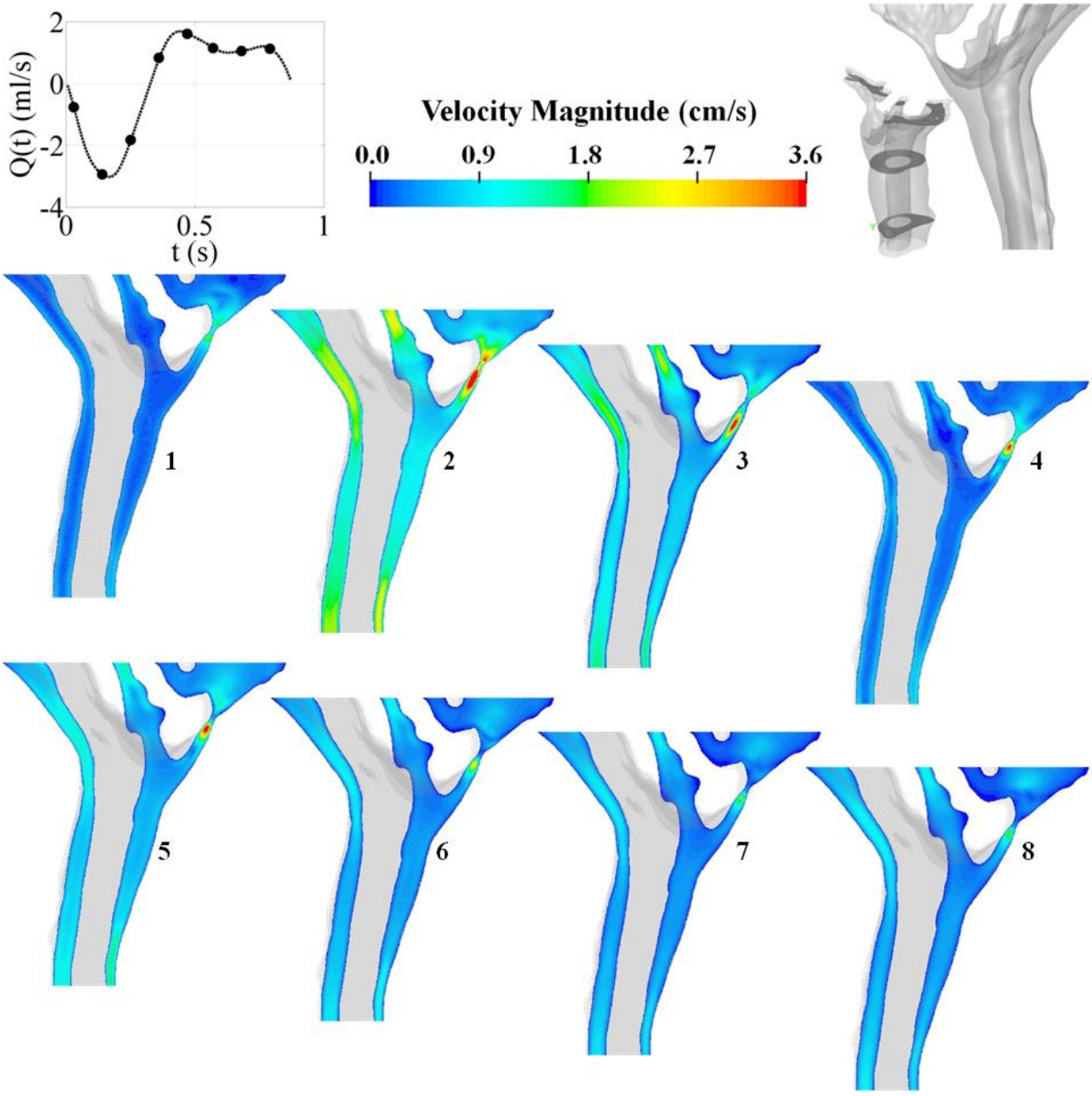

Figure 4.21. Velocity magnitude contours on mid-sagittal plane at 8 time points within a cardiac cycle.

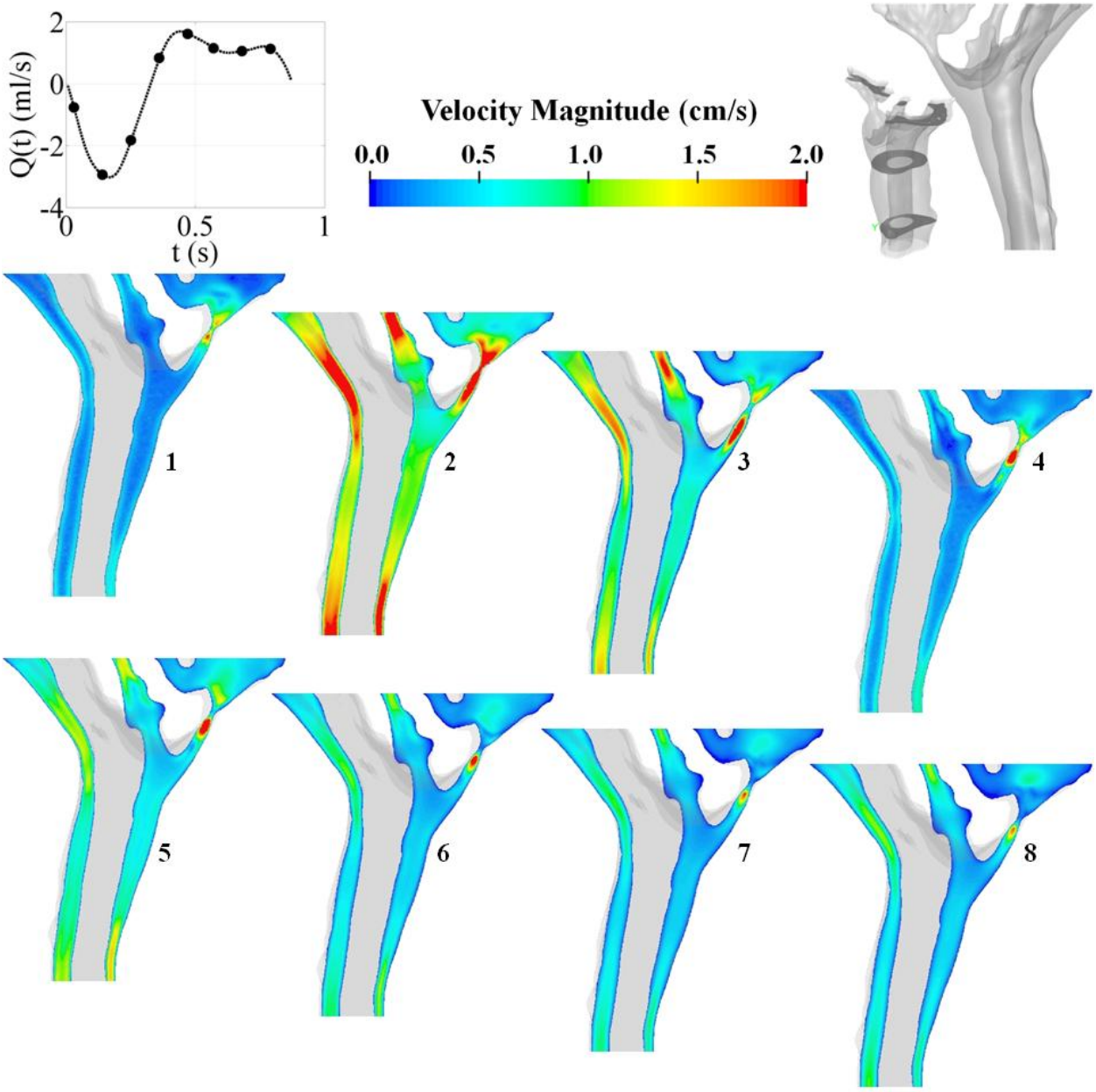

Figure 4.22 Velocity magnitude contours on mid-sagittal plane at 8 time points within a cardiac cycle. Velocity range reduced to highlight differences within flow field.

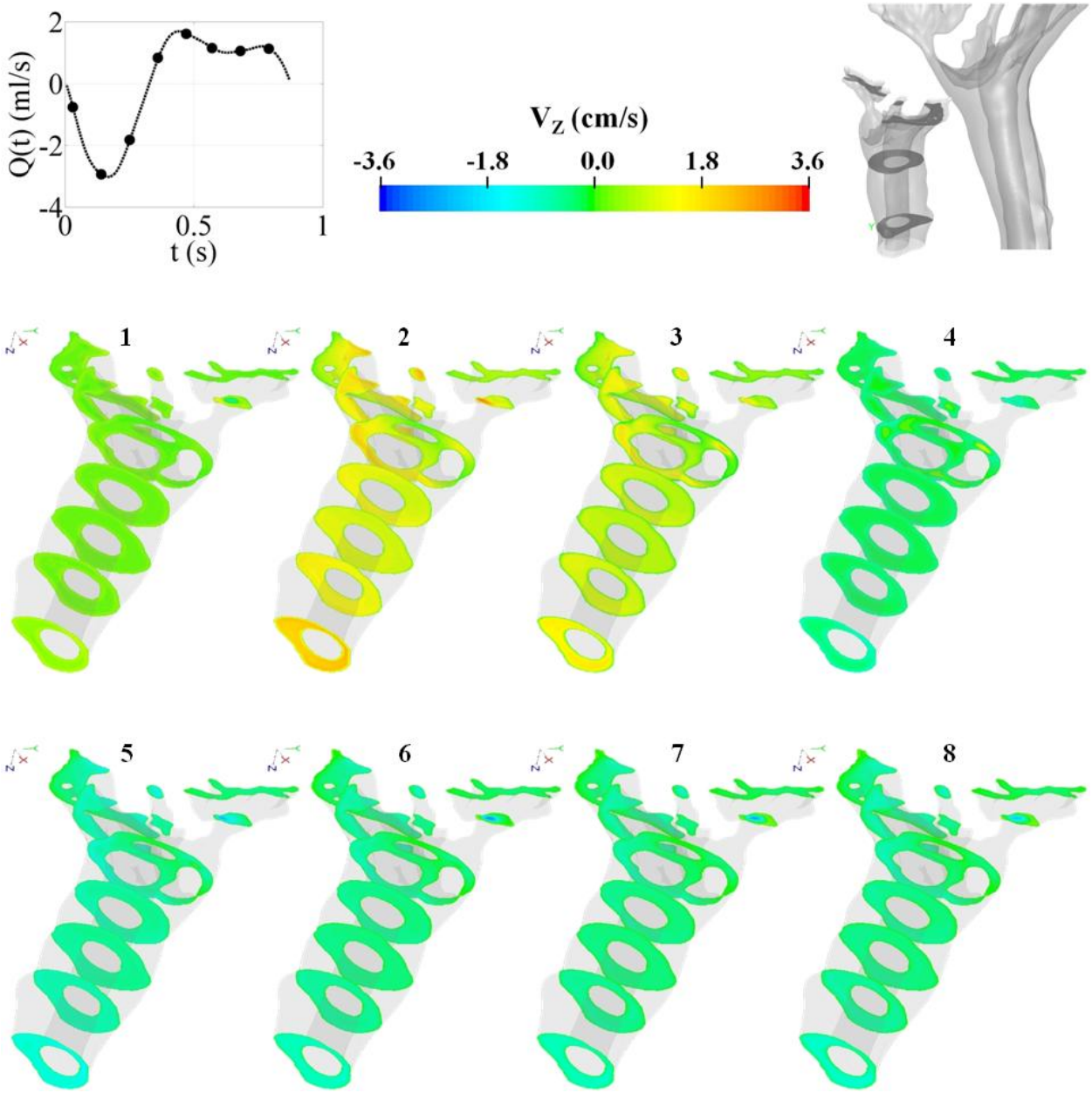

Figure 4.23. Axial velocity (V_Z) contours on multiple axial planes at 8 time points within a cardiac cycle.

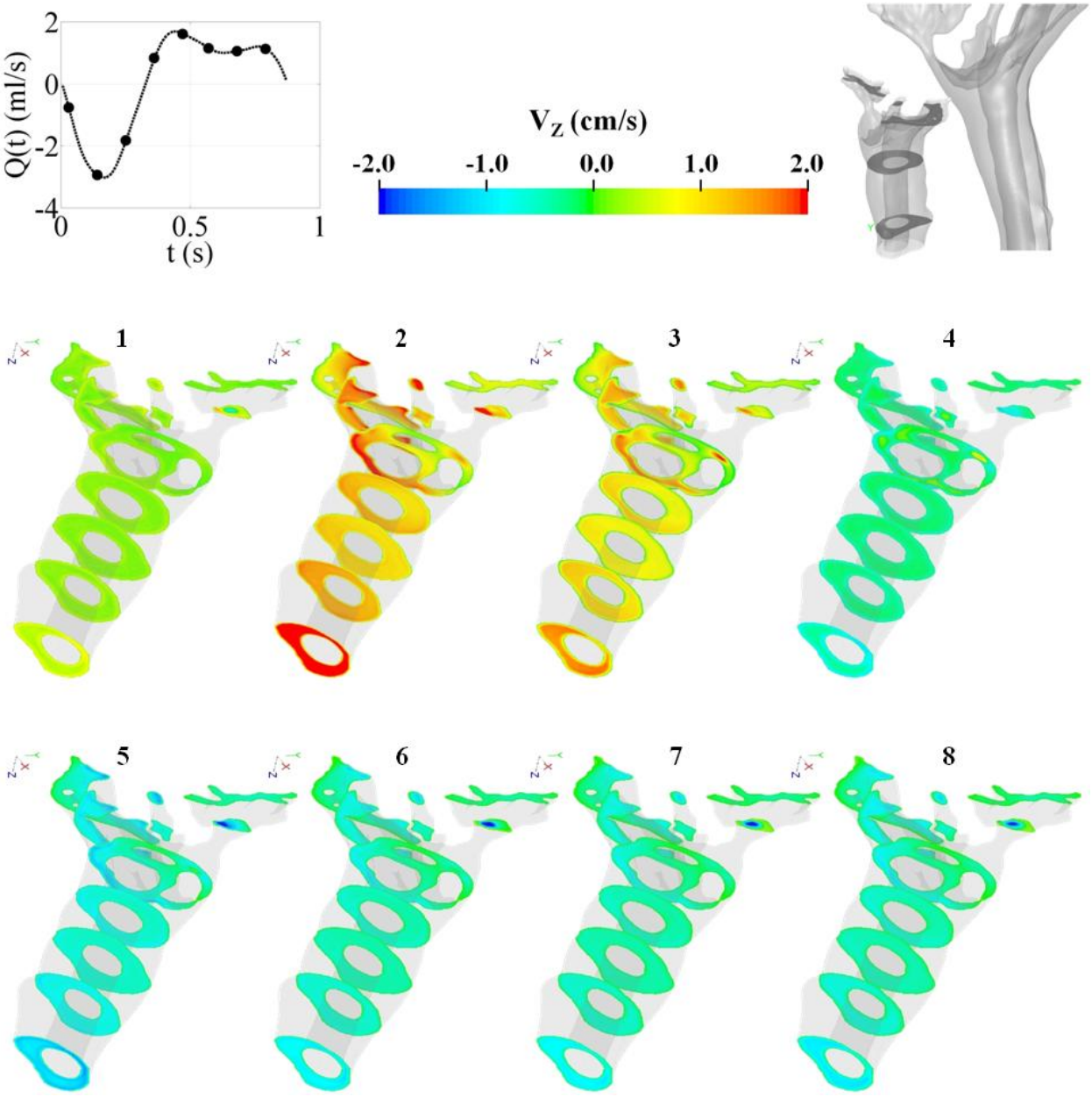

Figure 4.24 Axial velocity (V_Z) contours on multiple axial planes at 8 time points within a cardiac cycle. Velocity range reduced to highlight differences within flow field.

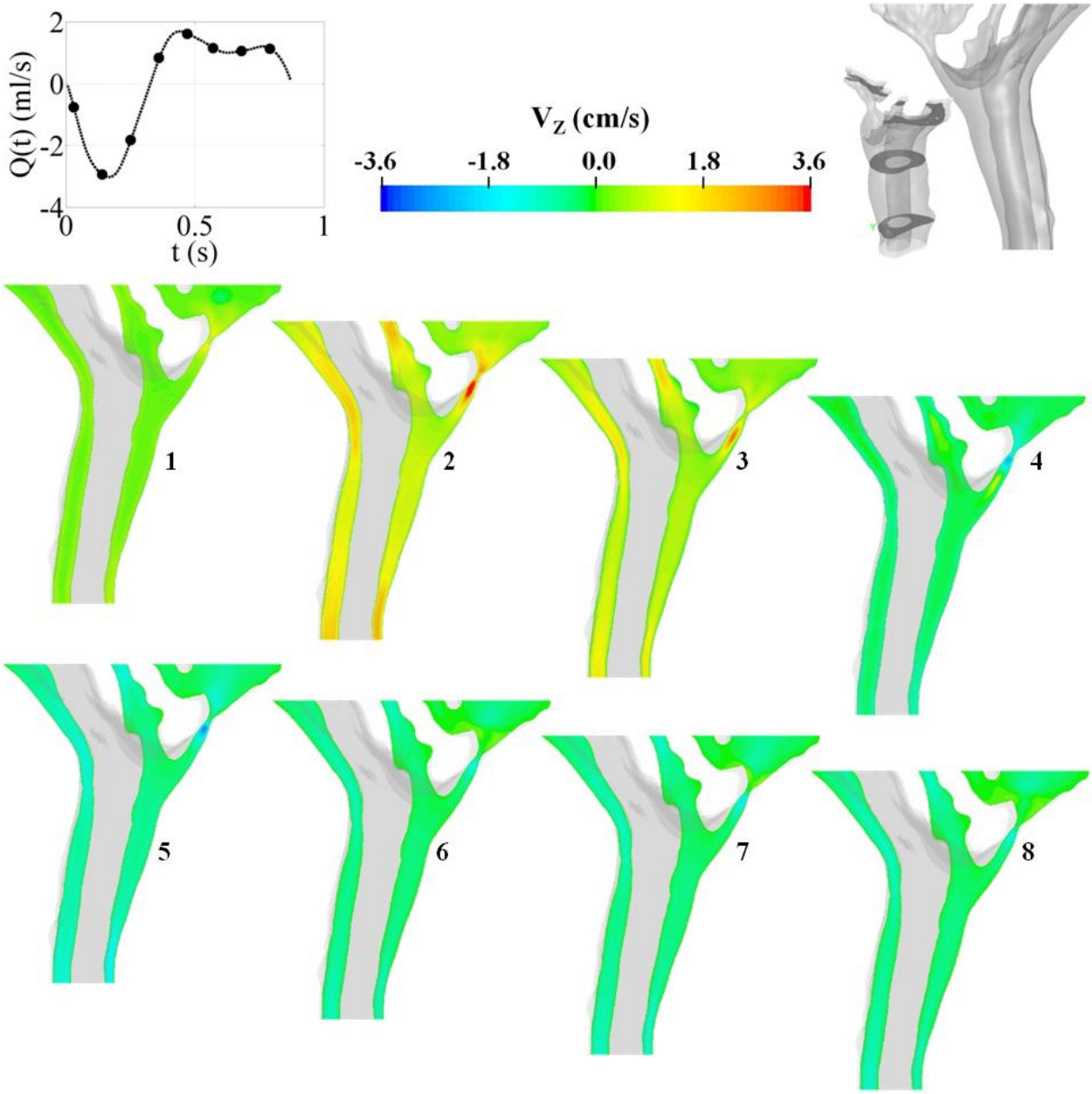

Figure 4.25. Axial velocity (V_Z) contours on mid-sagittal plane at 8 time points within a cardiac cycle.

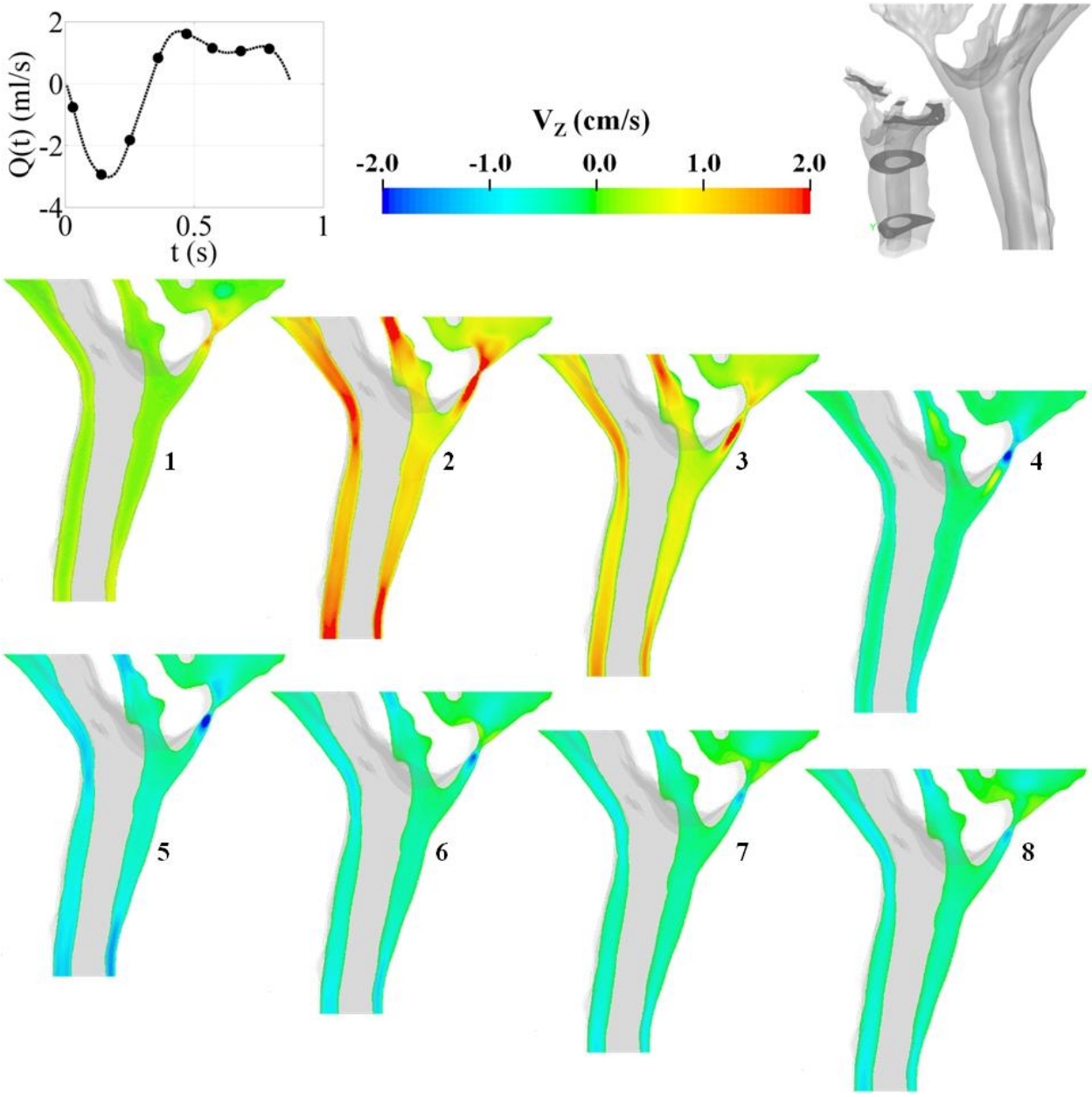

Figure 4.26 Axial velocity (V_Z) contours on mid-sagittal plane at 8 time points within a cardiac cycle. Velocity range reduced to highlight differences within flow field.

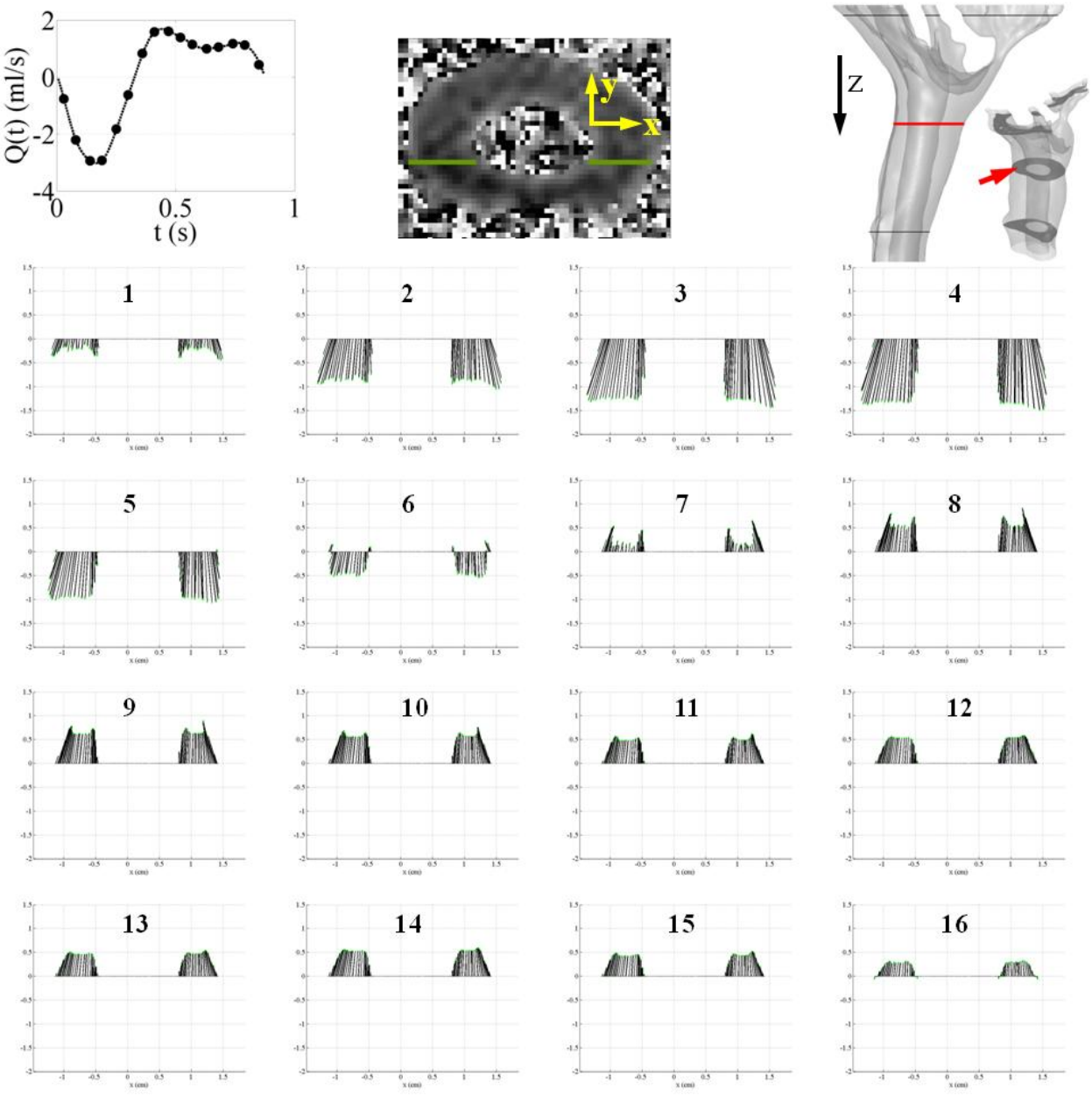

Figure 4.27. Velocity vectors at C2 level on XZ plane at 16 time points within a cardiac cycle.

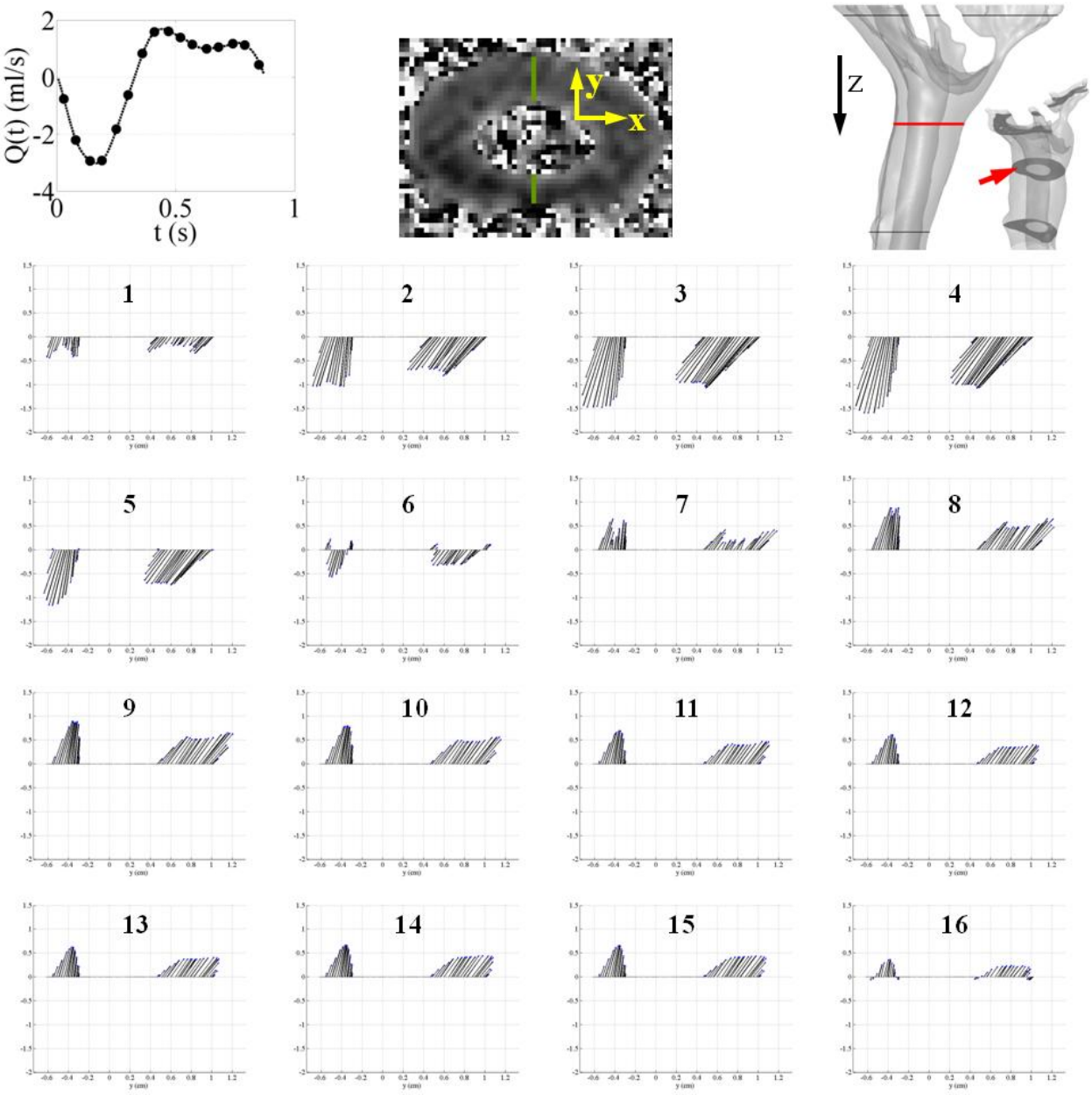

Figure 4.28. Velocity vectors at C2 level on YZ plane at 16 time points within a cardiac cycle.

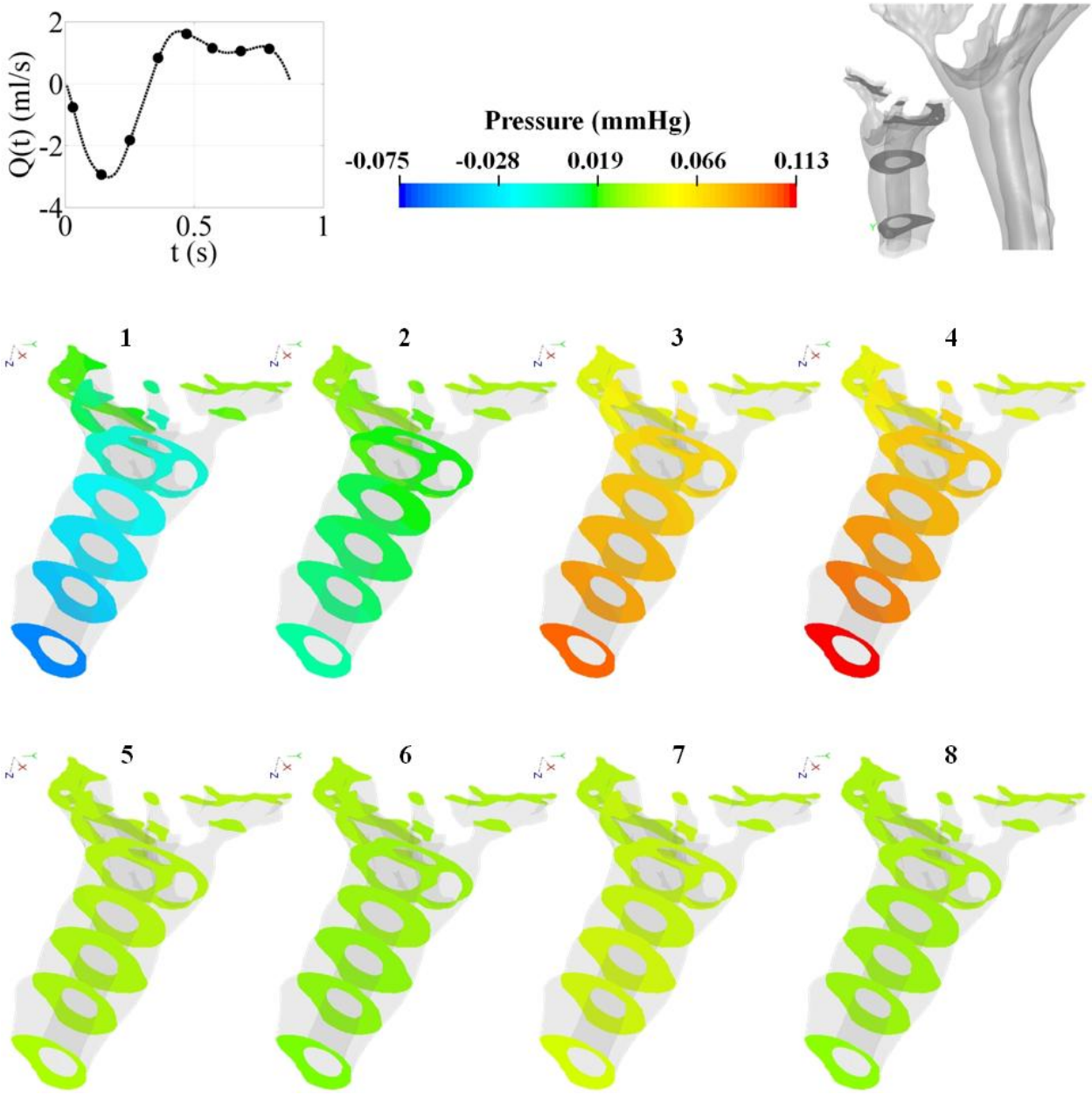

Figure 4.29. Pressure contours on multiple axial planes at 8 time points within a cardiac cycle.

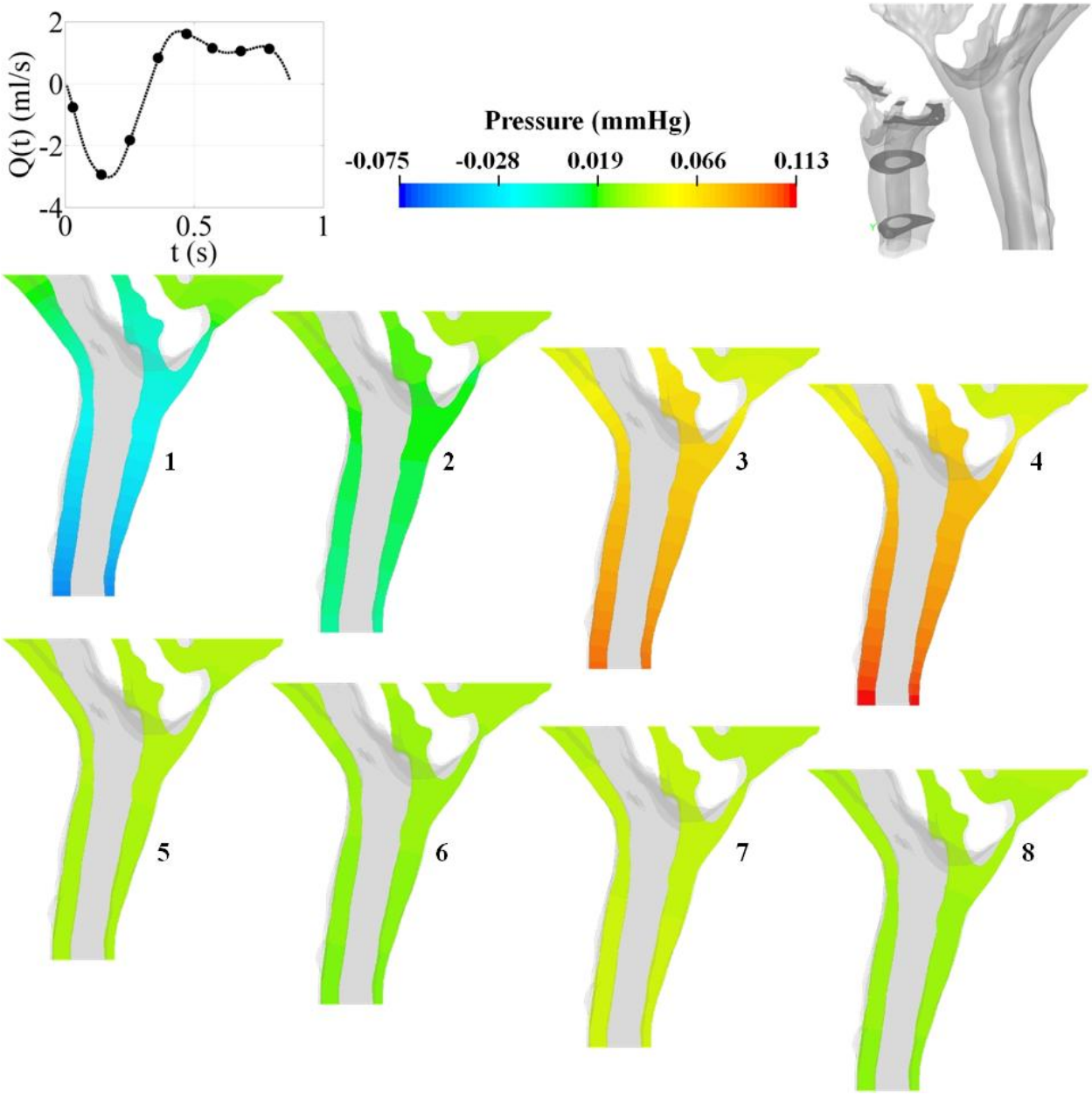

Figure 4.30. Pressure contours on mid-sagittal plane at 8 time points within a cardiac cycle.

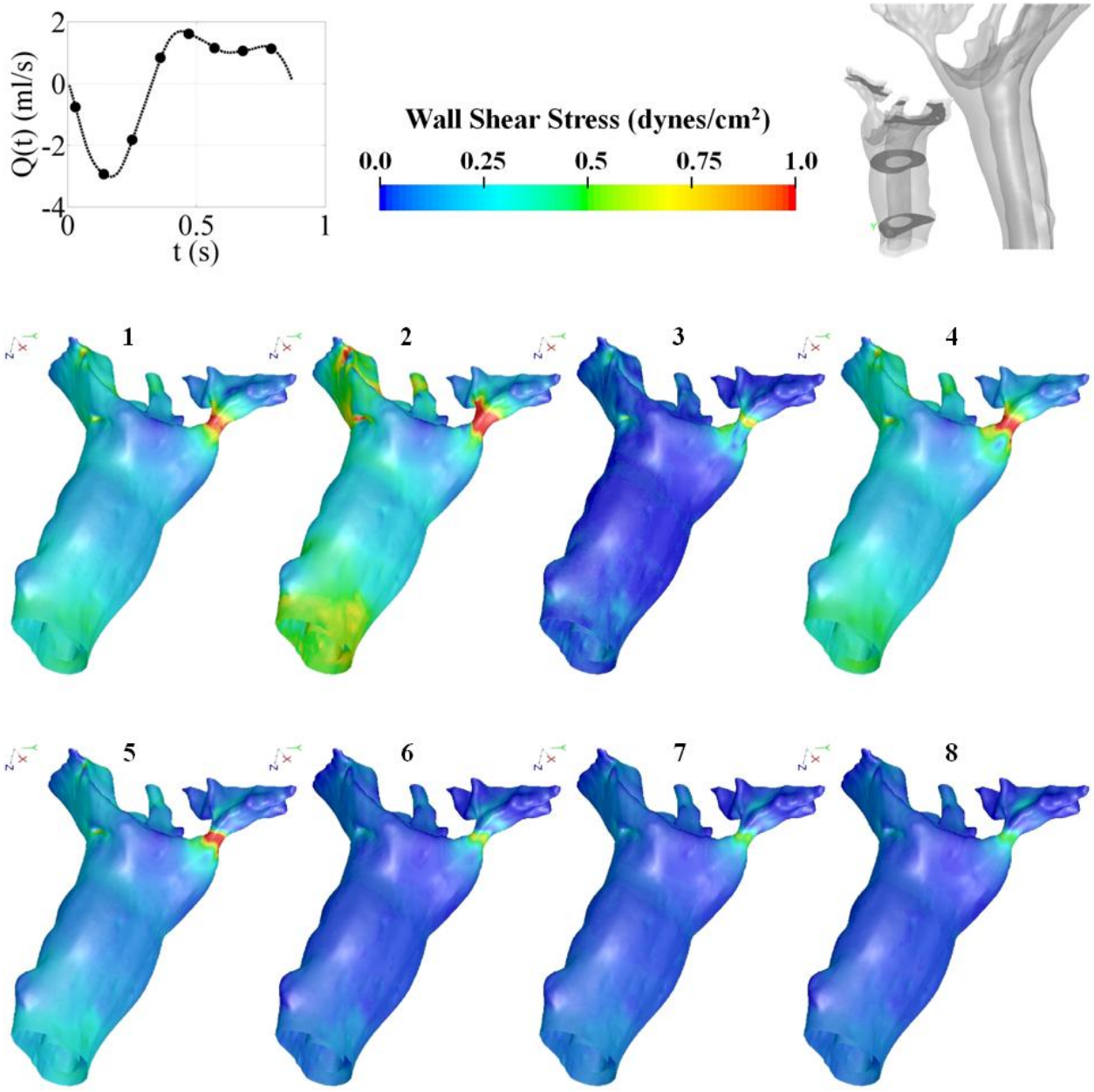

Figure 4.31. 3-D view of WSS contours at 8 time points within a cardiac cycle.

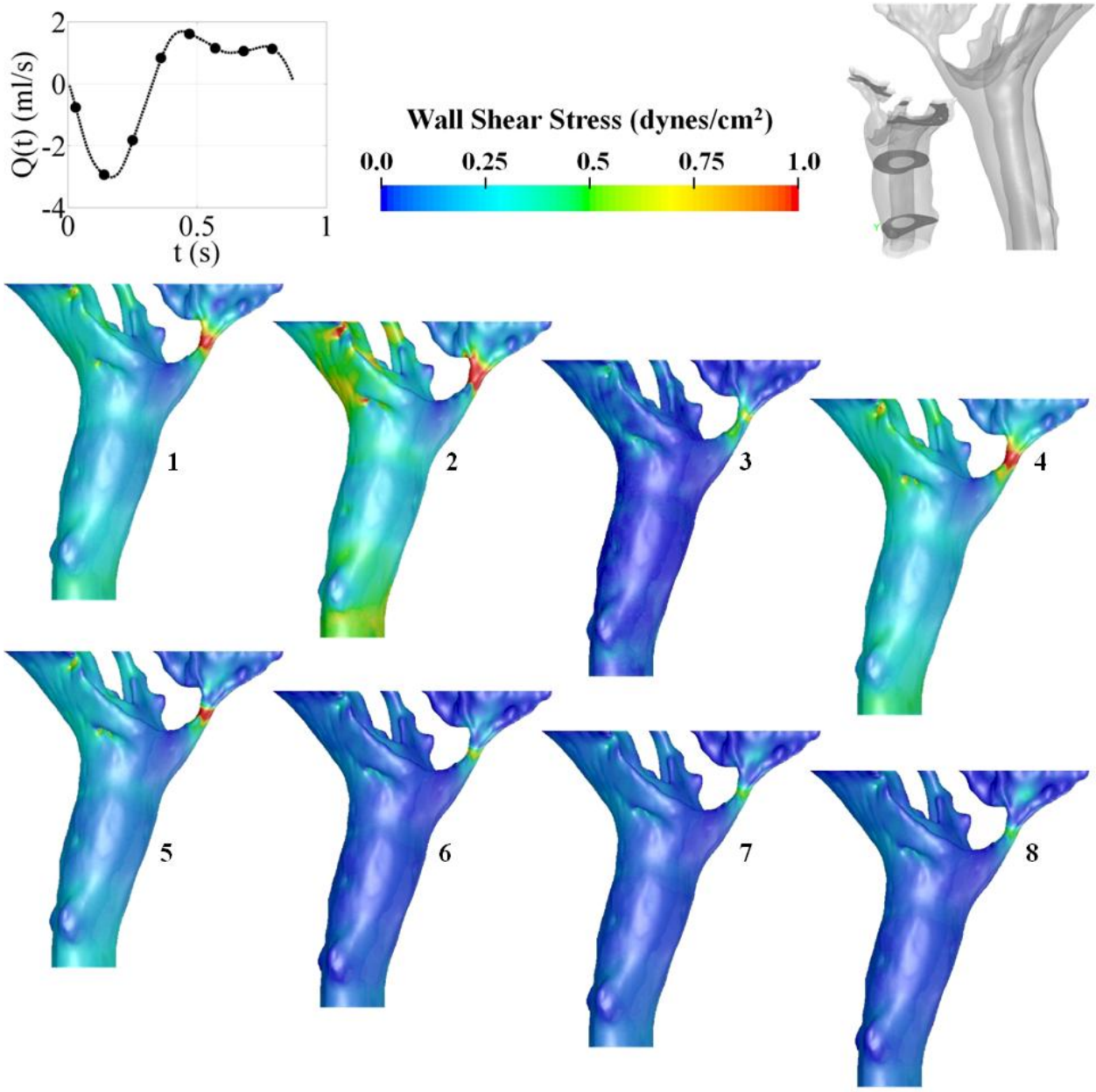

Figure 4.32. Side view of WSS contours at 8 time points within a cardiac cycle.

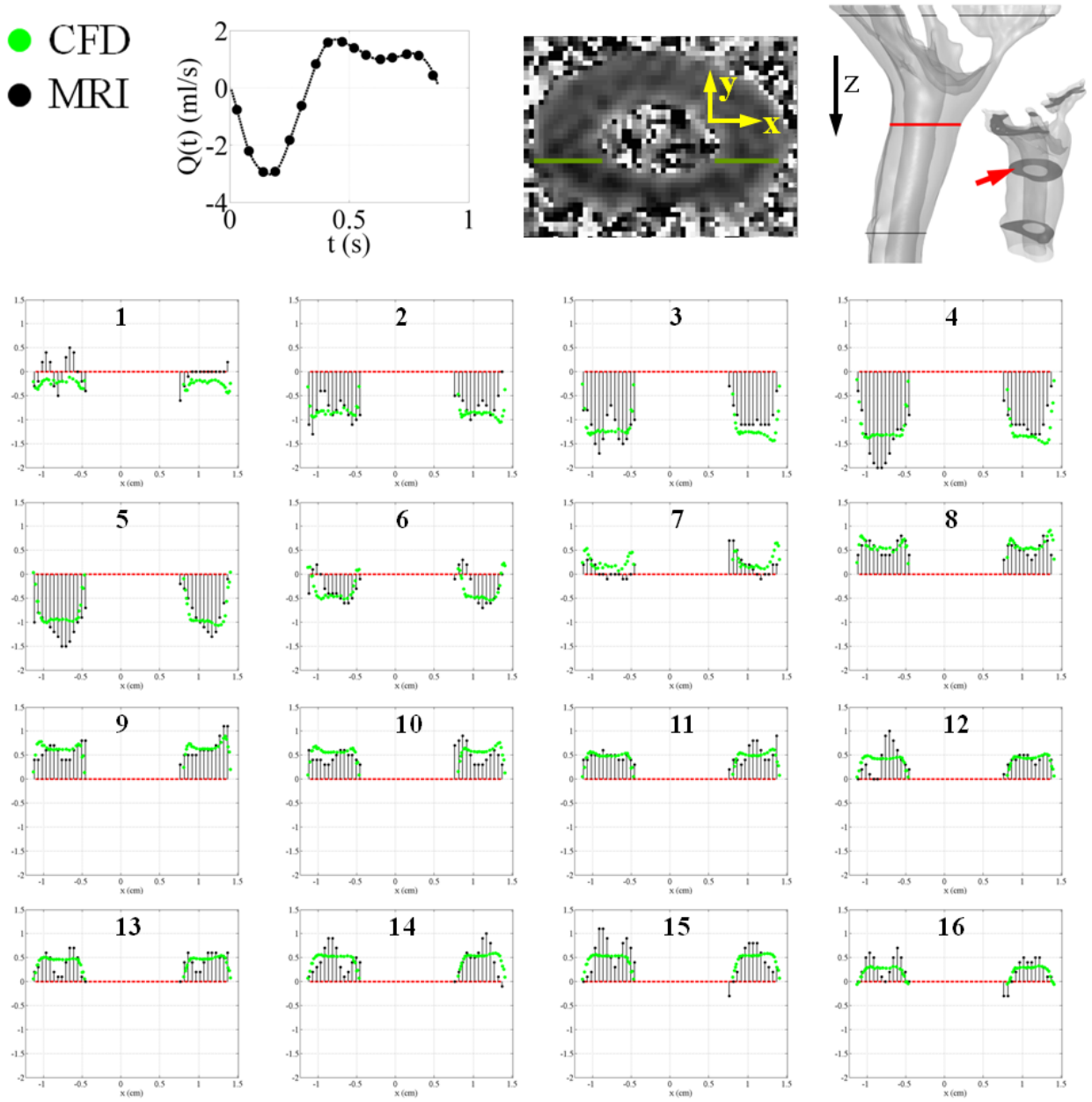

Figure 4.33. CFD Versus Model. Axial velocity at C2 level on XZ plane at 16 time points within a cardiac cycle.

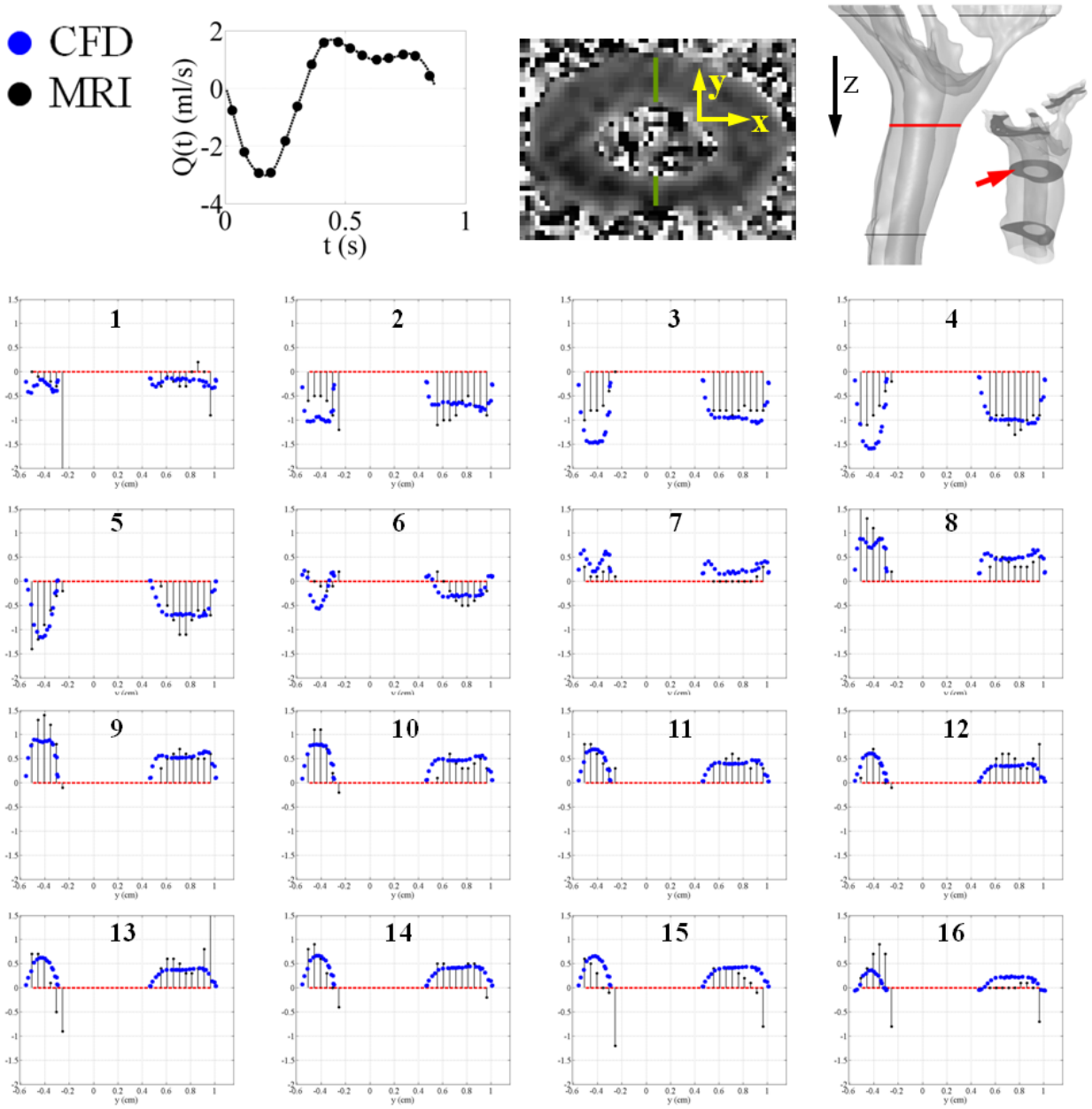

Figure 4.34. CFD Versus Model. Axial velocity at C2 level on YZ plane at 16 time points within a cardiac cycle.

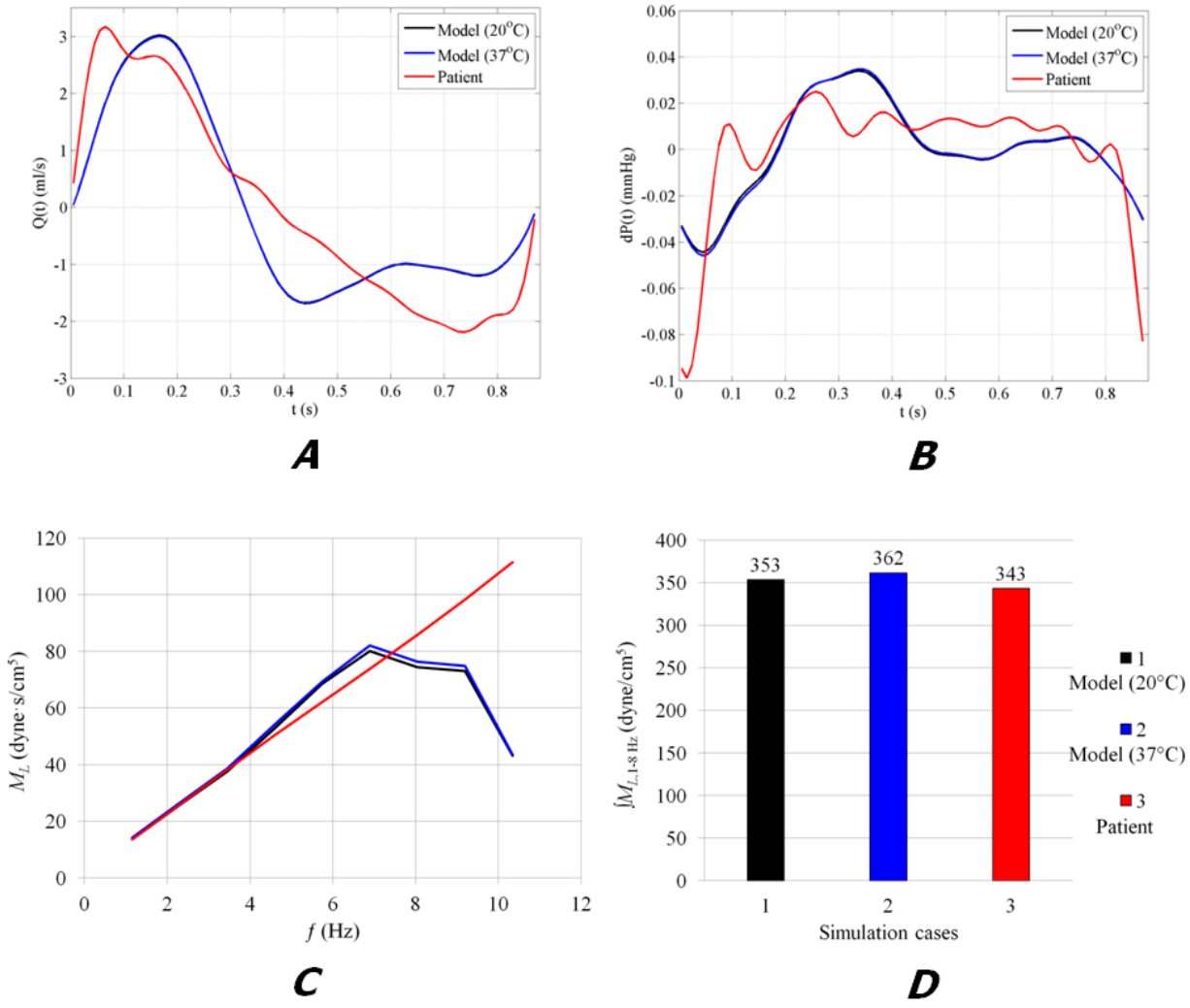

Figure 4.35. Comparison of pressure drop and resistance results for three simulated cases: **A.** Flow waveforms, **B.** Pressure drop across C2 and 25 mm above C2 level, **C.** Resulting longitudinal impedance, **D.** Integrated modulus of longitudinal impedance in 1-8 Hz range.

5. VELOCITY WAVE SPEED IN CERVICAL SAS

A specialized technique to measure the wave speed velocity in the cervical SAS was developed as part of this dissertation work. This work was published in 2009 and has already been cited ten times according to Google scholar (3/15/2012). This work is described here in this chapter with text and figures coming from the 2009 paper by Kalata et al. [51].

5.1 Introduction

The pulse wave velocity (PWV) in a compliant vessel increases as wall stiffness increases, and has been of interest since arterial stiffness is thought to be a risk factor for arterial disease [52]. Craniospinal disorders, such as CM and SM are thought to be linked with overall CSF system compliance as well, hence, PWV measurements were conducted by various investigators [25, 47, 53, 54]. *In-vivo* PWV has been quantified through invasive measurement of pressure in the CSF system [53]. However, researchers have found it difficult to obtain CSF PWV non-invasively due to a lack of accessibility through the skull and spinal vertebrae.

MRI has been employed to measure PWV in various parts of the circulatory system including the aorta and other major vessels by comparing the time to peak velocity between two locations along the vessel of interest [55-57]. Fielden et al. detailed a methodology for quantifying aortic pulse wave velocity using cross-correlation on 2-D PCMR velocity data [58]. In addition, a "COMB" excitation can be used and time to onset of displacement can be measured to estimate PWV [59, 60]. These studies have assumed that the PWV and velocity wave speed (VWS) measured by MR are nearly equivalent, which is likely a reasonable assumption in cases where Womersley number is nearly constant along the fluid conduit and the

radial measurement location of the velocity waveform in the vessel is consistent between measurement locations. Recent improvements in MRI and computing technologies have reduced the imaging time interval to values less than 10 ms. Furthermore, in-plane velocity encoding allows continuous sampling of the VWS propagation in both the temporal and spatial domain. This MR technique has been shown to produce a measurement of PWV in the aorta [58]. The present study employs this same MR technique to determine the VWS in the cervical spinal canal.

A number of studies have reported a single value of VWS during the CSF flow cycle. VWS in the CSF was found to be 13.5 m/s by Williams [53], 2.2 to 4 m/s by Carpenter et al. [54], 4 m/s by Greitz [61], and 12.4 m/s by Bertram [60]. In an i*n-vitro* study of SM by Martin et al., the VWS was found to vary during the CSF flow cycle from 2 to 26 m/s [47].

5.2 Methods

5.2.1 MRI Scans

Three subjects have been participating in this study. Two patients were referred for MRI because of unspecified back pain, but without any previously diagnosed craniospinal disorders, and one patient had fused vertebrae. All three patients were undergoing a clinically ordered MRI exam of the spine. Patients were placed supine on a 6-element spin array coil in a Philips Medical Systems 3.0 Tesla Intera MRI scanner. Electrocardiogram (ECG) leads or a peripheral pulse fingertip gating was used to monitor heart rate. After a standard MRI spine exam, including T1 and T2-weighted sagittal and transverse images, a slice location was identified which passed through the center of the spinal cord and spinal canal in the sagittal plane as shown in Figure 5.1A. At this slice location, an unsteady pcMRI velocity scan was acquired with in-

plane velocity encoding in the foot-head direction at a value of 20 cm/s. Retrospective ECG or peripheral pulse gating was used to reconstruct three cases with 134, 154 and 141 frames, respectively, over the cardiac cycle. The TR for the sequence was 4.4 ms and the TE was 2.4 ms. Slice thickness was 8 mm and in-plane reconstructed pixel sizes were 1.48 x 1.48 and 1.37 x 1.37 mm in case 1 and cases 2 and 3, respectively. Overall scan time was two to three minutes, depending on the heart rate.

5.2.2 Image Processing

Image processing was conducted using MATLAB (MRView and additional set of programs). The distance traveled by the pressure wave in the spinal canal was determined by tracing the path along the mid-line of the anterior SAS as shown in Figure 5.1B. Axial velocity information was recorded for each chosen pixel in the sagittal plane. The gap at the anterior side of the SAS ranged between two and five pixels. The pixel with the maximum systolic velocity was selected at each axial position to minimize wall boundary noise. This was generally near the center of the gap. It is important to select the pixels near the center of the gap since a phase shift can occur for velocity traces at different distances from the wall. This is a well documented phenomenon for pulsatile (Womersley) flows and would add noise to the calculation of VWS.

5.2.3 2-D Data Smoothing

The velocity waveform of each central pixel for all three cases was extracted for a total of 101, 106 and 124 vertical pixels, each having high temporal resolution with 6.7, 5.6 and 6.0 ms time intervals respectively. Time points of maximum velocity (peak systole), minimum velocity (peak diastole), maximum gradient (systolic acceleration), and minimum gradient (systolic

deceleration), were obtained. At each location, the velocity gradient throughout the cardiac cycle was based on slopes of lines fitted to an 11-time point window obtained at each time point, which could be considered as a "running" averaging method. The 11-point line was a fit obtained with linear least squares regression. The time of each computed gradient was considered to be that at the midpoint of the 11 time-point window. Additional filtering methods such as FFT and "hybrid median" were used but without clear benefits over the "running" averaging method.

Time point of maximum acceleration and deceleration along the spinal canal was determined, and a linear regression was then performed on the time points versus position. The distance the velocity wave traveled divided by the time delay, represented by the slope of this linear fit, was assumed to be representative of the VWS at this time point in the cardiac cycle. Slope values that had a p-value less that 0.05 were considered to be statistically significant. A linear fit may not be the best technique to compute VWS since it may vary along the spinal SAS due to compliance changes. Several other curve fit techniques were examined. However, the linear fit produced the lowest overall p-values for the three cases.

5.3 Results

Figure 5.2A-C shows the raw MR velocity data for each volunteer as a function of time and position. Axial position is indicated in Figure 5.1 and begins at the base of the brain and extended caudally. Velocity is indicated by the gray scale, white and black representing velocity in the caudal (towards feet) and cranial (towards head) directions, respectively. Gray represents zero velocity.

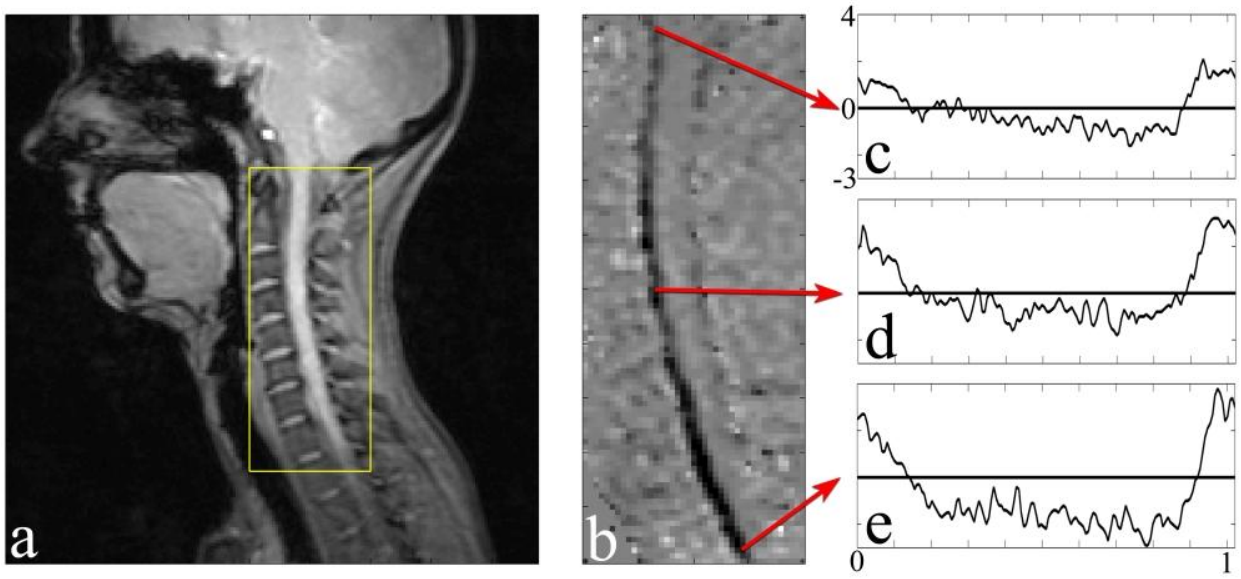

Figure 5.1. Position reference for measurements **A.** Sagittal geometry image with region of interest, **B.** Velocity image with position reference for velocity traces during the cardiac cycle, and **C-E.** Velocity traces during the cardiac cycle at various positions

An increasing time delay for the velocity front is observed for each case. Correspondingly, a decreasing time delay for the minimum velocity was observed for each case. VWS was computed as the slope of a linear fit for both the maximum and minimum velocity time points, which correspond to systole and diastole. The VWS was 12.7 and 7.2 m/s (standard deviation 13 and 4 m/s) during systole and diastole, respectively. Only two (Figures 5.2A and 5.2B) of the three cases were statistically significant ($p<0.05$) for the systolic VWS, and none were statistically significant for diastole. Thus, the maximum and minimum velocity time points did not provide a good measure of VWS using linear regression.

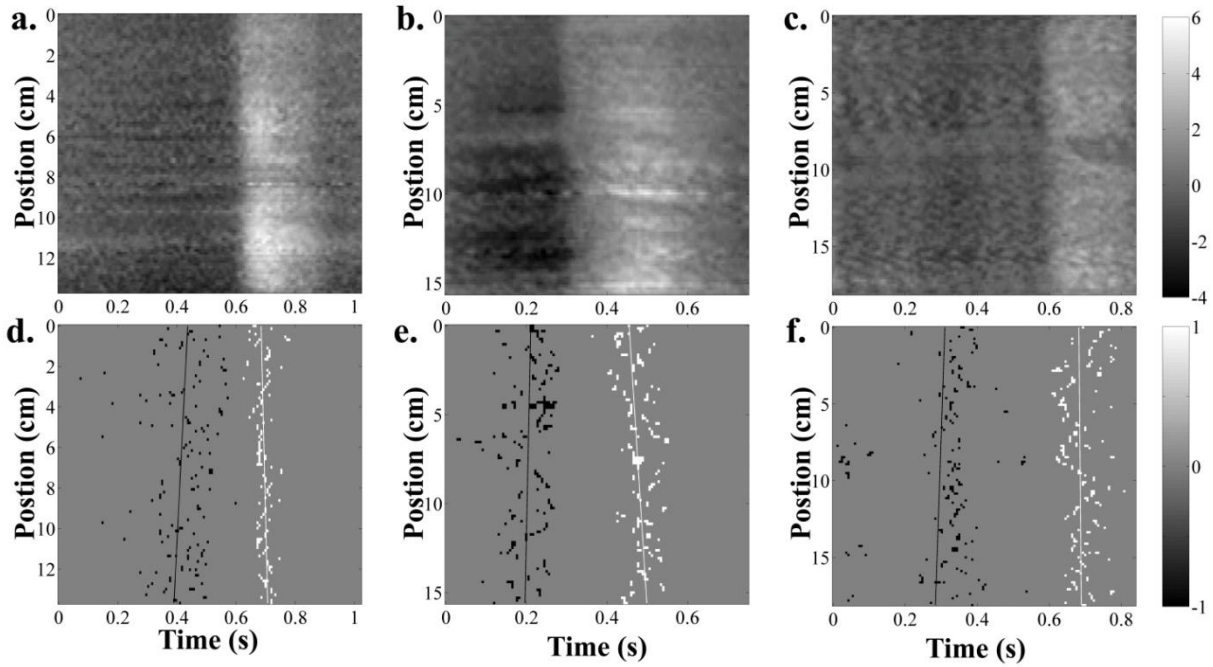

Figure 5.2. Velocity data, **A-C.** Raw velocity data for three patients along centerline of the anterior gap in the spinal canal indicated in Fig. 1, Velocity scale indicated in cm/s. **D-C.** Peak systolic acceleration (white) and deceleration (black) mappings with a linear fit (d-f).

Figure 5.3A-C shows the velocity temporal gradient for each patient as a function of time and position for the velocity data in Fig. 5.2A-C. Similar to the velocity plots, the velocity gradient magnitude is indicated by the grayscale, white and black representing acceleration and deceleration during the cardiac cycle. A second series of plots identify the time points at maximum acceleration and maximum deceleration during the systole Fig. 5.3D-F. VWS was computed as the slope of a linear fit for both the maximum and minimum velocity gradient time points, which correspond to systolic acceleration and deceleration. VWS was 4.6 and 10.6 m/s (standard deviation 1.7 and 11.1 m/s) during systole and diastole, respectively. Assuming a linear fit for the data, all acceleration VWS values were statistically significant (average R^2=0.244, standard deviation 0.126, $p<0.005$) while none of the deceleration VWS values were shown to be statistically significant (Table VII).

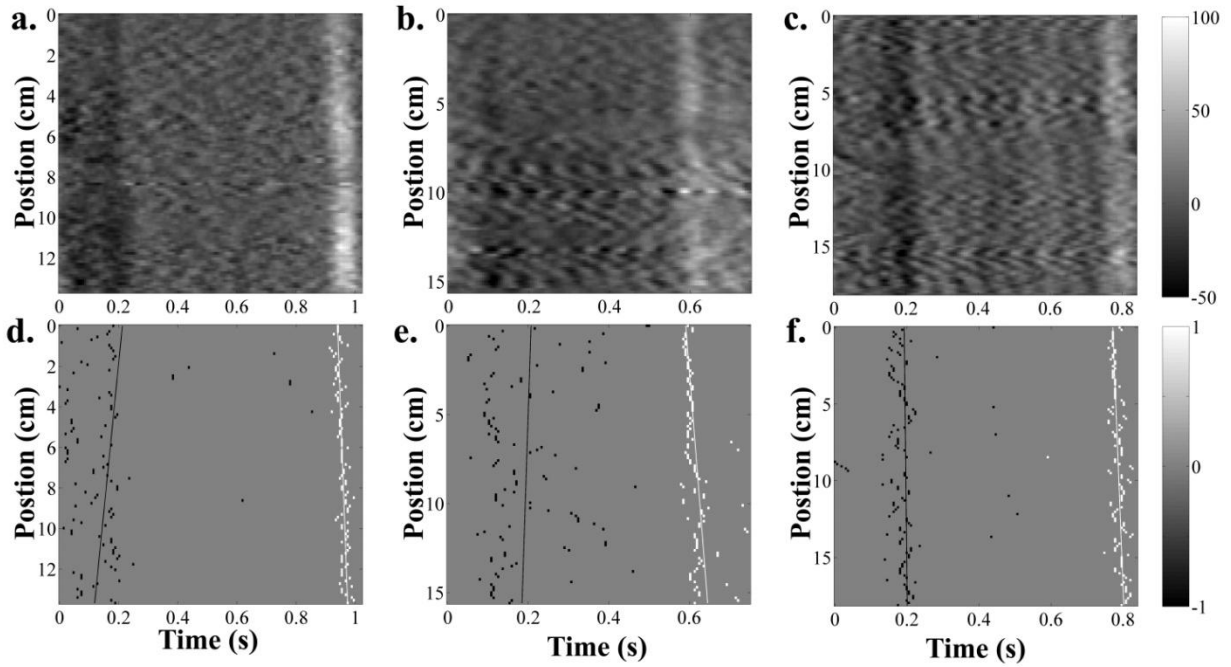

Figure 5.3. Velocity gradient data, **A-C.** Velocity temporal gradient based on the velocity data for three patients in Fig. 2. Velocity gradient scale indicated in mm/s^2, **D-F.** Peak systolic acceleration (white) and deceleration (black) mappings with a linear fit and their scale.

The coefficient of determination (R^2) and p-value were calculated based on a linear least squares regression fit for each data set. These values were computed using MATLAB software with a function called mregress.m written by G.A. Reina (The Neurosciences Institute). The results for all cases are detailed in Table VII in which it is clear that only the maximum velocity gradient, corresponding to systole, produce statistically significant values of VWS.

5.4 Discussion

VWS was computed for the pressure wave originating in the cranial compartment during the cardiac cycle. The slope of the peak velocity measurements during systole was positive indicating that the wave was traveling caudally. This is the expected velocity wave direction since the CSF is moving caudally during systole, i.e. towards the tailbone. During diastole, the flow is reversed and the pressure in the CSF system of the spine is lower.

TABLE VII.

CSF VWS IN THE SPINAL CANAL COMPUTED FROM THE VELOCITY METHOD AND PEAK GRADIENT OF THE VELOCITY. R^2 AND P-VALUES BASED ON LINEAR REGRESSION OF PEAK VELOCITY AND VELOCITY GRADIENT DATA.

	CSF VWS (m/s) **Linear regression R^2 [P-value]**			
	Peak Velocity		**Peak Systole Velocity Gradient**	
Case	**Systolic**	**Diastolic**	**Acceleration**	**Deceleration**
1	6.9 0.0628 [p<0.05]	3.2 0.0183 [NS]	4.4 0.3815 [p<0.005]	1.6 0.0307 [NS]
2	3.7 0.1345 [p<0.005]	11.2 0.0080 [NS]	3.0 0.2179 [p<0.005]	77.2 0.0039 [NS]
3	27.7 0.0025 [NS]	7.2 0.0049 [NS]	6.3 0.1329 [p<0.005]	23.0 0.0011 [NS]
Ave.±Std.Dev.	12.7±13.0	7.2±4.0	4.6±1.7	10.6±11.1

Due to the non-linear stiffening properties of the spinal tissues, the transient state of lower pressure results in a higher system compliance during diastole which manifests itself in a lower wave speed through the system. However, the results during diastole in this study were not statistically significant and thus, we cannot confirm VWS variation during cardiac cycle. Statistically significant data was only obtained for the wave traveling caudally using the maximum velocity gradient (during systole) as a time point marker.

Estimates of the VWS in the spinal SAS are few and the reported values vary significantly (Table VIII). The first measurement of wave speed was by Williams in 1976 via direct puncture in to the lumbar and cervical spinal canal [53].

TABLE VIII.

SUMMARY OF WAVE SPEED MEASUREMENTS IN THE SPINAL SAS.

Researcher	Year	Wave Speed (m/s)	Technique
Williams [53]	1976	13.5	Pressure measurement in lumbar and cisternal CSF during cough
Greitz et al. [25]	1999	4.0	MR velocity measurement
Carpenter et al. [54]	2003	4.0	Theoretical model
Bertram et al. [60]	2005	12.2	Computational model
Martin et al. [47]	2005	2-26	Compliant *in-vitro* SM model
Present Study (Kalata et al [51])	2008	4.6	*In-vivo* cine MR using maximum velocity gradient

Phase lag was recorded after the subject was asked to cough obtaining an approximate wave speed of 13 m/s. Carpenter et al. noted that the pressure pulse likely originated between the lumbar and cisternal regions, which means the assumption may not be correct that the wave traveled from the lumbar to cervical region [54]. Thus, the distance traveled was potentially shorter than assumed, which would mean the wave speed was likely smaller than reported, and in Carpenter's assessment, "…the true value lay in the range of 4 to 5 m/s" [54]. This value is in agreement with Carpenter's computed value from numerical simulations. In 2005, Bertram et al. also developed a numerical model of the spinal fluid system and computed wave speed to be approximately 12 m/s [60]. However, Carpenter et al. and Bertram et al. assumed elastic modulus values and dimensions for the various tissues, which will likely have a significant impact on the computed CSF VWS magnitude. Using an in vitro model representative of SM, Martin et al. demonstrated a variation in wave speed through the cardiac cycle (2 – 26 m/s) [47].

Because of the linear stiffening of the physical model's spinal cord, this VWS variation during the CSF flow cycle could be different in vivo. This study computed the wave speed within a model of the spinal SAS in a two part experiment. First, MR was used to measure velocity and compute the flow waveform in the model. In a separate experiment, unsteady pressure measurements were obtained in the same model in the laboratory. These values were then used to compute the wave speed using a modified form of the Moens-Korteweg equation. In 1999, Greitz et al. reported the CSF VWS of approximately 4 m/s [25]. This value matches the values from the numerical studies [54, 60]; however, details of how Greitz et al. obtained this value are not fully explained.

Thus, the paucity of in vivo VWS measurements in the spinal CSF space is indicative of the difficulty of this measurement. Numerical models can provide estimates of wave speed; however, the difficulty of determining tissue elasticity properties as well as accurate dimensions diminishes the reliability of these estimates. The in vitro study by Martin et al. was performed on a simplified flow model rather than a patient, which puts the VWS values in question.

This novel MR methodology with in-plane velocity encoding provides sufficient spatial and temporal resolution for CSF axial velocity such that the VWS can be detected by tracking the peak velocity gradient during systolic acceleration. The statistically significant values of VWS are similar in magnitude to previously published values. The MR method and image processing techniques could easily be incorporated into clinical protocols if found to have clinical relevance. For example, large values of VWS may provide an indication of elevated intracranial pressure. CMI may produce an altered pressure environment that is detectable by this methodology as well. Further research is necessary to determine the accuracy of this method

using in vitro models, possible accelerations of image acquisition, and the clinical importance of VWS in the spinal SAS and its relation to PWV.

It should be noted that one subject (Figures. 5.2C and 5.3C) had two disks that completely blocked CSF flow on the anterior side. In addition, there appeared to be artifacts due to subject motion during the MR scan. Despite these complications, the velocity gradient method obtained a value of VWS for this subject. This may indicate robustness of the VWS measurement. However, a large sample population and *in-vitro* validation will be required to accurately determine the efficacy of this methodology. In addition, the data processing technique could be improved through optimization of correlation parameters.

In Kalata's work [1], a healthy volunteer case had a pcMRI scan performed at multiple cross-sections throughout the spine (Figure 3.14). These were done 18 cm apart. There was large compliance observed at the upper spine portion. At the lower back region, the compliance was not as noticeable. Interestingly, from these measurements, it was possible to obtain an approximate velocity wave speed (VWS) between the C2 level and "S15" level, which was 36 cm from the C2 level. The phase shift at the Q=0 was ~90 ms. This yielded VWS value of 4 m/s, which is in range of values at systole acceleration portion of velocity waveform.

5.5 Conclusions

This chapter presents a technique to determine *in-vivo* CSF VWS, a potentially clinically useful parameter, to help understand the biomechanical environment of the spinal SAS. The methodology requires verification through phantom model studies and optimization of data processing. Nonetheless, the technique shows good promise as it provides robustness, since it factors in many axial positions along the spinal canal.

6. GENERAL DISCUSSION AND CONCLUSIONS

6.1 Summary

Every aspect of this work originated from measurements of anatomy MRI (SAS geometry) and pcMRI (CSF velocity). Chapters 2-5 describe the work to examine the hydrodynamics of CM patients using various methods such as statistical methods, numerical simulation, physical modeling, and image processing. All these methods require the initial input of data from MRI scans. Some of the MRI data used in this work is already incorporated into clinical protocols. However, high resolution geometry scans, axial pcMR, and the high frequency MRI for VWS are rarely incorporated in clinical scans.

Chapter 2 described methods to calculate unsteady resistance via 3D CFD and 1-D methods: Womersley flow and UAF. For each method, M_L was computed to compare the five cases. Each case had different SAS geometry and CSF flow waveform at C2 as an input condition. The subjects were one healthy volunteer and two patients before and after decompression surgery. As expected, the resistance was the lowest for the healthy volunteer. For both patients, the flow resistance was reduced after the surgery, although it was not reduced to the healthy level. More rapid 1-D methods showed similar M_L values and reduction trends as the 3D CFD. Additionally, a representative form of the Womersly number for each case was correlated with respective M_L values and showed similar reduction trends. Figure 6.1 briefly describes the degree of complexity, accuracy, and time for each solution method.

Chapter 3 investigated the features of CSF flow waveforms that were categorized between healthy volunteers (n=6) and pre-surgical CM patients (n=7). For comparison of cases with different heart rates, the flow waveforms were normalized by their period. For both the

healthy volunteers and CM patients, representative values of flow peaks and systolic duration percentage were obtained. When compared, volunteers had a shorter systolic phase which is consistent with previous literature. Unlike the systolic flow peaks, the diastolic flow peaks were noticeably different with the diastolic peak higher for patients which accommodated for a shorter duration of diastole. The differences in flow waveform shape between healthy and CM patients were investigated via FFT-coefficient analysis. The coefficients indicated that higher harmonic coefficients were dominant for healthy cases which corresponded to a shorter systole and most of them had a post-systolic peak (double-peak). Also, healthy subjects had a more compliant lower cervical SAS region than the patients as evidenced by higher flow peak differences especially in systole.

Chapter 4 focused on a single CM case. The hydrodynamic environment was investigated in the detailed SAS geometry with severe CM blockage. The problem was approached both experimentally and computationally. The experimental velocities were obtained via pcMRI from a Sylgard CM model cast from a negative model built using a rapid prototyping model. The flow rate computed from MRI experiments was similar to the patient flow magnitudes, but was different with respect to acceleration phases. The CFD computed M_L harmonic based on the experiment's flow waveform was similar to that based on the patient's flow waveform. This confirms that CSF flow resistance is strongly dependent upon SAS geometry in CM patients and less dependent on flow waveform.

Chapter 5 presented a novel technique to calculate VWS in sagittal oriented pcMRI planes which contained high frequency axial velocity. Using custom software, high frequency velocity was obtained at the mid-line of the anterior part of the cervical SAS for three subjects (14-19 cm below cranium). The CSF velocity was examined at four different time points:

systolic peak, diastolic peak, systole acceleration, and systole deceleration. The acceleration was obtained from the velocity data via computing a running average based gradient. To assure the statistical significance of the VWS, the R^2 and p-values were computed from linear regression. For all three subjects, only systole acceleration was statistically significant. The average VWS at systolic acceleration was 4.6 m/s.

A brief summary of the work by chapters is provided in Table IX. It indicates where this work was presented and published. Additionally this work was a basis for a National Institute of Health Grant (Project Number: 1R15NS071455-01) titled "Clinical Utility of MR Based Hydrodynamic Parameters in Chiari Malformation."

6.2 Clinical Relevance

As medical imaging techniques such as MRI, CT, or ultrasound improve, it may be possible to develop valuable new diagnostic techniques for clinical use. Improved treatment options and diagnostic methods are desperately in need for patients with CM and SM. Furthermore, research may be able to provide valuable insight to better understand disease genesis and progression.

General parameters, such as M_L, systole duration, flow based FFT-coefficients, flow difference between two axial locations, and VWS need to be further researched before they can be determined to be clinically useful. All parameters need to be evaluated with a large number of test subjects where statistical significance clearly identifies the differences between healthy subjects and CM patients. Also, there is a question of success of surgery. These parameters need to be closely studied before and after surgery, where the parameter of interest is correlated with severity and the results of surgery which may or may not resolve CM symptoms. There are

cases of asymptomatic CM, where by definition there is a tonsillar blockage but people do not experience symptoms of CM. There may be elevated resistance in these cases, but what about other parameters? In cases that are not clearly different from healthy subjects, more than one parameter should be investigated and cross-correlated. As mentioned in Chapter 1, there are various categories of CM, where some parameters may not be relevant. CM is often associated with SM which brings an additional level of difficulty in assessment of the complex pressure environment within compliant sub-cranial SAS and the syrinx.

Chapter 3 touched upon parameters that can be identified with respect to the healthy subject only. Healthy subjects are essential for comparative analysis. They serve as a baseline reference for any parameter that is investigated. Just like the baseline for a normal range of blood pressure, any of the parameters investigated in this work need to have an established normal range based on healthy volunteers.

As mentioned in Chapter 1, the only treatment that has been shown to resolve CM and SM is by surgical means. Currently, surgery planning is based on evaluation of 2-D anatomy images. 3-D reconstruction of SAS (numerous cases shown in Figure 6.2) and the brain tonsils that obstruct normal CSF flow provides dimensional insight into the complexity of the blockage. With current advancement of visualization hardware and software, the stereoscopic display of 3-D SAS geometries can be further visualized giving a better understanding of the importance of the 3-D structure where stereoscopic visualization utilizes depth perception. Today, these visualization tools are available to anyone.

Surgical planning may also be performed using these hydrodynamic simulation tools. With parametric analysis and 1-D computational methods which were discussed in Chapter 2, simulating flow with virtually modified geometries can be performed quickly. 3-D CFD

simulations for quick assessment of resistance is currently not easily available due to the complexity of the problem and current CFD techniques where meshing and computations still consume a significant amount of time. With an advancement of high performance computing (HPC) where processor (or CPU core) parallelization is utilized, obtaining solutions is achievable but still relatively time-consuming and expensive. As processors and graphics cards that utilize HPC technologies such as CUDA, [62, 63] get faster, we are getting closer to achieve results of full 3-D CFD simulation in a time that is acceptable to clinicians.

6.3 Compliance

In Chapters 3 and 5, compliance of sub-cranial SAS was hinted at. In Chapter 3, CSF flow difference between two axial locations was used as one of the parameters to distinguish healthy cases versus the CM patients. In Chapter 5, VWS was computed from pcMR images. This is also a measure of compliance. Both methods clearly show that cervical SAS is expanding and contracting as CSF flows in during systole and out towards the cranium during diastole. Also, it has been shown by Pujol et al. [24] that in a CM patient's brain tonsils move axially as the brain expands and contracts due to phase change between arterial inflow and venous outflow of blood from intracranial space (Figure 1.4). The question arises: Is the rigid assumption used in M_L calculations valid? Arguably, yes. The anatomy MRI is obtained from static images, which represent averaged pixel intensity. In most of the cases, the SAS is reconstructed from high intensity pixels where CSF moves/resides to provide a subject-specific geometry. Its features define the hydrodynamic predispositions towards developing pathological conditions. With the rigidity assumption it may be difficult or even impossible to develop theories for pathogenesis of CM and SM, but a rigid assumption can be used to

hydrodynamically assess the CM condition or stage of progression and identify parameters that could help the physicians and surgeons make better decisions during their diagnosis and treatment.

6.4 Further Work

This work can be continued in many directions. Based on Chapters 2 and 4, experimental and numerical models can be further refined and even automated. There are many unanswered questions regarding how CM or SM initializes, how it develops, and how can it can prevented. The work ahead must be oriented with a multidisciplinary mindset. Engineers, doctors, programmers and even administrators need to work together to push forward towards more funding for CM/SM research.

There is room for further improvements in physical and computational flow models. In physical modeling, a patient specific geometry of the cranium, brain, and spinal canal could be included to reproduce the geometrical feature in a more complete system. So far, the physical reproductions are rather in pieces of the cranio-spinal system. Compliance adds another dimension of difficulty, where brain pulsations would have to simulate brain volume change due to the phase difference between arterial blood inflow and venous blood outflow. There is promising breakthroughs already. Martin et al. [48] showed that modeling of complianat SAS with SM is possible. Numerical simulation technologies advance along with software and hardware advancements. CFD simulations with millions of cells are common today, therefore, a high degree of anatomical accuracy can be incorporated. Gupta et al. [49] has successfully simulated a CSF flow in the lower cranium and upper spinal canal where CSF flow is complex geometrically, therefore, hydrodynamically as well. Also, with advancements in CFD and HPC

technologies, the fluid-structure interaction (FSI) simulations may become more available as FSI is gaining a lot of interest and the type of simulations presented by Bertram [60] may become more common in the future. It is only matter of time that simulation software, which could handle patient specific compliant SAS, will be available to users without advanced training in CFD and FSI.

6.5 Conclusions

Various parameters were introduced to characterize CSF flow in the spinal canal. Using MRI data both for anatomy and CSF velocity, this work investigated various flow parameters that were distinguished between healthy subjects and the patients with CM. CFD analysis was performed to obtain an unsteady resistance parameter, longitudinal impedance. This parameter indicated that CM patients had higher resistance than healthy subjects. Also, a complex geometry of CM blockage was simulated numerically and experimentally. The Sylgard flow phantom model of CM blockage was built and tested with MRI and compared with accompanying CFD results. A statistical flow waveform analysis was performed on numerous cases of healthy subjects and patients. These parameters have shown patients' altered hydrodynamics with respect to healthy subjects. Additionally, a novel technique was developed to measure the CSF wave speed along the spinal canal for MRI images.

This work was a search for parameters which may have the potential to become additional tools to help physicians and neurosurgeons with the diagnosis and treatment of CM patients. Future clinical studies would be required to determine the underlying relationship between these hydrodynamic parameters and neurological symptoms, radiological severity, and

surgical success. The most significant aspect of this study was to describe the variety and range of CSF hydrodynamics in CM patients with respect to healthy subjects.

TABLE IX.

SUMMARY OF WORK

Chapter Title	MRI Anatomy	pcMRI (Cine MRI)	Methods	Parameters	Comparisons	Conferences Publications
CSF Flow Resistance - CFD Study (Chapter 2)	Simplified to continuous annularity	Flow waveforms	• Hydrodynamic parameters • 1-D methods • CFD • FFT	• Womersly number • Longitudinal impedance	• Healthy vs. CM patients • Before vs. after surgery	• ASME 2001 (Poster)[1] • NHD 2002 (Podium pres.)[a]
CSF Flow - Statistical Approach (Chapter 3)	NA	Flow waveforms	• Basic statistical analysis • Normalization • FFT	• Flow peaks • Systole duration • Flow shape • Axial flow difference	Healthy vs. CM patients	• NHD 2005 (Podium pres.)[a]
CM In-Vitro Model (Chapter 4)	Detailed blockage	Flow waveforms and velocity	• Physical flow model • MRI 3-D velocity • CFD • Validation	• 3-D velocity • Longitudinal impedance	Patient vs. model	• IMECE 2004 (Podium pres.)[b] • **Journal Article, Martin et al. – JBME**[2]
Velocity Wave Speed in Cervical SAS (Chapter 5)	NA	High frequency velocity	• Image processing • Statistical analysis	Velocity wave speed	NA	• BMES 2006 (Podium pres.)[c] • **Journal Article, Kalata et al. – JBME**[3]

[a] Presented by Kalata,
[b] Co-author,
[c] First author

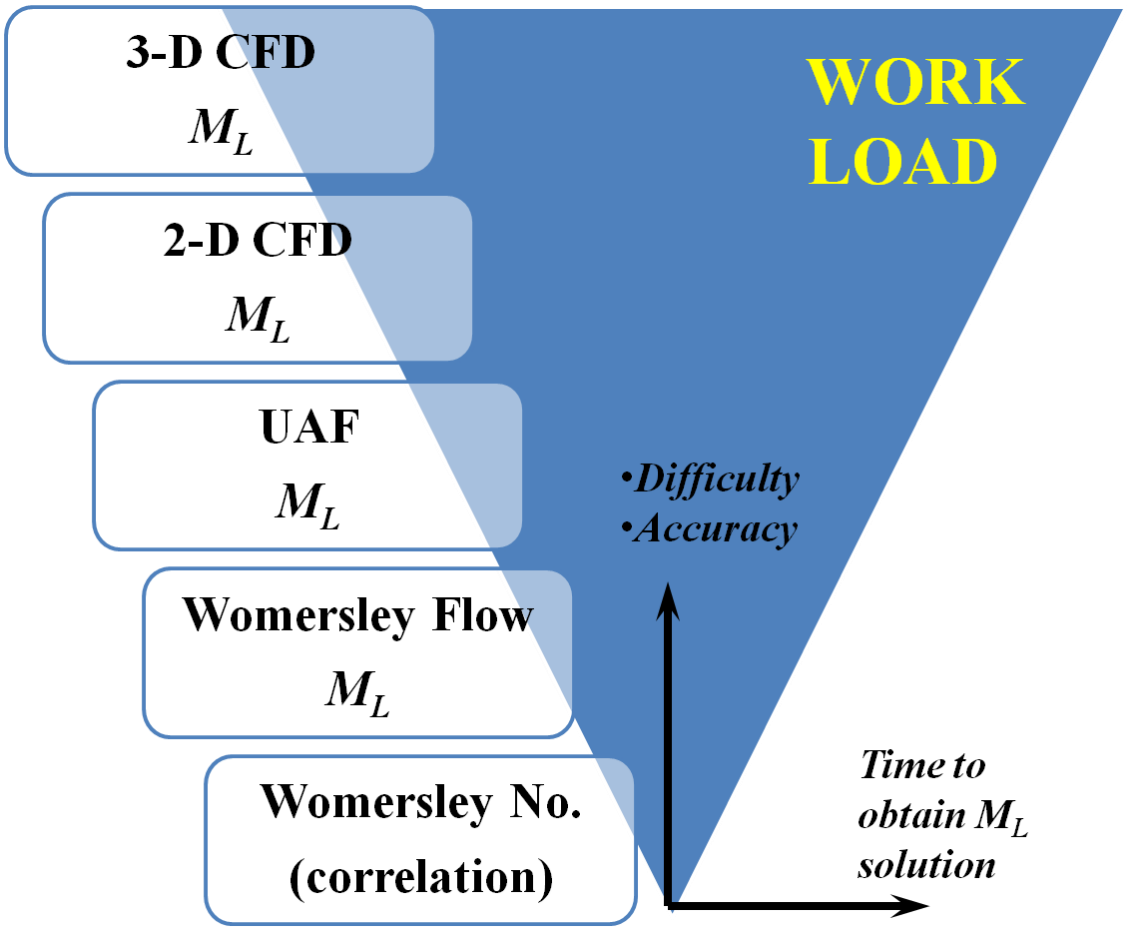

Figure 6.1. Chart describing difficulty levels of methods to compute M_L and their respective accuracy and computational time.

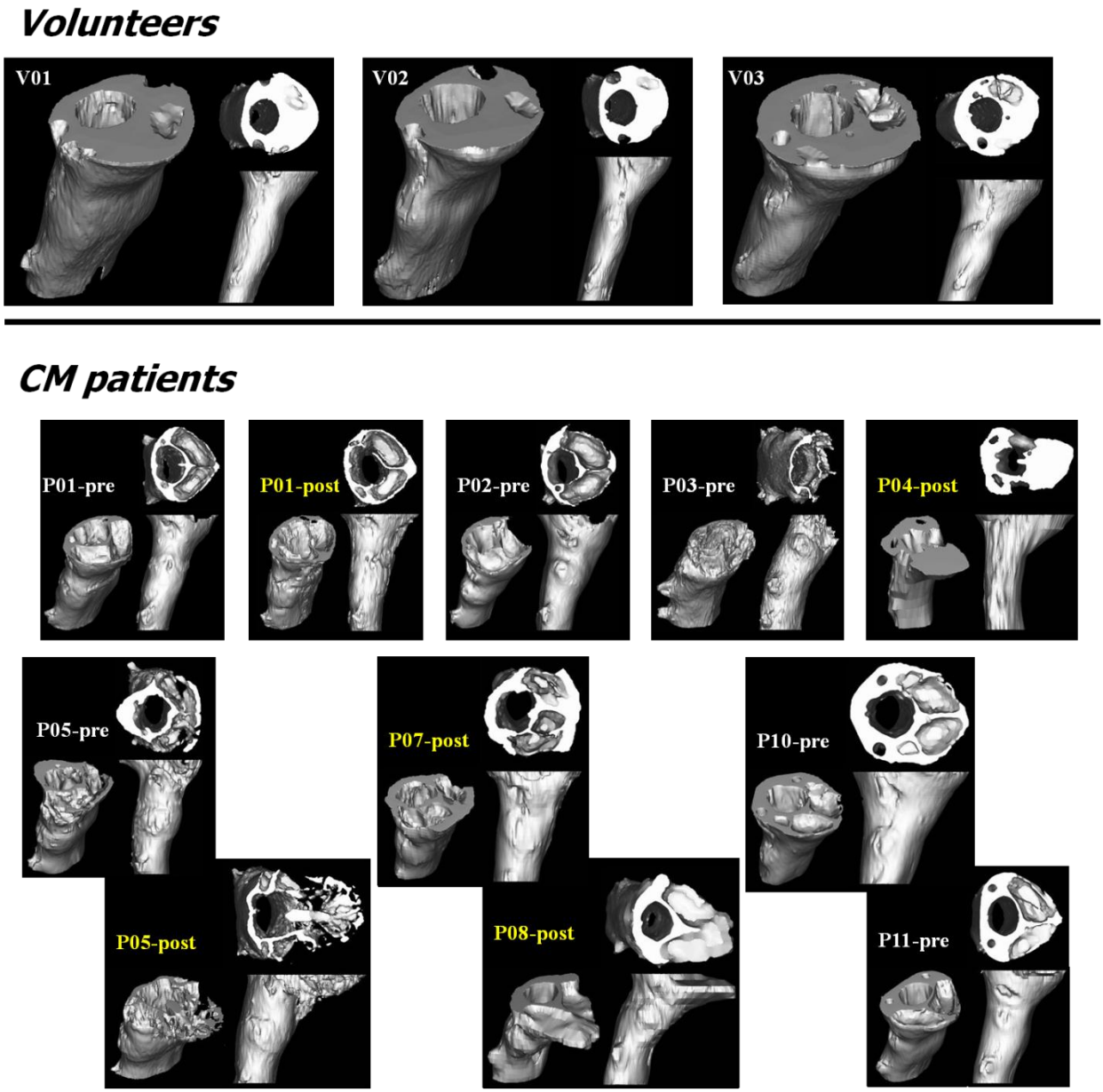

Figure 6.2. 3-D geometries obtained from anatomy MRI: Healthy (top), CM patients (bottom).

CITED LITERATURE

1. Kalata, W.: Numerical Simulation of Cerebrospinal Fluid Motion within the Spinal Canal. Master's thesis, University of Illinois at Chicago, Chicago, 2002

2. Millen, J.W. and Woollam, D.H.M.: *The Anatomy of the Cerebrospinal Fluid.* Oxford Medical Publications, London, Oxford University Press, 1962

3. McConnell, H. and Bianchine, J.: *Cerebrospinal Fluid in Neurology and Psychiatry.* First ed., London, Chapman & Hall Medical, 1994.

4. Fishman, R.A.: *Cerebrospinal Fluid in Diseases of the Nervous System.* 1st ed., Philadelphia, W. B. Sounders Company, 1980.

5. Bloomfield, I.G., Johnston , I.H., and Bilston, L.E.: Effects of proteins, blood cells and glucose on the viscosity of cerebrospinal fluid. *Ped. Neurosurg.*, 28(5): p. 246-51, 1998.

6. Kestin, J., Sokolov, M., and Wakeham, W.A." Viscosity of Liquid Water in the Range -8 Degrees to 150 Degrees Celsius. *Journal of Physical and Chemical Reference Data*, 7(3), 1978.

7. Masserman, J.H.: Cerebrospinal Hydrodynamics: IV. Clinical experimental studies. *Archives of Neurology and Psychiatry*, 32: p. 523-553. 1934.

8. Moufarrij, N. and Awad, I.A.: Classification of the Chiari Malformations and Syringomyelia, in *Syringomyelia and the Chiari Malformations.* Anson, J.A., Benzel, E.C., and Awad, I.A. (eds). The American Association of Neurological Surgeons: Park Ridge. p. 27-34, 1997.

9. Milhorat, T.H., Chou, M.W., Trinidad, E.M., Kula, R.W., Mandell, M., Wolpert, C., and Speer, M.C.:Chiari I malformation redefined: clinical and radiographic findings for 364 symptomatic patients. *Neurosurgery*, 44(5): p. 1005-17, 1999.

10. Ellenbogen, R.G., Rocco, A.A., Shaw, D.W.W., and Winn, R.H.: Toward a rational treatment of Chiari I malformation and syringomyelia. *Neurosurgical Focus*, 8(3): p. Article 6, 2000.

11. Bejjani, G.K.: Definition of the adult Chiari malformation: a brief historical overview. *Neurosurgical Focus*, 11(1): p. Article 1, 2001.

12. Schijman, E.: History, anatomic forms, and pathogenesis of Chiari I malformations. *Childs Nerv Syst*, 20(5): p. 323-8, 2004.

13. Speer, M.: The Prevalence of Syringomyelia in the U.S., in *The Expert Advisor*. American Syringomyelia Alliance Project, Inc.: Longview, TX, 2005.

14. Alzate, J.C., Kothbauer, K.F., Jallo, G.I., and Epstein, F.J.: Treatment of Chiari type I malformation in patients with and without syringomyelia: a consecutive series of 66 cases. *Neurosurgical Focus*, 11(1): p. Article 3, 2001.

15. Alden, T.D., Ojemann, J.G., and Park, T.S.: Surgical treatment of Chiari I malformation: indications and approaches. *Nurosurgical Focus*, 11(1): p. Article 2, 2001.

16. Oldfield, E.H., Muraszko, K., Shawker, T.H., and Patronas N.J.: Pathophysiology of syringomyelia associated with Chiari I malformation of the cerebellar tonsils. Implications for diagnosis and treatment. *J Neurosurg*, 80(1): p. 3-15, 1994.

17. Williams, B.: Management Schemes for Syringomyelia: Surgical Indications and Nonsurgical Management, in *Syringomyelia and the Chiari Malformations*, Anson, J.A., Benzel, E.C., and Awad, I.A. (eds). The American Association of Neurological Surgeons: Park Ridge. p. 125-144,1997.

18. Kern, M.B., and Anson, J.A.: Shunting Procedures for Syringomyelia in Chiari Malformations, in *Syringomyelia and the Chiari Malformations*, Anson, J.A., Benzel, E.C., and Awad, I.A. (eds). The American Association of Neurological Surgeons: Park Ridge. p. 151-158, 1997.

19. Lotbiniere, A.C.d.J.: Historical Considerations, in *Syringomyelia and the Chiari Malformations*, Anson, J.A., Benzel, E.C., and Awad, I.A. (eds). The American Association of Neurological Surgeons: Park Ridge. p. 1-26, 1997.

20. Bergstrand, G., Bergstrom, M., Nordell, B., Stahlberg, F., Ericsson, A., Hemmingsson, A., Sperber, G. Thuomas, K.A., and Jung, B.: Cardiac gated MR imaging of cerebrospinal fluid flow. *J Comput Assist Tomogr*, 9(6): p. 1003-6, 1985.

21. Bradley, W.G.Jr., Kortman, K.E., and Burgoyne, B.: Flowing cerebrospinal fluid in normal and hydrocephalic states: appearance on MR images. *Radiology*,159(3): p. 611-6, 1986.

22. Feinberg, D.A., and Mark, A.S.: Human brain motion and cerebrospinal fluid circulation demonstrated with MR velocity imaging. *Radiology*, 163(3): p. 793-9, 1987.

23. Levy, L.M., and Di Chiro, G.: MR phase imaging and cerebrospinal fluid flow in the head and spine. *Neuroradiology*, 32(5): p. 399-406, 1990.

24. Pujol, J., Roig, C., Capdevila, A., Pou, A., Marti-Vilalta, J.L., Kulisevsky, J., Escartin, A., and Zannoli, G.: Motion of the cerebellar tonsils in Chiari type I malformation studied by cine phase-contrast MRI. *Neurology*, 45(9): p. 1746-53, 1995.

25. Greitz, D., Ericson, K., and Flodmark, O.: Pathogenesis and mechanics of spinal cord cysts: a new hypothesis base in magnetic resonance studies of cerebrospinal fluid dynamics. *International Journal of Neuroradiology*, 5(2): p. 61-78, 1999.

26. Heiss, J.D., Patronas, N., DeVroom, H.L., Shawker, T., Ennis, R., Kammerer, W., Eidsath, A., Talbot, T., Morris, J., Eskioglu, E., and Oldfield, E.H.: Elucidating the pathophysiology of syringomyelia. *J Neurosurg*, 91(4): p. 553-62, 1999.

27. Brugieres, P., Idy-Peretti, I., Iffenecker, C., Parker, F., Jolivet, O., Hurth, M., Gatson, A., and Bittuon, J.: CSF flow measurement in syringomyelia. *AJNR Am J Neuroradiol*, 21(10): p. 1785-92, 2000.

28. Hofmann, E., Warmuth-Metz, M., Bendszus, M., and Solymosi, L.: Phase-contrast MR imaging of the cervical CSF and spinal cord: volumetric motion analysis in patients with Chiari I malformation. *AJNR Am J Neuroradiol*, 21(1): p. 151-8, 2000.

29. Alperin, N., Kulkarni, K., Roitberg, B., Loth, F., Pandian, N.K., Mafee, M.F., Foroohar, M., and Lichtor, T.: Analysis of magnetic resonance imaging - based blood and cerebrospinal fluid flow measurements in patients with Chiari I malformation: a system apprach. *Neurosurgical Focus*, 11(1): p. Article 6, 2001.

30. Haughton, V.M., Korosec, F.R., Medow, J.E., Dolar, M.T., and Iskandar, B.J.: Peak systolic and diastolic CSF velocity in the foramen magnum in adult patients with Chiari I malformations and in normal control participants. *AJNR Am J Neuroradiol*, 24(2): p. 169-76, 2003.

31. Dolar, M.T., Haughton, V.M., Iskandar, B.J., and Quigley, M.: Effect of craniocervical decompression on peak CSF velocities in symptomatic patients with Chiari I malformation. *AJNR Am J Neuroradiol*, 25(1): p. 142-5, 2004.

32. Ethier, C.R., Prakash, S., Steinman, D.A., Leask, R.L., Couch, G.C., and Ojha, M.: Steady flow separation patterns in a 45 degree junction. *J. Fluid Mech.*, 411: p. 1-38. 2000.

33. Moore, J.E., Weydahl, E.S.Jr., and Santamarina, A.: Frequency dependence of dynamic curvature effects on flow through coronary arteries. *J Biomech Eng*, 123(2): p. 129-33. 2001.

34. Perktold, K., Thurner, E., and Kenner, T.: Flow and stress characteristics in rigid walled and compliant carotid artery bifurcation models. *Med Biol Eng Comput*, 32(1): p. 19-26. 1994.

35. Steinman, D.A., Poepping, T.L., Tambasco, M., Rankin, R.N., and Holdsworth, D.W.: Flow patterns at the stenosed carotid bifurcation: effect of concentric versus eccentric stenosis. *Ann Biomed Eng*, 28(4): p. 415-23. 2000.

36. Loth, F., Yardimci, M.A., and Alperin, N.: Hydrodynamic modeling of cerebrospinal fluid motion within the spinal cavity. *J Biomech Eng*, 123(1): p. 71-9, 2001.

37. Ford, M.D., Nikolov., H.N., Milner, J.S., Lownie, S.P., Demont, E.M., Kalata, W., Loth, F., Holdsworth, D.W., and Steinman, D.A.: PIV-measured versus CFD-predicted flow

dynamics in anatomically realistic cerebral aneurysm models. *J Biomech Eng*, 130(2): p. 021015, 2008.

38. Lei, M., Giddens. D.P., Jones, S.A., Loth, F., and Bassiouny, H.: Pulsatile flow in an end-to-side vascular graft model: comparison of computations with experimental data. *J Biomech Eng*, 123(1): p. 80-7, 2001.

39. Yedavalli, R.V., Loth,. F., Yardimci, M.A., Prichard, W.F., Oshinski, J.N., Sadler, F., Charbel, F.T., and Alperin, N.:Construction of a physical model of the human carotid artery based upon In vivo magnetic resonance images. *J Biomech Eng*, 123: p. 372-376, 2001.

40. Lee, S.H.: Solution method for transitional flow in the vascular bifurication based on in vivo medical images. Master's thesis, University of Illinois at Chicago, Chicago, 2002.

41. Lee, S.H., Piersol, N.E., Loth, F., Fischer, P.F., Leaf, G., Smith, B., Yedavalli, R.V., Yardimchi, M.A., Alperin, N., and Schwartz, L.B.: Automated Mesh Generation of an Arterial Bifurcation Based upon In Vivo MR Images. in *World Congress on Medical Physics and Bioengineering*. Chicago, IL., 2000.

42. Alperin, N., Vikingstad, E.M., Gomez-Anson, B., and Levin, D.N.: Hemodynamically independent analysis of cerebrospinal fluid and brain motion observed with dynamic phase contrast MRI. *Magn Reson Med*, 35(5): p. 741-54, 1996.

43. Alperin, N.J., Lee, S.H., Loth, F., Raksin, P.B., and Lichtor, T.: MR-Intracranial pressure (ICP): a method to measure intracranial elastance and pressure noninvasively by means of MR imaging: baboon and human study. *Radiology*, 217(3): p. 877-85, 2000.

44. Henry-Feugeas, M.C., Idy-Peretti, I., Baledent, O., Poncelet-Didon, A., Zannoli, G., Bittoun, J., and Schouman-Claeys, E.: Origin of subarachnoid cerebrospinal fluid pulsations: a phase-contrast MR analysis. *Magn Reson Imaging*, 18(4): p. 387-95, 2000.

45. Bhadelia, R.A., Bogdan, A.R., Wolpert, S.M., Lev, S., Appignani, B.A., and Heilman, C.B.: Cerebrospinal fluid flow waveforms: analysis in patients with Chiari I malformation by means of gated phase-contrast MR imaging velocity measurements. *Radiology*, 196(1): p. 195-202, 1995.

46. Gray, H., *Gray's Anatomy*. 15 ed., New York: Barnes & Noble Books. 1995

47. Martin, B.A., Kalata, W., Loth, F., Royston, T.J., and Oshinski, J.N.: Syringomyelia hydrodynamics: An in vitro study based on in vivo measurements. *J Biomech Eng*, 127(7): p. 1110-1120, 2005.

48. Martin, B.A., and Loth, F.: The influence of coughing on cerebrospinal fluid pressure in an in vitro syringomyelia model with spinal subarachnoid space stenosis. *Cerebrospinal Fluid Res*, 6: p. 17, 2009.

49. Gupta, S., Soellinger, M., Boesinger, P., Poulikakos, D., and Kurtcuoglu, V.: Three-dimensional computational modeling of subject-specific cerebrospinal fluid flow in the subarachnoid space. *J Biomech Eng*, 131(2): p. 021010, 2009

50. Medina, F., Sandoval, H., and Wicker. R.: Building molds with WaterWorks - a process for manufacturing rigid and compliant models. in *Stratasys User Group Conference Proceedings*. Minneapolis, MN, 2002.

51. Kalata, W., Martin, B.A., Oshinski, J.N., Jerosch-Herold, M., Royston, T.J., and Loth, F.: MR measurement of cerebrospinal fluid velocity wave speed in the spinal canal. *IEEE Trans Biomed Eng*, 56(6): p. 1765-8, 2009.

52. Zhang, X. and Greenleaf, J.F.: Noninvasive generation and measurement of propagating waves in arterial walls. *J Acoust Soc Am*, 119(2): p. 1238-43, 2006.

53. Williams, B.: Cerebrospinal fluid pressure changes in response to coughing. *Brain*, 99(2): p. 331-46, 1976.

54. Carpenter, P.W., Berkouk, K., and Lucey, A.D.: Pressure wave propagation in fluid-filled co-axial elastic tubes. Part 2: Mechanisms for the pathogenesis of syringomyelia. *J Biomech Eng*, 125(6): p. 857-63, 2003.

55. Laffon, E., Marthan, R., Montaudon, M., Latrabe, V., Laurent, F., and Ducassou, D.: Feasibility of aortic pulse pressure and pressure wave velocity MRI measurement in young adults. *J Magn Reson Imaging*, 21(1): p. 53-8, 2005.

56. Rogers, W.J., Hu, Y.L., Coast, D., Vido, D.A., Kramer, C.M., Pyeritz, R.E., and Reichek, N.: Age-associated changes in regional aortic pulse wave velocity. *J Am Coll Cardiol*, 38(4): p. 1123-9, 2001.

57. Wiesmann, F., Petersen, S.E., Leeson, P.M., Francis, J.M., Robson, M.D., Wang, Q., Choudhury, R., Channon, K.M., and Neubauer, S.: Global impairment of brachial, carotid, and aortic vascular function in young smokers: direct quantification by high-resolution magnetic resonance imaging. *J Am Coll Cardiol*, 44(10): p. 2056-64, 2004.

58. Fielden, S.W., Fornwalt, B.K., Jerosch-Herold, M., Eisner, R.L., Stillman, A.E., and Oshinski, J.N.: A new method for the determination of aortic pulse wave velocity using cross-correlation on 2D PCMR velocity data. *J Magn Reson Imaging*, 27(6): p. 1382-7, 2008.

59. Tarnawski, M., Cybulski, G., Doorly, D., Dumoulin, C., Darrow, R., and Caro, C.: Noninvasive determination of local wavespeed and distensibility of the femoral artery by comb-excited Fourier velocity-encoded magnetic resonance imaging: measurements on athletic and nonathletic human subjects. *Heart Vessels*, 9(4): p. 194-201, 1994.

60. Bertram, C.D., Brodbelt, A.R., and Stoodley, M.A.: The origins of syringomyelia: Numerical models of fluid/structure interactions in the spinal cord. J *J Biomech Eng*, 2005. 127(7): p. 1099-1109.

61. Greitz, D., Franck, A., and Nordell, B.: On the pulsatile nature of intracranial and spinal CSF-circulation demonstrated by MR imaging. *Acta Radiol*, 34(4): p. 321-8. 1993.

62. Cohen, J.M., and Molemaker, M.J.: A fast double precision CFD code using CUDA. in *Proceedings of Parallel Computational Fluid Dynamics 2009*. 2009.

63. Crespo, A.C., Dominguez, J.M., Barriero, A., Gomez-Gasteira, M., and Rogers, B.D.: GPUs, a new tool of acceleration in CFD: efficiency and reliability on smoothed particle hydrodynamics methods. *PLoS One*, 6(6): p. e20685, 2011.

APPENDIX

A1. 1-D Comutational Methods

A1.1. Unsteady 1-D Solution in Cylindrical Coordinates

The reduced unsteady Navier-Stokes equation is

$$\frac{\partial w}{\partial t} = -\frac{1}{r}\frac{\partial p}{\partial z} + \nu\left\{\frac{\partial w^2}{\partial^2 r} + \frac{1}{r}\frac{\partial w}{\partial r}\right\} \tag{A1.1}$$

If we assume the pressure gradient as

$$\frac{\partial p}{\partial z} = Ae^{i\omega t} \tag{A1.2}$$

And also the velocity as

$$w(t,r) = f\left(\frac{r}{R}\right)e^{i\omega t} = f(y)e^{i\omega t} \quad \text{where } y = \frac{r}{R} \tag{A1.3}$$

The above momentum equation is transformed to the following ordinary differential equation

$$f(y)i\omega e^{i\omega t} = -\frac{A}{\rho}e^{i\omega t} + \nu\left\{\frac{1}{R^2}\frac{\partial f^2}{\partial^2 y}e^{i\omega t} + \frac{1}{y}\frac{1}{R^2}\frac{\partial f}{\partial y}e^{i\omega t}\right\} \tag{A1.4}$$

$$f(y)i\omega = -\frac{A}{\rho} + \frac{\nu}{R^2}\left\{\frac{\partial f^2}{\partial^2 y} + \frac{1}{y}\frac{\partial f}{\partial y}\right\} \tag{A1.5}$$

$$\frac{\partial f^2}{\partial^2 y} + \frac{1}{y}\frac{\partial f}{\partial y} - f(y)\frac{i\omega R^2}{\nu} = \frac{AR^2}{\rho\nu} \tag{A1.6}$$

If we let $\boldsymbol{\alpha = R\sqrt{\frac{\omega}{\nu}}}$ and $\boldsymbol{\xi = i^{\frac{3}{2}}\alpha y}$ the above equation is

$$\left(i^{\frac{3}{2}}\alpha\right)^2\frac{\partial f^2}{\partial^2 \xi} + \frac{i^{\frac{3}{2}}\alpha}{\xi}\left(i^{\frac{3}{2}}\alpha\right)\frac{\partial f}{\partial \xi} - if(\xi)\alpha^2 = \frac{AR^2}{\rho\nu} \tag{A1.7}$$

$$\frac{\partial f^2}{\partial^2 \xi} + \frac{1}{\xi}\frac{\partial f}{\partial \xi} - f(\xi)\frac{i\alpha^2}{\left(i^{\frac{3}{2}}\alpha\right)^2} = \frac{AR^2}{\rho\nu}\frac{i\alpha^2}{\left(i^{\frac{3}{2}}\alpha\right)^2} \tag{A1.8}$$

$$\frac{\partial f^2}{\partial^2 \xi} + \frac{1}{\xi}\frac{\partial f}{\partial \xi} + f(\xi) = -\frac{A}{i\rho\omega} \tag{A1.9}$$

Thus, the solution for the above equation is complex Bessel function,

$$f(y) = B_1 J_0\left(i^{\frac{3}{2}}\alpha y\right) + B_2 Y_0\left(i^{\frac{3}{2}}\alpha y\right) - \frac{A}{i\rho\omega} \tag{A1.10}$$

$$w(y,t) = \left[B_1 J_0\left(i^{\frac{3}{2}}\alpha y\right) + B_2 Y_0\left(i^{\frac{3}{2}}\alpha y\right) - \frac{A}{i\rho\omega}\right] e^{i\omega t} \tag{A1.11}$$

$$w(r,t) = \left[B_1 J_0\left(i^{\frac{3}{2}}\alpha \frac{r}{R}\right) + B_2 Y_0\left(i^{\frac{3}{2}}\alpha \frac{r}{R}\right) - \frac{A}{i\rho\omega}\right] e^{i\omega t} \tag{A1.12}$$

A1.2. Womersley Flow

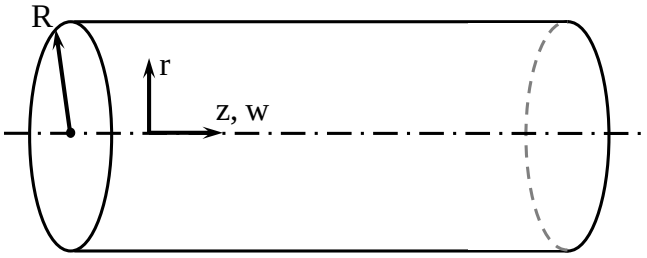

Initial consideration using Equation A1.13: w(0,t) is finite

At r = 0 → $Y_0(0) = -\infty \rightarrow B_2 = 0$

$$w(r,t) = \left[B_1 J_0\left(i^{\frac{3}{2}}\alpha \frac{r}{R}\right) - \frac{A}{i\rho\omega}\right] e^{i\omega t} \tag{A1.13}$$

Applying the B.C at the wall to Equation A1.14 : w(R,t) = 0

$$B_1 = \frac{A}{i\rho\omega}\frac{1}{J_0\left(i^{\frac{3}{2}}\alpha\right)} \tag{A1.14}$$

Thus,

$$w(r,t) = \frac{A}{i\rho\omega}\left[\frac{J_0\left(i^{\frac{3}{2}}\alpha\frac{r}{R}\right)}{J_0\left(i^{\frac{3}{2}}\alpha\right)} - 1\right] e^{i\omega t} = \frac{AR^2}{i\alpha^2\mu}\left[\frac{J_0\left(i^{\frac{3}{2}}\alpha\frac{r}{R}\right)}{J_0\left(i^{\frac{3}{2}}\alpha\right)} - 1\right] e^{i\omega t} \tag{A1.15}$$

The volume flow rate is

$$Q(t) = \int_0^R w(r,t)2\pi r\, dr \tag{A1.16}$$

$$Q(t) = \frac{A\pi R^2}{i\rho\omega}\left[1 - \frac{2J_1\left(i^{\frac{3}{2}}\alpha\right)}{i^{\frac{3}{2}}\alpha J_0\left(i^{\frac{3}{2}}\alpha\right)}\right]e^{i\omega t} = \frac{A\pi R^4}{i\alpha^2\mu}\left[1 - \frac{2J_1\left(i^{\frac{3}{2}}\alpha\right)}{i^{\frac{3}{2}}\alpha J_0\left(i^{\frac{3}{2}}\alpha\right)}\right]e^{i\omega t} \quad \text{(A1.17)}$$

A1.3. Pressure Drop Calculation for Womersley Flow

As previously stated in Equation A1.2, the pressure drop is $\frac{\partial p(t)}{\partial z} = Ae^{i\omega t}$

As any flow waveform can be represented with FFT coefficients, the pressure drop can be computed via harmonic representation (FFT coefficient) as well

$$\frac{\partial p(t)}{\partial z} = \sum_{n=1}^{N} A_n e^{in\omega t} = \sum_{n=1}^{N}\left\{\left[1 - \frac{2J_1\left(i^{\frac{3}{2}}n\alpha\right)}{i^{\frac{3}{2}}n\alpha J_0\left(i^{\frac{3}{2}}n\alpha\right)}\right]^{-1}\left[\frac{i(n\alpha)^2\mu}{\pi R^4}\right]C_n e^{in\omega t}\right\} \quad \text{(A1.18)}$$

Where **n** is harmonic variable, **N** is harmonic order, and $\mathbf{C_n}$ are FFT coefficients based from a flow waveform

A1.4. Unsteady 1-D Annulus Flow

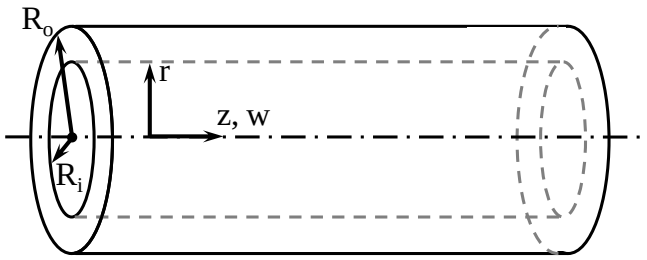

Applying the B.C.'s at both walls (will use y instead of r) to Equation A1.12

Outer wall (R_o): $w(R_o,t) = 0 \rightarrow$ at $r = R_o$, $y = 1$

Inner wall (R_i): $w(R_i,t) = 0 \rightarrow$ at $r = R_i$, $y = R_i/R_o = r_i$ $(0 < r_i < 1)$

$$w(y,t) = \left[D_1 J_0\left(i^{\frac{3}{2}}\alpha y\right) + D_2 Y_0\left(i^{\frac{3}{2}}\alpha y\right) - \frac{A}{i\rho\omega}\right]e^{i\omega t} \quad \text{(A1.19)}$$

Where,

$$D_1 = \left(\frac{A}{i\rho\omega}\right)\frac{\left[Y_0\left(i^{\frac{3}{2}}\alpha r_i\right) - Y_0\left(i^{\frac{3}{2}}\alpha\right)\right]}{\left[J_0\left(i^{\frac{3}{2}}\alpha\right)Y_0\left(i^{\frac{3}{2}}\alpha r_i\right) - J_0\left(i^{\frac{3}{2}}\alpha r_i\right)Y_0\left(i^{\frac{3}{2}}\alpha\right)\right]} \tag{A1.20}$$

$$D_2 = \left(\frac{A}{i\rho\omega}\right)\frac{-\left[J_0\left(i^{\frac{3}{2}}\alpha r_i\right) - J_0\left(i^{\frac{3}{2}}\alpha\right)\right]}{\left[J_0\left(i^{\frac{3}{2}}\alpha\right)Y_0\left(i^{\frac{3}{2}}\alpha r_i\right) - J_0\left(i^{\frac{3}{2}}\alpha r_i\right)Y_0\left(i^{\frac{3}{2}}\alpha\right)\right]} \tag{A1.21}$$

Thus,

$$w(y,t) = \frac{A}{i\rho\omega}\left[E_1 J_0\left(i^{\frac{3}{2}}\alpha y\right) - E_2 Y_0\left(i^{\frac{3}{2}}\alpha y\right) - 1\right]e^{i\omega t} \tag{A1.22}$$

$$w(y,t) = \frac{AR_0^4}{i\alpha^2\mu}\left[E_1 J_0\left(i^{\frac{3}{2}}\alpha y\right) - E_2 Y_0\left(i^{\frac{3}{2}}\alpha y\right) - 1\right]e^{i\omega t} \tag{A1.23}$$

Where

$$E_1 = \frac{\left[Y_0\left(i^{\frac{3}{2}}\alpha r_i\right) - Y_0\left(i^{\frac{3}{2}}\alpha\right)\right]}{\left[J_0\left(i^{\frac{3}{2}}\alpha\right)Y_0\left(i^{\frac{3}{2}}\alpha r_i\right) - J_0\left(i^{\frac{3}{2}}\alpha r_i\right)Y_0\left(i^{\frac{3}{2}}\alpha\right)\right]} \tag{A1.24}$$

$$E_2 = \frac{\left[J_0\left(i^{\frac{3}{2}}\alpha r_i\right) - J_0\left(i^{\frac{3}{2}}\alpha\right)\right]}{\left[J_0\left(i^{\frac{3}{2}}\alpha\right)Y_0\left(i^{\frac{3}{2}}\alpha r_i\right) - J_0\left(i^{\frac{3}{2}}\alpha r_i\right)Y_0\left(i^{\frac{3}{2}}\alpha\right)\right]} \tag{A1.25}$$

The volume flow rate can be calculated using the followings

$$Q(t) = \int_{R_i}^{R_o} w(r,t)2\pi r\,dr = 2\pi R^2 \int_{r_i}^{1} w(y,t)y\,dy \tag{A1.26}$$

$$Q(t) = \frac{A2\pi R_0^4}{i\rho\omega}\int_{r_i}^{1}\left[E_1 J_0\left(i^{\frac{3}{2}}\alpha y\right) - E_2 Y_0\left(i^{\frac{3}{2}}\alpha y\right) - 1\right]e^{i\omega t}y\,dy \tag{A1.27}$$

$$Q(t) = \frac{A2\pi R_0^4}{i\rho\omega}\left\{\frac{E_1}{i^{\frac{3}{2}}\alpha}\left[J_1\left(i^{\frac{3}{2}}\alpha\right) - J_1\left(i^{\frac{3}{2}}\alpha r_i\right)\right] - \frac{E_2}{i^{\frac{3}{2}}\alpha}\left[Y_1\left(i^{\frac{3}{2}}\alpha\right) - Y_1\left(i^{\frac{3}{2}}\alpha r_i\right)\right] - \frac{1 - r_i^2}{2}\right\}e^{i\omega t} \tag{A1.28}$$

$$Q(t) = \frac{A2R_o^4}{i\alpha^2\mu}\left\{\frac{E_1}{i^{\frac{3}{2}}\alpha}\left[J_1\left(i^{\frac{3}{2}}\alpha\right) - J_1\left(i^{\frac{3}{2}}\alpha r_i\right)\right] - \frac{E_2}{i^{\frac{3}{2}}\alpha}\left[Y_1\left(i^{\frac{3}{2}}\alpha\right) - Y_1\left(i^{\frac{3}{2}}\alpha r_i\right)\right] - \frac{1-r_i^2}{2}\right\}e^{i\omega t}$$

(A1.29)

A1.5. Pressure Drop Calculation for Unsteady 1-D Annulus Flow

As previously stated, the pressure drop is $\frac{\partial p(t)}{\partial z} = Ae^{i\omega t} = \sum_{n=1}^{N} A_n e^{in\omega t}$

As any flow waveform can be represented with FFT coefficients, the pressure drop can be computed via harmonic representation (FFT coefficient) as well

$$\frac{\partial p(t)}{\partial z} =$$

$$\sum_{n=1}^{N}\left\{\frac{E_1}{i^{\frac{3}{2}}n\alpha}\left[J_1\left(i^{\frac{3}{2}}n\alpha\right) - J_1\left(i^{\frac{3}{2}}n\alpha r_i\right)\right] - \frac{E_2}{i^{\frac{3}{2}}n\alpha}\left[Y_1\left(i^{\frac{3}{2}}n\alpha\right) - Y_1\left(i^{\frac{3}{2}}n\alpha r_i\right)\right] - \frac{1-r_i^2}{2}\right\}^{-1}\left[\frac{i(n\alpha)^2\mu}{2R_o^4}\right]C_n e^{in\omega t}$$

(A1.30)

Where **n** is harmonic variable, **N** is harmonic order, and $\mathbf{C_n}$ are FFT coefficients based from a flow waveform

VITA

NAME Wojciech Kalata

EDUCATION B.S. Mechanical Engineering, University at Illinois at Chicago, Chicago, Illinois, 1999
M.S. Mechanical Engineering, University at Illinois at Chicago, Chicago, Illinois, 2002

EXPERIENCE Research Engineer
Spraying Systems Co.
Spray Analysis and Research Services 2006-present

Research/Teaching Assistant
Heat Transfer and Fluid Mechanics II
University of Illinois at Chicago, 2000-2006

Graduate Student Researcher
Argonne National Laboratory, Summer 2000
Mathematics and Computer Science Division

HONORS American Council for Polish Culture for a Pulaski Scholarship for Advanced Studies, 2003

Summer student appointment at Argonne Natoional Laboratory at Mathematics and Computer Science, Summer 2000

Academic Achievement Award for 1997-98 at UIC Men's Varsity Soccer

JOURNAL PUBLICATIONS

1. Kalata W., Martin B.A., Loth F., Royston T.J., Oshinski J.N., and Jerosch-Herold M.: MR Measurement of Cerebrospinal Fluid Velcotiy Wave Speed in the Spinal Canal. *IEEE Transactions on Biomedical Engineering*, Vol. 56, No. 6, pp. 1765-8, June 2009.
2. Ford, M.D., Nikolov, H.N., Milner, J.S., Lownie, S.P., Demont, E.M., Kalata, W., Loth, F., Holdsworth, D.W., and Steinman, D.A.: PIV-Measured Versus CFD-Predicted Flow Dynamics in Anatomically Realistic Cerebral Aneurysm Models. *J Biomech Eng*, Vol. 130, No. 2, pp. 021015-1-9, April 2008.
3. Martin, B.A., Kalata, W., Loth, F., Royston, T.J., and Oshinski, J.N.: Syringomyelia hydrodynamics: an in vitro study based on in vivo measurements, *J Biomech Eng*, Vol. 127, No. 7, pp. 1110-1120, December 2005.

PUBLISHED WORK – Conference and Symposium Papers

1. Kalata, W., Brown, K.J., and Schick, R.J.: Injector study via VOF: Emphasis on vapor condensation due to spray. In *ILASS Americas, 23rd Annual Conference on Liquid Atomization and Spray Systems*, Ventura, CA, May 2011.
2. Brown, K.J., Kalata, W., and Schick, R.J.: Experimental and computational study of a spray at multiple injection angles impact study of a clean in place tank wash system. In *ILASS Americas, 22nd Annual Conference on Liquid Atomization and Spray Systems*, Cincinnati, OH, May 2010.
3. Bade, K.M., Kalata, W., and Schick, R.J.: Experimental and computational study of a spray at multiple injection angles. In *ILASS Americas, 22nd Annual Conference on Liquid Atomization and Spray Systems*, Cincinnati, OH, May 2010.
4. Bade, K.M., Kalata, W., and Schick, R.J.: Spray plume characteristics at multiple cross-flow angles, experimental and computational results. In *ICLASS 2009, 11th Triennial International Annual Conference on Liquid Atomization and Spray Systems*, Vail, CO, July 2009.
5. Kalata, W., Brown, K.J., Bade, K.M., and Schick, R.J.: Dimensional, thermal and evaporative spray plume characteristics using computational fluid dynamics. In *ICLASS 2009, 11th Triennial International Annual Conference on Liquid Atomization and Spray Systems*, Vail, CO, July 2009.
6. Martin, B.A., Loth, F., Kalata, W., Royston, T.J., Oshinski,J.N., and Jerosch-Herold, M.: MR Measurement of Pulse Wave Velocity in the Spinal Canal. In *Summer Bioengineering Meeting*, Marco Island, FL, June 2008.
7. Brown, K.J., Kalata, W., and Schick, R.J.: Drop size distribution analysis with respect to height - numerical simulation versus empirical evaluation. In *ILASS Americas, 21st Annual Conference on Liquid Atomization and Spray Systems*, Orlando, FL, May 2008.
8. Cronce, K., Kalata, W., and Schick, R.J.: Model to predict hydraulic flat spray distribution. In *ILASS Americas, 21st Annual Conference on Liquid Atomization and Spray Systems*, Orlando, FL, May 2008.
9. Knasiak, K., Schick, R.J., and Kalata, W.: Multiscale design of rain simulator. In *ILASS Americas, 20th Annual Conference on Liquid Atomization and Spray Systems*, Chicago, IL, May 2007.
10. Martin, B.A., Kalata, W., Loth, F., Royston, T.J., and Oshinski, J.N.: Syringomyelia hydrodynamics: an in vitro study based on in vivo measurements. In *Summer Bioengineering Conference*, Vail, CO USA, June 2005.
11. Ford, M.D., Nikolov, H.N., Milner, J.S., Kalata, W., Loth, F., Lownie, S.P., Holdsworth, D.W., and Steinman, D.A.: In vitro validation of an image-based CFD model of an anatomically realistic cerebralaneurysm. In *Summer Bioengineering Conference*, Vail, CO, June 2005.
12. Martin, B.A., Kalata, W., Oshinski, J.N., Loth, F., and Royston, T.J.: Construction and validation of a complaint model of the cerebrospinal fluid system with fluid filled syrinx. In *2004 ASME International Mechanical Engineering Congress & Exposition*, Anaheim, CA, November 13-19, 2004.
13. Kalata, W., Martin, B.A., Oshinski, J.N., and Loth, F.: Hydrodynamics of cerebrospinal fluid in spinal canal with Chiari malformation and syringomyelia. In *2004 ASME International Mechanical Engineering Congress & Exposition*, Anaheim, CA, November 13-19, 2004.

14. Kalata, W., Lee, S.E., Alperin, N., Fischer, P.F., and Loth, F.:Numerical simulation of cerebrospinal fluid motion within a healthy and diseased spinal canal. In *World Congress of Biomechanics*, Proceedings CD, Calgary, Canada, Aug. 2002.
15. Kalata, W., Lee, S.E., Piersol, N.E., Alperin, N., Fischer, P.F., and Loth, F.: Three-dimensional computational fluid dynamics of cerebrospinal fluid motion within the spinal cavity. In *2001 Bioengineering Conference*, BED-Vol. 50, Snowbird, Utah, pp. 449-50, June 2001.
16. Piersol, N.E., Lee, S.E., Kalata, W., Loth, F., Fischer, P.F., Alperin, N., and Bassiouny, H.B.: Automated simulation of velocity and wall shear stress patterns inside a healthy carotid bifurcation. In *2001 Bioengineering Conference*, BED-Vol. 50, Snowbird, Utah, pp. 755-6, June 2001.
17. Lee, S.E., Piersol, N.E., Kalata, W., Skelly, C.L., Curi, M.A., Fischer, P.F., Loth, F., and Schwartz, L.B.: Numerical simulation of vein graft hemodynamics. In 2001 *Bioengineering Conference*, BED-Vol. 50, Snowbird, Utah, pp.733-4, June 2001.

PRESENTED WORK – Conference/Symposium Abstracts and Posters

1. Kalata, W., Brown, K.J., Bade, K.M., and Schick, R.J.: Study of a hollow cone spray at varying injection angle. In *Chicago ANSYS Regional Conference - Engineering the System*, Chicago, IL, August 2011.
2. Brown, K.J., Kalata, W., and Schick, R.J.: Impact study of a clean in place tank wash. In *Chicago ANSYS Regional Conference*, Chicago, IL, August 2010.
3. Brown, K.J., Kalata, W., and Schick, R.J.: Optimization of gas conditioning design for NOx controll. In *Air Quality VII*, Arlington, VA, October 2009.
4. Martin, B.A., Kalata, W., Loth, F., Oshinski, J.N., and Royston, T.J.: Characterization of pressure wave transmission in a fluid filled syrinx. In *Biomedical Engineering Society Annual Meeting*, Chicago, IL, 10/11-14, 2006.
5. Kalata, W., Martin, B.A., Loth, F., Royston, T.J., Oshinski, J.N., and Jerosch-Herold, M.: Measurements of pulse wave velocity in the spinal canal. In *Biomedical Engineering Society Annual Meeting*, Chicago, IL, 10/11-14, 2006.
6. Martin, B.A., Kalata, W., Loth, F., Oshinski, J.N., and Royston, T.J.: Experimental Syringomyelia Hydrodynamics: The importance of pressure phase relation on syrinx pathogenesis. In *3rd Annual Neural Hydrodynamics Symposium*, Cleveland, OH, 5/12-14, 2005.
7. Kalata, W., Martin, B.A., Loth, F., and Oshinski, J.N.: Differences in cerebrospinal fluid motion in Chiari malformation patients and healthy volunteers," *3rd Annual Neural Hydrodynamics Symposium*, Cleveland, OH, 5/12-14, 2005.
8. Martin, B.A., Kalata, W., Oshinski, J.N., and Loth, F.: The engineering perspective: syringomyelia. In *ASAP Annual Conference*, Key Biscayne, FL, July 2004.
9. Martin, B.A., Kalata, W., Royston, T.J., Oshinski, J.N., and Loth, F.: Experimental Study on Pressure and hydrodynamic flow within the subarachnoid space. In *2nd Symposium of Neural Hydrodynamics*, Menlo Park, CA, May 1, 2004.
10. Martin B.A., Kalata, W., Oshinski, J.N., and Loth, F.: Importance of Mechanical Forces in the development of syringomyelia for patients with Chiari malformation. In *ASAP Annual Conference*, New York City, NY, July 2003.

11. Kalata, W., Lee, S.E., Alperin, N., Fischer, P.F., and Loth, F.: Calculation of unsteady resistance within the spinal canal based on MRI measurements. In *1st Symposium of Neural Hydrodynamics*, Pittsburgh, PA, September 2002.
12. Loth F., Kalata, W., Lichtor, T., and Alperin, N.J.: The potential of computer simulations to help in the diagnosis and treatment of syringomyelia. In *ASAP Annual Conference, SM/CM Physician/Engineer Workshop*, St. Louis, MO, July 27, 2002.